NUCLEAR ENERGY RESEARCH INITIATIVE (NERI)
FINAL REPORT

Nuclear Reactor Power Monitoring Using Silicon Carbide Semiconductor Radiation Detectors

Project Number DE-FG03-02SF22620

October 1, 2002 –September 15, 2007

Submitted by:

Lead Organization: The Ohio State University

Co-PI Thomas E. Blue, Ph.D.
Co-PI Don W. Miller, Ph.D.

Collaborating Organizations:

Westinghouse Electric Company
General Atomics Company

Submitted on:

June 30, 2008

Section 1: Project Overview

1.1 Task 1 Overview

1.1.1 Task 1 Description

To provide a perspective for our accomplishments, all of the sub-tasks in Task 1 (as they were identified in the proposal) are identified below, and a brief description of the subtasks is given.

Task 1 Define Generation IV Reactor Power Monitoring Requirements

Task 1.1 The power monitoring requirements for the IRIS and GT-MHR will be evaluated. Parameters considered will include maximum power level uncertainty, response time, etc.

Task 1.2 The optimum locations for power monitors will be selected for both the IRIS and GT-MHR. Factors to be considered will include the power monitoring requirements defined in Task 1.1 as well as expected detector sensitivity and the presence of gamma ray background.

Task 1.3 Other applications and opportunities offered by SiC power monitors will be evaluated. The prospects for on-line fault identification and diagnosis using pulse height and pulse shape analysis will be explored. The use of miniature SiC detectors to define axial, azimuthal, and radial flux profiles will be investigated.

1.1.2 Task 1 Performance History

The Sub-Tasks 1.1 and 1.2 both have associated with them Sub-Sub-Tasks. There are two Sub-Sub-Tasks per Sub-Task. One Sub-Sub-Task relates to the IRIS reactor concept and is to be carried out as a collaborative effort between OSU and Westinghouse Electric Company (WEC). The other Sub-Sub-Task relates to the GT-MHR reactor concept and is to be carried out as a collaborative effort between OSU and General Atomics (GA). In Quarters 1 and 2 we emphasized the Sub-Sub-Tasks for IRIS. In Quarters 3, 4, and 5 we emphasized the performance of the Sub-Sub-Tasks for the GT–

MHR, to correct the imbalance in Quarters 1 and 2.

In Quarter 3, a graduate student, Benone Lohan, calculated the neutron and gamma-ray radial flux distributions in the reactor cavity and in the RCCS resulting from fission events within the GT-MHR core. The GT-MHR reactor was modeled as nested infinitely long cylinders of varying compositions. The calculations that were performed were appropriate for an assessment of the neutron and gamma-ray radial flux distributions in the midplane of the reactor core.

In Quarter 4, Benone repeated the calculations for the GT-MHR that he undertook previously in Quarter 3. However, in his repetition of the calculations, Benone accounted for axial variations of the core power and calculated the neutron and gamma-ray radial flux distributions, as a function of radius and axial location, in the reactor cavity and in the RCCS.

In Quarter 5, we considered the possibility of placing SiC detectors within the central reflector of the GT-MHR. We calculated the neutron flux in detector capsules, for detector capsules located at radial distances R=117 and R=153 cm from the central reflector centerline.

In Quarter 6, we concerned ourselves with quantifying radiation exposures in the OSU Research Reactor (OSURR) Beam Port 1 in terms of the 1 MeV equivalent neutron fluence. The resulting neutron dosimetry data are summarized below for irradiation of SiC in the irradiation vessel in Position 4 in Beam Port 1 for operation at 50 kW:

$\phi^{Total}_{eq,1MeV,SiC}$ **(n cm^{-2}s^{-1})** =7.20 x 10^{10}, $\mathbf{H_{SiC}}$ =0.6610, and $\dot{d}_{SiC}$ **(n cm^{-2}s^{-1})(MeV-mb)** =2.05*10^{12}

In Quarter 7, we predicted that the 1 MeV equivalent neutron flux (in n cm^{-2}s^{-1}) for full power operation of the GT-MHR is on the order of 1.2E+12 for the detector capsule located at a core radii of 117 cm and is on the order of 1.9E+13 for the detector capsule located at a core radii of 153 cm. The corresponding values of the 1 MeV equivalent neutron flux for ex-core locations in the RC are on the order of 3E+07 for both R=430 cm and R=530 cm. Within the RCCS, the 1 MeV equivalent neutron flux is on the order of 3.4E+07 for R=610 cm. These results indicate that the OSURR Beam Port 1 can be used

to simulate the degradation of the SiC detectors that would be incurred in the GT-MHR RC and RCCS over a time period that is more than 2400 times the testing period in the OSURR (i.e. one hour of testing at full power operation in Beam Port of the OSURR would (neglecting rate effects) result in an amount of damage that is equivalent to the damage which would be incurred by the detectors during 480 hours of operation of the GT-MHR).

Also, in Quarter 7, we used the calculations of the neutron radial flux distribution in the reactor cavity and in the RCCS, which were performed in Quarter 4, and the calculations of the neutron flux distributions within the central reflector of the GT-MHR, which were performed in Quarter 5, to predict the detector count rate at the respective detector locations. The maximum triton count rate for a capsule at R=153 cm and Z=520cm for full power operation (P=600 MWt) is on the order 6.8E+5 T/s for a detector with a 500 μm diameter and a 1 μm thick LiF layer for 90% Li-6 enrichment. For the same detector, at full power the maximum triton count rate for a capsule at R=117cm and Z=520 cm is 6.0E+05 T/s. The depletion of ^{6}Li for one cycle is about 0.92%, if the detector is positioned at R=153 cm and Z=320 cm, and is 0.11% if the detector is positioned at R=117 cm and Z=320 cm. For the same detector, the maximum triton count rate for R=430 cm and R=530 cm is on the order of 5 T/s for Z=520 cm, while the count rate for R=610 cm and Z=520 cm is on the order of 40 T/s.

In Quarter 9 we reported that we had developed a method to estimate the DPA/fluence, using two well-known codes: MCNP and TRIM. This effort was undertaken since predictions of radiation damage and radiation effects to the SiC detectors are important for deciding where the SiC detectors should be placed.

In Quarter 10, we reported the results of our efforts to develop a Simulink model of the GT-MHR with which we can analyze Full Power Reactivity Insertion Transients (FPRITs) and Startup Reactivity Insertion Transients (SURITs), in order to determine scram setpoints and scram initiation times that protect the core in the event of FPRITs and SURITs. In addition, we presented the code results for the case of a FPRIT.

In Quarter 11, we described the application of the Simulink code to the analysis of a

SURIT for the GT-MHR, for a SURIT that is initiated with the GT-MHR in a state in which: 1) Rod Bank Groups 1 and 2 are fully withdrawn from the core, 2) The remaining rod bank groups are fully inserted, 3) The reactor is cold (300 K) and sub-critical at the BOEC (Beginning of Equilibrium Cycle) condition and 4) The reactor is operating with a fission power of 5.09 E-7 W. For these conditions, if Rod Bank Group 3 (the rod bank with the largest worth of any of the rod banks) is withdrawn at the maximum rod withdrawal speed, then the maximum reactor power in this case is 313 MW; i.e., the reactor fission power never reaches the FPRIT trip point of 900 MW.

In the Quarter 12 Quarterly Report, we described the application of the Simulink code to the analysis of a series of SURITs, for which the initial power is varied. An envelope of response was determined to establish which initial powers correspond to the worst case SURIT.

In the Quarter 15 Quarterly Report, we described our calculations using MCNP5 and TRIM to determine, ϕ^{Total}, $\phi^{Total}_{eq,1MeV,SiC}$, H_{SiC} and the triton count rates at four radii in the downcomer region of IRIS, inside of two different designs of instrumentation tube. In a three-layer instrumentation tube, at R = 155 cm, where the triton count rate is more appropriate than for other locations, $\phi^{Total}_{eq,1MeV,SiC}$ and ϕ^{Total} are 8.67E+10 $cm^{-2}s^{-1}$ and 2.26E+11 $cm^{-2}s^{-1}$, respectively. At this location H_{SiC} is 0.38 and the triton count rate is 1.40E+05 cps. In this calculation, we assumed that the detector (^{6}LiF radiator and SiC diode) radius is 250 μm and that tritons that are born in (n,α) reactions in the ^{6}LiF radiator are recorded with a detection efficiency of 39%. We found no position in the IRIS such that the count rate is high enough (preferably more than 1E+06 cps) and the displacement damage (in term of $\phi^{Total}_{eq,1MeV,SiC}$) is small enough that the SiC Schottky diode detectors can tolerate at least one reactor refueling cycle.

In the Quarter 16 Quarterly Report, we developed methods to estimate the count rate and number of defects at 0 K created per atom using two well-known codes: MCNP and TRIM. We used the methods which we developed previously (as described in the Quarter 15 Quarterly Report) to predict at what positions in a nuclear reactor silicon carbide (SiC) semiconductor diode detectors may work functionally as neutron monitors

for at least one refueling cycle of the Gas Turbine-Modular Helium Reactor (GT-MHR). It was shown that, for the stated SiC detector geometry, in comparison with detectors placed at R153, for detectors place at R117, the count rate for the detectors is one-half, but the average $(PDPA)_{all}$ over a GT-MHR refueling cycle is twenty times smaller. For SiC detectors placed at R81 and R0 (the center of the central reflector), the reduction in the average $(PDPA)_{all}$ over a GT-MHR refueling cycle is much more significant. Based on available data in literature, SiC detectors placed in a capsule that is located at R0 may tolerate at least one GT-MHR refueling cycle. However, more study is needed to define the detector failure, and then find the *PDPA* for the corresponding neutron fluence and energy spectrum that caused the SiC detector to fail.

In the Quarter 17 Quarterly Report, using a multiscale modeling methodology, we developed a simulation framework to estimate the number of defects for SiC detectors placed in the thermal region of the GT-MHR. We found that at 500 K, the Point Defects per Atom (PDPA) is 1.5×10^{-3} in the depleted region for SiC detectors placed at GT-MHR R0 for a refueling cycle, and that approximately half of the initially created defects anneal out during that period. However, from these results we currently cannot predict the changes in detection ability of the detector. Identification and modeling of the critical *PDPA* for detector failure is subject of our ongoing research.

Also, in the Quarter 17 Quarterly Report, we included that our KLMC needs some modifications to be able to model the damage recovery at higher temperatures. These modifications include the migration of defects to the detector boundaries and interfaces and inter-cascade interactions. With this, studying the effect of different ambient temperatures on the damage annealing will become possible. Studies such as these are necessary to find the most appropriate temperatures for SiC neutron monitors placed in a thermal neutron environment. The final step in the modeling process is to evaluate the influence of the defects on the carrier mobility and other electrical properties of SiC, and to predict how these changes in the electrical properties of SiC affect the count rate of the power monitor.

1.2 Task 2 Overview

1.2.1 Task 2 Description

To provide a more complete perspective of this project, the sub-tasks in Task 2 are identified below, and a brief description of the subtasks is given.

Task 2 Design, Fabrication, and Evaluation of a High-Speed SiC Neutron Monitoring Channel.

Task 2.1 SiC detector elements will be designed. Factors to be considered include SiC diode area, depletion region thickness, substrate and depletion region n^- doping levels, Schottky contact characteristics, and performance of the detector packages at high temperature and in high radiation fields.

Task 2.2 Design specifications defined in Task 2.1 will be used to guide the manufacture of the SiC Schottky diodes. A qualified SiC vendor such as Cree, Inc will carry out packaging of the diodes. A prototype SiC power monitor will be assembled with these diodes.

Task 2.3 Electronics will be developed to meet the requirements of the high event rates that are anticipated to be needed to meet reactor power monitoring accuracy and response time requirements. These event rates are expected to be $10^7 - 10^8$ sec^{-1} or higher, and may require the development of new pulse processing techniques.

Task 2.4 The prototype SiC power monitor will be tested. Pulse shape characteristics, including pulse height, rise time, tailing time, etc. will be defined. These pulse shape characteristics will be electronically modified where appropriate to provide an optimized neutron response shape that will facilitate the development of high event rate electronics.

Task 2.5 The prototype electronic counting channel for the SiC neutron detectors will be assembled.

Task 2.6 The prototype SiC power monitor and high event rate electronics prototype will be reactor tested at the OSU Research Reactor (OSURR)

under neutron fluence rate conditions that will provide pulse rates that are commensurate with Generation IV monitoring requirements.

1.2.2 Task 2 Performance History

Regarding Task 2.1 and 2.2, our WEC subcontractor colleagues have developed designs for the SiC diode detectors that were used in the neutron-monitoring channel. In the Quarter 4 report, we discussed our progress in developing a TRIM model of such a diode detector, and how we used the TRIM results to develop MatLab simulation models of the detector output current signal.

Task 2.3 was the focus of our research efforts regarding Task 2 for Quarters 4, 5, and 6. The TRIM/MatLab simulation models of the detector output current signal that were developed in Quarter 4 to fulfill the obligations of Tasks 2.1 and 2.2 are also important in fulfilling the obligations of Task 2.3.

In Quarter 5, we reported the continued development of the simulation model from the output of the SiC detector to the channel's end with: 1) the addition of a distributed parameter model of the cable using the program PSpice and 2) the inclusion of MatLab models of a voltage sensitive preamplifier and discriminator. We concluded that the proposed electronic channel, with a voltage sensitive preamplifier of the type that we specified, is able to monitor the neutron flux of the core in the pulse mode with a count rate 4.0E+07 counts/s with a 9% deadtime loss. The speed of the channel is limited by the discriminator dead time.

In Quarter 6, we reported our continued development of the simulation model from the output of the SiC detector to the channel's end (a discriminator) using a charge sensitive preamplifier, as opposed to a voltage sensitive preamplifier, as was used in our analysis in Quarter 5.

In Quarter 8, we reported the results of our construction and testing of a fast electronic counting channel for the SiC diode detectors based on our modeling of the channel with TRIM, SIMULINK and MatLab. The experimental setup was flawed because three amplifiers were used in the channel, instead of two, which was later shown

to be the optimum number of amplifiers. Despite this flaw, the results of the experiment were still valuable regarding the conclusion that we drew from the experiments regarding pulse rise time. The rise time of the detector signal was calculated to vary from 170 ps to 520 ps.

In Quarter 9, we reported the results of our efforts to establish a baseline for measurements regarding the degradation of the performance of the SiC detectors as a consequence of irradiation in mixed neutron and gamma-ray fields. We used a standard pulse height analysis (PHA) counting chain with a charge sensitive preamplifier to obtain thermal-neutron and fast-neutron pulse-height response data for SiC diodes.

In the Quarter 13 Quarterly Report, we described testing to evaluate the degradation of the performance of the SiC detectors as a consequence of irradiation in mixed neutron and gamma-ray fields. The evaluation of the degradation of the performance was accomplished using a standard pulse height analysis (PHA) counting chain with a charge sensitive preamplifier to obtain thermal-neutron and fast-neutron pulse-height response data for SiC diodes. The measurements that are reported were taken by Dr. Ruddy and Mr. John Seidel, with the assistance of OSU project personnel. Three SiC detectors were used; two with nominal ^{6}LiF converter foil thicknesses of 24.2 μm and 2.5 μm, and one without a converter foil. A noticeable shift to lower pulse heights was observed as a function of increasing power level. A smaller shift to lower pulse heights was observed as a result accumulated neutron and particle fluences for repeated measurements at the same power.

In the Quarter 14 Quarterly Report, we presented the results of reactor testing of a high-speed SiC neutron-monitoring channel, which is based on the use of a voltage sensitive preamplifier. The results show that the degradation of the detectors is sufficiently severe at room temperatures, that reactor testing of the high-speed SiC neutron-monitoring channel necessarily involves degradation of the performance of the detector, if the high-speed SiC neutron-monitoring channel is tested at its high count rate limit.

Section 2: Final Work

The work that is reported below integrates contributions to both Task 1 and Task 2 and as such is appropriate for the Final Report.

2.1 Experimental and Computational Evaluation of the Response of a SiC Neutron Monitoring System in a Thermal Neutron Field

2.1.1 Introduction

Silicon carbide (SiC) is an interesting material for nuclear-reactor power monitor detectors. It has a wide band-gap, small volume and high break down electric field. In addition, SiC is chemically and neutronically inactive. Using SiC power monitors as in-core detectors provides the ability for high counting rate that may help to increase the safety margins of nuclear reactors. Experiments at the Ohio State University research reactor (OSURR) [1] showed that SiC detectors cannot survive a fast neutron flux for an appreciable irradiation time. However, the situation in a thermal neutron environment is different, since thermal neutrons do not have enough energy to create displacement damage defects via scattering in SiC. Furthermore, the damage caused by ^{29}Si and ^{13}C recoils produced by (n, gamma) reactions in SiC is negligible. In fact, a computer modeling study on the usage of SiC detectors in the GT-MHR [2] showed that SiC detectors with a ^{6}LiF converter may live as long as a reactor refueling cycle, if placed in the center of the GT-MHR's central reflector, where neutrons are highly thermalized.

The use of silicon detectors with converters like ^{6}Li or ^{10}B was proposed in the 1960's [3]. Recently, researchers at the Westinghouse Electric Company have published several papers regarding use of SiC diode detectors with LiF converter for thermal neutron spectroscopy [4-6].

We demonstrate the performance of SiC diode detectors with a LiF converter in the thermal column facility (TC) of the OSURR. The experimental count rate was observed to be 2.9×10^{4} cps. This count rate, based on our best knowledge, is one of the highest published count rates for this kind of detector placed in a thermal neutron environment. We completed the demonstration by comparing the TRIM simulation results with the experimental data. The experimentally determined thermal neutron flux in the TC at the detector position and TRIM (Ref. 7) simulations were used to estimate the maximum

triton count rates. The comparison is made to determine if the experimental count rate agrees reasonably well with the calculated maximum count rate.

2.1.2 Detector Design

To observe the triton response in the SiC p+-n diode, a detector with a 1.56-μm LiF converter (with 95% enriched ^{6}LiF) was used. ^{6}Li atoms in the LiF converter may absorb thermal neutrons and generate 2.05- MeV alpha and 2.73-MeV triton particles (^{6}Li(n,^{3}H)α reaction). An 8-μm Al layer was used to minimize damage in the SiC by blocking all alpha particles. However, most tritons have enough energy to pass through this layer and reach the 4.8-μm SiC active layer. The diameter of the LiF converter is 0.508 cm and the SiC diode area is 1.1 mm x 1.1 mm (diode is a square). The active area of the diode is approximately 0.965 mm^{2}. Upon irradiation in the TC, one can observe the triton peak in the recorded detector pulse-height spectra and the concomitant triton induced radiation damage on the detector. A schematic of the detector is shown in **Error! Reference source not found.**. Also, a top view of the detector diode package is shown in **Error! Reference source not found.**.

2.1.3 Theoretical Calculations

2.1.3.1 TRIM Simulation

The purpose of performing TRIM simulations was to study the energy deposited in the active volume of the SiC detector by the thermal neutrons through the ^{6}Li(n,α)^{3}H reaction. To perform the simulation, the target and the ions that strike the target were specified. The target was SiC and the ions were tritons. An input file named "TRIM.dat" was created for the neutron-induced triton particles, including various depths and emission angles within the LiF layer.

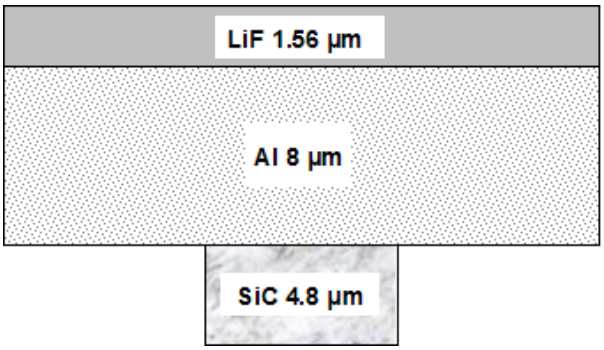

Fig. 1. Schematic of side view of SiC detector. The diameter of the LiF converter is 0.508 cm and the SiC diode active area is 0.965 mm^2 (diode is a square). Only the active region of SiC is shown.

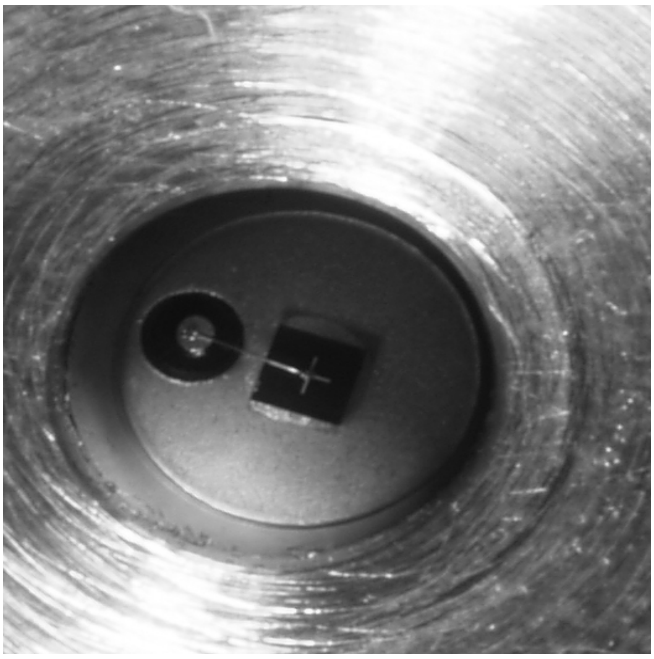

Fig. 2. Top view of the detector Schottky diode package

The simulation was performed in two steps. A MATLAB program was written to generate the "TRIM.dat" input file. The code was written based on the Monte Carlo acceptance/rejection technique. It was assumed, in the code, that tritons were generated isotropically and uniformly throughout the LiF volume. The code writes, as input for TRIM, a file that contains only information regarding those tritons that are born with a direction of motion that will cause them to strike the p^+-n diode detector's active volume; thus greatly reducing the computational time and the statistical errors for the TRIM calculations. It should be noted that, only the ions that strike the detector's active volume were tracked in the TRIM calculations. However, for determining the efficiency of the detector, all the ions, both those accepted and tracked and those rejected and not tracked, were considered. The MATLAB based rejection scheme yielded a sampling efficiency of about 2.0×10^{-2}.

TRIM simulations create a number of output files that provide information such as collision details for each ion, track by track, and transmitted-ion details (for ions that enter the SiC active volume). Once the TRIM simulation was completed, the file containing collision details was processed. For the processing, only those tritons that had lost energy through interaction with Si or C atoms in the SiC active volume were considered. The magnitude of the current pulse is proportional to the number of electron-hole pairs created in the active volume, which in turn is proportional to the deposited energy. Since tritons started at different depths within the LiF, and underwent multiple interactions in the SiC active volume, the amounts of energy lost by tritons were different. Most of the tritons passed through the SiC active volume completely and deposited their end-of-range energy in the SiC inactive volume (or substrate).

The energy deposited by each triton in the SiC active volume was calculated on a track by track basis. A combination of EXCEL software and a MATLAB program were used to process the results from the collision file. The predicted triton geometric efficiency, based on TRIM simulations, was found to be 1.2×10^{-2}.

2.1.4 Experiments in Thermal Column

To evaluate the degradation of SiC diode neutron detectors in mixed neutron/gamma ray radiation fields, experiments were performed in the TC of the OSURR. The performance of the SiC detectors was studied using a standard pulse height analysis counting chain with a charge sensitive preamplifier.

2.1.4.1 Experimental Design

The SiC detector package was connected to a pulse processing system consisting of a preamplifier (ORTEK 142 B) and a digital spectrum analyzer (Canberra DSA 2000). An oscilloscope (Hewlett Packard 54601B, 100 MHz) was used to study the shape of the signal from the amplifier. Bias voltage was provided by the DSA to the detector through the preamplifier. A power monitoring program was used to verify the reactor power that was displayed in the control room. Fig. shows a schematic of the experimental setup used in the TC.

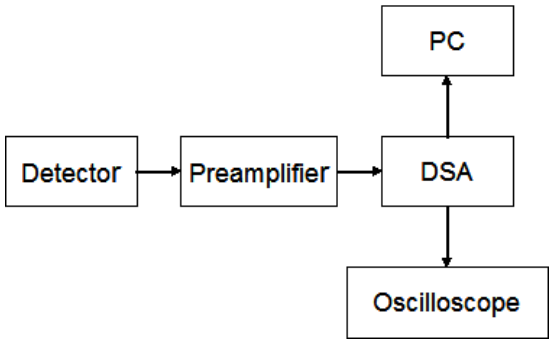

Fig. 3. Experimental setup used for SiC detector testing in the OSURR TC

Detector Measurements

The detector was placed in the TC and operated in pulse mode. The detector was reverse biased to 20 V. The DC current while operating the detector in the TC was on the order of Pico amps. The pulse height spectrum was obtained for the detector in position in the TC. The reactor power was increased from 1 kW to 455 kW and the spectrum was recorded at various power levels. The counting time for each measurement was 5 minutes. The experiments were performed at room temperature inside the TC.

The tritons produced by thermal neutrons, lose energy in the detector and create electron-hole pairs. The electron-hole pairs created in the active volume of the detector are collected and recorded as a current pulse. As the peak pulse voltage is proportional to the integral of the current pulse, which is in turn proportional to the deposited energy, the recorded pulse- height distribution (PHD) is the histogram of the number of pulses that arise as a consequence of energy deposition within various increments of deposited energy.

Error! Reference source not found. shows the recorded PHD for the detector. **Error! Reference source not found.** has as the title of its ordinate "Corrected Counts/ kW*s". The word "Corrected", in this context, means that the effects of finite detector system resolving times have been accounted for using a real time to live time correction factor that is output by the DSA 2000. This real time to live time correction factor was applied to all the recorded PHDs to account for dead time effects. Measurements were recorded of the fission product decay gammas after the reactor was shut down. This measurement showed that gamma-ray events were confined to channels less than 150 (Figure 3). To eliminate most of the gamma-ray induced pulses from processing by the DSA 2000, a lower level discriminator (LLD) for pulse height was set on the DSA 2000 to channel 10 for neutron counting. One can observe by comparing the PHDs in **Error! Reference source not found.** and Figure 3 that this LLD setting was sufficiently large to eliminate noise and virtually all gamma-ray induced pulses from neutron-induced triton pulses in the recorded PHDs. To further discriminate gamma-ray induced pulses from neutron-induced triton pulses, in the post-processing of the PHDs to obtain Corrected Counts/ kW*s, only counts for channel numbers greater than 150 were included in the sum.

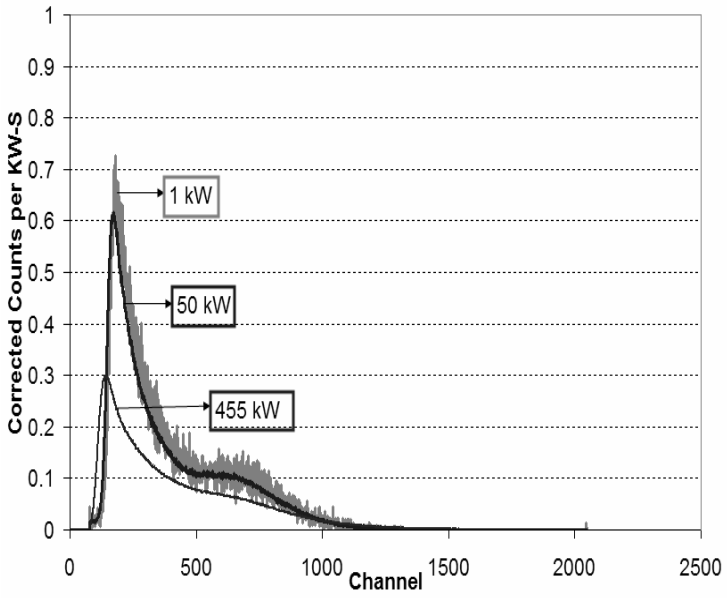

Fig. 4. The pulse height spectra of SiC detector placed in the TC for various reactor power levels as specified by the curve labels.

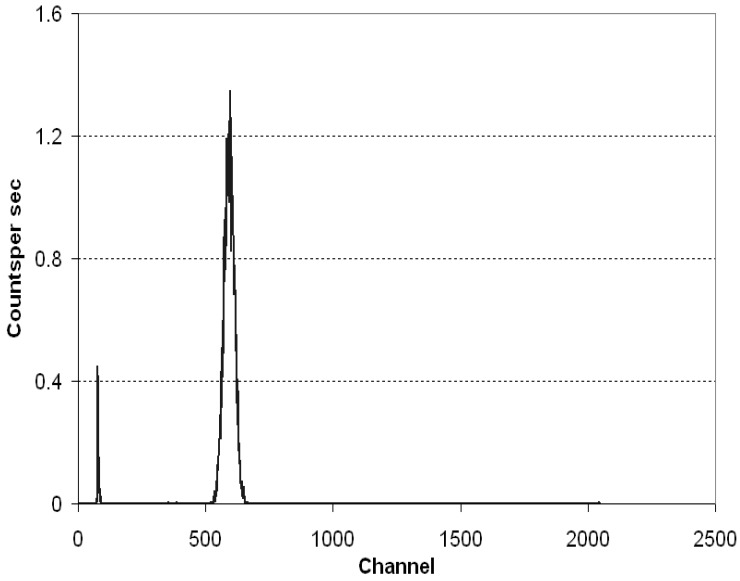

Figure 3 SiC detector spectrum after reactor shutdown. The peak at channel 600 is due to

pulser.

2.1.4.2 Detector Degradation Due to Dose Rate

Experiments performed in the TC with the detector showed degradation in the detector performance when the detectors were irradiated at different power levels. The results were analyzed to account for the degradation in the detector performance. As shown in **Error! Reference source not found.** the spectrum was shifted toward the left as the detector was irradiated for increasingly large power levels ranging from 1 kW to 455 kW. This flux dependant shift appears to be operationally significant. Irradiations such as those that led to **Error! Reference source not found.** were repeated again, and the shift in the spectrum was prominent every time the detector was irradiated at increasingly large power levels. **Error! Reference source not found.** also shows that the area beneath the spectra for channels greater than 150 (this subset of channels includes all the channels for which there is only a contribution from neutron induced pulses) decreased with increasing reactor power. The count rate decreased from 146.91 counts/kW-s (includes real time to live-time correction) to 77.97 counts/kW-s (includes real time to live time correction) as reactor power was increased from 1 kW to 455 kW.

Figure 4 shows the Corrected Counts/ kW*s for the SiC detector package placed in the TC as a function of neutron fluence. Two important observations from this figure are:

1) Up to $3x10^{12}$ n/cm^2 thermal neutron fluence, an increase in fluence caused a decrease in count rate per kW, which implies the build up of stable defects with increasing fluence.

2) Extrapolating Curve 2 (which was measured for a reactor power of 455 kW) to a lower fluence of $5.69x10^{11}$ n/cm^2 (the fluence for which the irradiations at 50 kW were terminated) yielded 90.1 counts per kW-s. But for the same fluence, Curve 1 (measured for a reactor power of 50 kW) yielded about 133.4 counts per kW-s. The differences between the extrapolated count rates for Curve 2 and the measured count rates for Curve 1 indicate the presence of a transient defect population that increases with increasing fluence rate and degrades the performance of the detector.

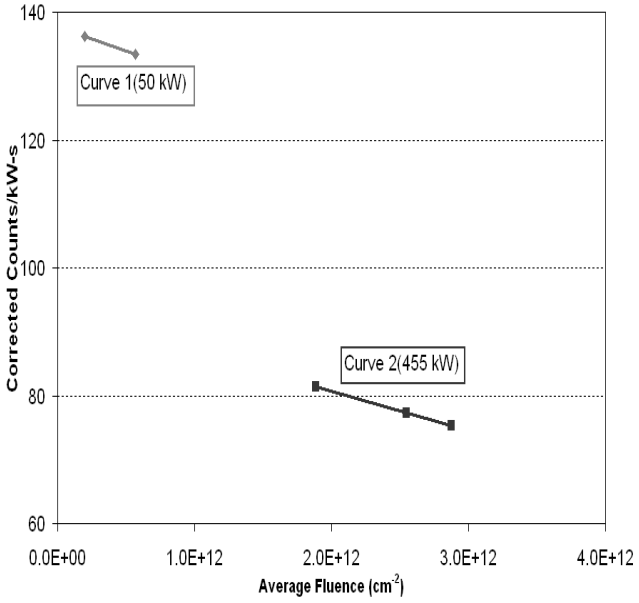

Figure 4 SiC detector normalized (per kW-s) count rate vs. average fluence. The reactor was operated at various power levels, as specified in the curve labels. (The fractional error on the data points for 50 kW is 0.5% and for 455 kW is 0.65%).

The change in the corrected counts per kW-s that was observed is due to the damage caused by the tritons in the SiC detector. These charged particles increase the number of trapping centers by displacing the atoms. As the free electrons, which contribute to the spectrum peak, are trapped at these trapping centers, the charge collection efficiency of the detector decreases, thus degrading its performance.

2.1.4.3 Detector Degradation Due to Accumulated Dose

To account for the accumulated dose effect, the SiC detector was irradiated at a constant full power (455 kW) for 11 hr in the TC and the effects of the prolonged irradiation on the detector performance were observed, as it is shown in Figure 5. One can observe from the figure that at fluences greater than $5x10^{13}$ n/cm^2, the count rate appears to remain constant. A slight increase in the count rate at fluence greater than $6x10^{13}$ n/cm^2 was also observed.

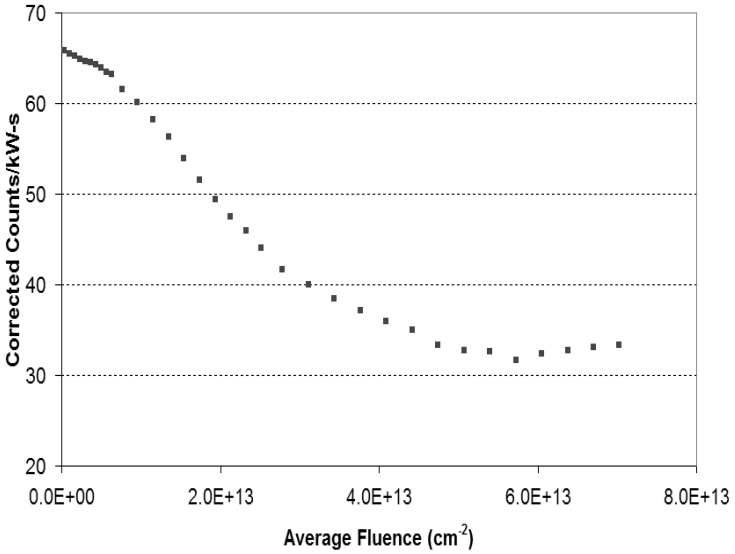

Figure 5 SiC detector normalized (per kW-s) count rate vs. average fluence. The reactor was operated at 455 kW for 11 hours. (The fractional error on the data points are 0.5%)

2.1.4.4 I-V Measurements

To study the degradation of the material and electrical properties of the diode due to radiation effects, I-V (current vs. voltage) measurements were recorded before and after neutron irradiations. A Keithley sourcemeter 2410 was used to record the forward characteristics of the diode.

To study the degradation of the material and electrical properties of the diode due to radiation effects, I-V (current vs. voltage) measurements were recorded before and after neutron irradiations. A Keithley sourcemeter 2410 was used to record the forward characteristics of the diode. The detector was forward biased when making the I-V measurements.

The I-V measurements that were recorded show the degradation of the detector performance due to the dose-rate effect. Figure 6 shows the increase in the forward resistance of the diode, as the detector was irradiated at different power levels. The power levels of the irradiations were chronologically ordered from lowest power to highest power. Thus, the results are integral in the sense that the curve labeled as "After 10 minutes at 50 kW" shows the damage resulting from irradiation at 1 kW for 1 hour followed by irradiation at 10 minutes at 50 kW. A similar statement can be made

regarding the irradiation history of the diode for the curve that is labeled as “After 15 minutes at 455 kW”. Consequently, the shift of the curve from the position of the preceding curve indicates the result of the incremental irradiation with which the curve is labeled. The shifting of the curves to lower currents for the same voltage results from an increase in the resistivity of the diode due to the more trapping centers.

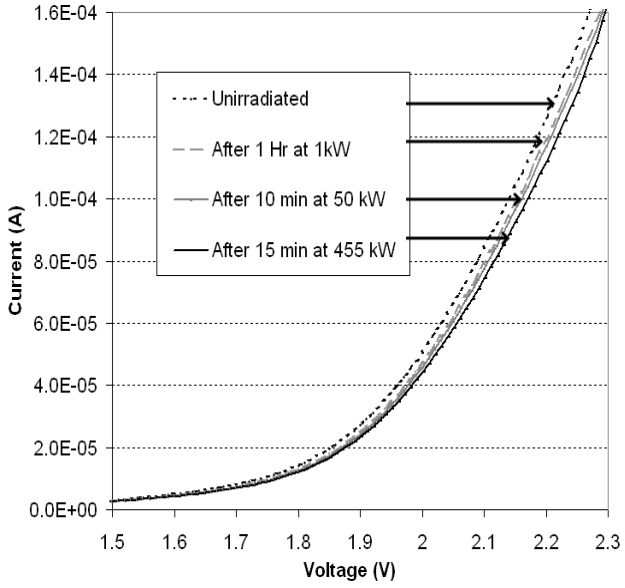

Figure 6 I-V measurements for the SiC detector, before and after irradiation at various power levels.

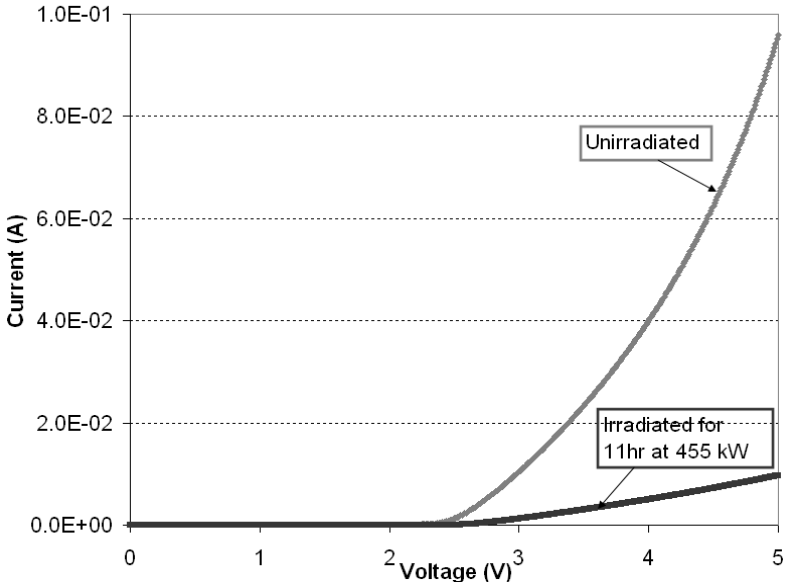

Figure 7 I-V measurements for the SiC detector, before and after 11 hr irradiation.

2.1.5 Comparative Study

The thermal neutron flux (2200m/s flux) measured experimentally using a gold foil in the TC yielded a flux of (2.2±0.07)x10^9 n/cm^2/s. The experimentally measured thermal neutron flux was multiplied by the volume of the LiF target and TRIM calculations of the total detection efficiency for tritons to predict the theoretical triton count rate.

Table I compares the experimental and theoretical triton count rates for the detector. Column 1 presents the experimental triton count rate for the detector placed in the TC. Column 2 presents the theoretical triton count rate, if the detector counts all the tritons which enter the SiC active volume.

Table I. Experimental and Theoretical count rates for the SiC detector

Experimental count rate (cps)	Theoretical count rate, assuming all incident tritons are counted (cps)
(2.90±.02)x10^4	(3.3±.099)x10^4

From Table I, one can observe that the theoretical and experimental count rates for the SiC detector are in close agreement with one another.

2.2 Conclusion

In this report, the degradation of the SiC detectors in the TC's thermal neutron environment was evaluated in terms of dose and dose rate effects. Irradiating the detector at 455 kW (the 2200 m/s fluence rate is 2.2×10^9 n/cm^2/s), the count rate per kW decreased by a factor of 2 after 11 hr. The I-V characteristics recorded during pre-irradiation and post-irradiation, confirm degradation of the detectors.

A theoretical model of the SiC Schottky diode detectors was constructed based on MCNP and TRIM computer codes to study the damage induced by tritons for a given diode detector package configuration in the TC's thermal neutron environment. The predicted count rate was compared with the experimental results that were obtained in the TC irradiation field of OSURR using a charge sensitive preamplifier. The experimental results are in agreement with the predicted response to within a factor of three.

I-V measurements show some annealing effects occuring at room temperature. Maintaining the detectors at a higher temperature during irradiation may cause more annealing to occur, thus reducing degradation of the detector. Experiments are necessary to test the degradation of the detector at elevated temperatures, to determine if the effects of annealing are sufficiently great so that the detectors may be useful for neutron power monitoring at high count rates.

References

[1] M. Reisi Fard, B. Khorsandi, T. E. Blue, J. Kulisek, and D.W. Miller, "Evaluation of the SiC Semiconductor Diode Detector Degradation in a Fast Neutron Flux," 5th International Topical Meeting on Nuclear Plant Instrumentation, Control and Human-Machine Interface Technologies (NPIC & HMIT 2006), Albuquerque, NM, Nov. 12-16 (2006).

[2] B. Khorsandi, M. Reisi Fard, T.E. Blue, D. Miller, and W. Windl, "Monte Carlo Modeling of Count Rates & Defects in SiC Detector Neutron Monitor System," Approved for publication in Nuclear Technology.

[3] A.J. Tavendale, "Semiconductor Nuclear Radiation Detectors," Annual Review of Nuclear Science, Vol. 17: 73-96 (Volume publication date December 1967).

[4] A.R. Dulloo, F.H. Ruddy, J.G. Seidel, J.M. Adams, J.S. Nico, and D.M. Gilliam, "The Thermal Neutron Response of Miniature Silicon Carbide Semiconductor

Detectors," Nuclear Instruments and Methods in Physics Research A, 498 (2003) 415-423.

[5] A.R. Dulloo, F.H. Ruddy, J.G. Seidel, C. Davison, T. Flinchbaugh, and T. Daubenspeck, "Simultaneous Measurements of Neutron and Gamma-Ray Radiation Levels from a TRIGA Reactor Core Using Silicon Carbide Semiconductor Detectors," IEEE Transactions on Nuclear Science, 46, 3 (1999) 275-279.

[6] S. Seshadri, A.R. Dulloo, F.H. Ruddy, J.G. Seidel, and L. B. Rowland, "Demonstration of an SiC Neutron Detector for High-Radiation Environments," IEEE Transactions on Electron Devices, 46, 3 (1999) 567-571.

[7] R.A. Forster, L.J. Cox, R.F. Barrett, T.E. Booth, J.F Briesmeister, F. B. Brown, J.S. Bull, C.G. Geisler, J.T Goorley, R.D. Mosteller, S.E. Post, R.E. Prael, E.C. Selcow, and A. Sood, "MCNP Version 5," Nuclear Instruments and Methods in Physics Research B, 213, 82 (2004).

[8] F.J. Ziegler, "SRIM-2003," Nuclear Instruments and Methods in Physics Research B, 219-220, 1027 (2004).

[9] J. Sroka, V. Krishnan, R. J. Chenkovich, and T. E. Blue, "MCNP Modeling of the Radiation Fields in the Functional Testing Vessel in Beam Port 1(Bp-1) of the OSURR," The American Nuclear Society's 14th Biennial Topical Meeting of the Radiation Protection and Shielding Division, Carlsbad New Mexico, USA. April 3-6, (2006).

[10] MCNP: A General Monte Carlo N-Particle Transport Code, Version 5, Los Alamos National Laboratory, Los Alamos, NM (2003).

4. Theses and Dissertations

As a product of this project, 3 M.S. theses and 2 Ph.D. dissertations were completed. The list of these documents is as follows:

M.S Theses:

1. Benone Lohan, "Nuclear Reactor Power Monitoring using SiC Semiconductor Radiation Detector in Gas Turbine Modular Helium Reactor," September 2004, Current employment: Westinghouse (Pittsburgh.)
2. Mehdi Reisi-Fard, "Nuclear Reactor Power Monitoring using SiC Semi-conductor Radiations Detectors," December, 2004. Graduate pursued Ph.D. (see below.)
3. Vijayalakshmi Krishnan, "Characterization of Effects of Mixed Neutron/Gamma Irradiation of SiC Neutron Power Monitors on their Recorded Pulse Height Distribution and I-V Curves," March 2007. Graduate is currently seeking employment in India.

Ph.D. Dissertations:

1. Mehdi Reisi-Fard, May 2006, "The Development of a High Count Rate Neutron Monitoring Channel Using Silicon Carbide Semiconductor Detectors." Current employment: NRC.

2. Behrooz Khorsandi, February 2007, "Simulation Modeling of Displacement Damage in the Silicon Carbide Detectors Resulting from Neutron Irradiation." Current employment: Candesco, Toronto, Canada.

5. Papers

As a product of this project, 4 High Level Journal Articles were written and published:

1. "Neutron Damage in SiC Semiconductor Radiation Detectors in the GT-MHR," T.E. Blue, B. Lohan, B. Khorsandi, and D.W. Miller, Journal of ASTM International, Vol.3, No.8, paper ID JAl13434, available online at www.astm.org, June, 2006.

2. "Trim Modeling of Displacement Damage in SIC for Monoenergetic Neutrons," B. Khorsandi, T.E. Blue, W. Windl, J. Kulisek, Journal ASTM Int., Vol. 3, No. 8, Paper ID JAl100358, available online at www.astm.org, June, 2006.

3. "Monte Carlo Modeling of Count Rates and Defects in Silicon Carbide Detector Neutron Monitor System, Highlighting GT-MHR, B. Khorsandi, M. Reisi Fard, T.E. Blue, D.W. Miller, W. Windl, Nuclear Technology, Vol. 159, No. 2, August 2007, pp: 208-220.

4. "Development of a Novel Dynamic Simulink Model of the GT-MHR Core," M. Reisi Fard, T.E. Blue, D.W. Miller, Nuclear Science and Engineering, Vol. 157, Number 3, pp: 316-330 (2007).

As a product of this project, 23 Refereed Articles were written and published:

1. "Simulation of a High Speed Counting System for SiC Neutron Sensors," M. Reisi Fard, T.E. Blue, D.W. Miller, F.H. Ruddy, A. R. Dulloo, J. G. Seidel, Trans. Am. Nucl., Vol. 90, Pittsburgh, PA (June, 2004), 352-353.

2. "A Mathematical Model of SiC Detector as Power Monitors," M. Reisi Fard, T. Blue, D. Miller, F. Ruddy, A. Dulloo, J. Seidel, Proceedings of the Forth American Nuclear Society International Topical Meeting on Nuclear Plant Instrumentation, Controls and Human-Machine Interface Technologies (NPIC&HMIT 2004) Columbus, OH, 947-954.

3. "Effect of Detector Capacitance and Cable on SiC Detector-Cable System Performance," M. Reisi Fard, T. Blue, D. Miller, Proceeding of the Forth American Nuclear Society International Topical Meeting on Nuclear Plant Instrumentation, Controls and Human-Machine Interface Technologies (NPIC&HMIT 2004) Columbus, OH, 955-965.

4. "The Dependence of Location Within Central Reflector on Detector Count Rate and Burn-Up for SiC Power Monitors in the GT-MHR," B. Lohan, T. Blue, D. Miller, Proceedings of the Forth American Nuclear Society International Topical Meeting on Nuclear Plant Instrumentation, Controls and Human-Machine

Interface Technologies (NPIC&HMIT 2004) Columbus, OH, 966-973.

5. "SiC Semiconductor Detector Power Monitors for Space Nuclear Reactors," M. Reisi Fard, T.E. Blue, and D.W. Miller, Space Technology and Applications International Forum-STAIF 2004, edited by M.S. El-Genk, February 2004, 574-581.

6. "Prediction of Radiation Damage in Silicon Carbide Semiconductor Radiation Detectors for Nuclear Reactor Power Monitoring in the GT-MHR," T. Blue, B. Lohan, B. Khorsandi, and D. Miller, 12th International Symposium on Reactor Dosimetry, May 8-13, 2005, Gatlinburg, TN, Flash Disk B.14.

7. "Predictions of Radiation Damage in SiC Neutron Power Monitors in IRIS," D. Berens, B. Khorsandi, B. Lohan, T. Blue, D. W. Miller, Transactions Vol.93, ANS 2005 Winter Meeting, November 13-15, 2005, Washington DC, on CD-ROM, pp 605-606 .

8. "GT-MHR Full Power Reactivity Insertion Transient Using a Novel Dynamic Simulink Model," M. Reisi Fard, T. Blue, D. Miller, Transactions Vol.93, ANS 2005 Winter Meeting, November 13-15, 2005, Washington DC, on CD-ROM, pp 934-935 .

9. "Radiation Damage in SiC Neutron Power Monitors in the GT-MHR," T. Blue, B. Lohan, B. Khorsandi, D. Miller, Transactions Vol.93, ANS 2005 Winter Meeting, November 13-15, 2005, Washington DC, on CD-ROM, pp 607-609 .

10. "Production of Vacancies in SiC Detectors after Irradiation with Monoenergetic Neutrons," B. Khorsandi, T.E. Blue, J. Kulisek, W. Windl, D. Miller, , Transactions Vol.93, ANS 2005 Winter Meeting, November 13-15, 2005, Washington DC, on CD-ROM, pp 425-426.

11. "MCNP Modeling of the Radiation Fields in the Functional Testing Vessel in Beamport 1 (BP-1) of the OSURR," J. Sroka, V. Krishnan, R.J. Chenkovich, and T.E. Blue, Proceedings of the ANS 14th Biennial Topical meeting of RPSD, Carlsbad, NM, April 1-8, 2006, pp: 345-347.

12. "The Use of Monte Carlo Methods to Study the Creation and Evolution of Defects in SiC Detectors irradiated by Neutrons," B. Khorsandi, T.E. Blue, J. Kulisek, W. Windl, D. Miller, Proceedings of the ANS 14th Biennial Topical Meeting of the RPSD, Carlsbad, NM, April 1-8, 2006, pp: 262-264.

13. "Predictions of Displacement Damage and Count Rate for SiC Detectors in IRIS," B. Khorsandi, B. Lohan, T.E. Blue, D. Miller, J. Kulisek, Proceedings of ICAPP '06, June 4-8, 2006, Reno, NV, paper 6316 on CD-ROM.

14. "GT-MHR Start-up Reactivity Insertion Transient Analysis Using Simulink," M. Reisi-Fard, T.E. Blue, D.W. Miller, Proceedings of ICAPP '06, June 4-8, 2006, Reno, NV, paper 6326, on CD-ROM.

15. "Reactor Power Monitoring Using Silicon Carbide Fast Neutron Detectors, " F. Ruddy, J. Seidel, T.E. Blue, and D.W. Miller, PHYSOR-2006, ANS Topical Meeting on Reactor Physics, September 10-14, 2006, Vancouver, BC, Canada, C162, CD-ROM.

16. "A Feasibility Study for 4H-SiC Diode Detectors as Neutron Flux Monitors in the GT-MHR," B. Khorsandi, M. Reisi-Fard, T.E. Blue, J. Kulisek, B. Lohan, and D.W. Miller, PHYSOR-2006, ANS Topical Meeting on Reactor Physics, September 10-14, 2006, Vancouver, BC, Canada, C161, CD-ROM.

17. "4H-SiC Based Neutron Flux Monitors in Very High Temperature Nuclear Reactors," B. Khorsandi, W. Windl, T.E. Blue, W. Luo, J. Kulisek, M. Reisi-Fard, V. Krishnan, Proceedings of Materials Science & Technology (MS&T) 2006: Fundamentals and Characterization: Vol.2, Radiation Effects in Materials, Organized by R. Devanathan, L.W. Hobbs, B.D. Wirth, and K. Yasuda, Cincinnati, OH, October 15-19, 2006, CD pp: 307-315.

18. "Evaluation of a High Speed Neutron Counting System Using SiC Semiconductor Detector," M Reisi-Fard, V. Krishnan, T.E. Blue, D.W. Miller, 5th International Topical Meeting on Nuclear Plant Instrumentation, Control and Human-Machine Interface Technologies, NSA Winter Meeting, November 2006, Albuquerque, NM, CD pp: 628-636.

19. "Evaluation of SiC Semiconductor Diode Detector Degradation in a Fast Neutron Flux," M. Reisi-Fard, B. Khorsandi, T.E. Blue, J. Kulisek, D.W. Miller, 5th International Topical Meeting on Nuclear Plant Instrumentation, Control and Human-Machine Interface Technologies, NSA Winter Meeting, November 2006, Albuquerque, NM, CD pp: 1066-1073.

20. "Theoretical and Experimental Analysis of Response of SiC in Thermal Neutron Environment," V. Krishnan, B. Khorsandi, J. Kulisek, D. Hawn, T.E. Blue, D.W. Miller, Transactions of the ANS 2007 Annual Meeting, Vol. 96, Boston, MA, June 2007, CD Rom pp: 705-706.

21. "Effect of Fast Neutron Damage on Linearity of a SiC Semiconductor Detector Monitoring System," M. Reisi Fard, T.E. Blue, D.W. Miller, Transactions of the ANS 2007 Annual Meeting, Vol. 96, CD Rom, Boston, MA, June 2007, pp: 701-702.

22. "A Method to Estimate the Lifetime of SiC Semiconductor Detectors in Next Generation Reactors," B. Khorsandi, M. Reisi Fard, T. Blue, D.W. Miller, Transactions of the ANS 2007 Annual Meeting, Vol. 96, Boston, MA, June 2007, CD Rom pp: 703-704.

23. "Multiscale Modeling of Damage in SiC Detectors in GT-MHR Central Reflector," B. Khorsandi, J. Chenkovich, T.E. Blue, W. Windl, J. Kulisek, D.W. Miller, Transactions of the ANS 2007 Annual Meeting, Vol. 96, Boston, MA, June 2007, CD Rom pp: 677-678.

Journal of ASTM International, Vol. 3, No. 8
Paper ID JAI13434
Available online at www.astm.org

T. E. Blue,[1] *B. Lohan,*[2] *B. Khorsandi,*[3] *and D. W. Miller*[1]

Neutron Damage in SiC Semiconductor Radiation Detectors in the GT-MHR

ABSTRACT: As a part of a U.S. Department of Energy Nuclear Engineering Research Initiative (NERI) project, we are evaluating the potential for using silicon carbide (SiC) semiconductor radiation detectors, operating in the pulse mode, as power monitors for gas turbine modular helium reactor (GT-MHR) [1]. Locations for the power monitors will be selected considering acceptable detector count rates and lifetimes. We have characterized the radiation environment at various locations in the GT-MHR, where detectors may be placed, in terms of the 1 MeV equivalent neutron flux in SiC ($\phi_{eq,1\ MeV,\ SiC}^{Total}$). Also, we have characterized the radiation field in beam part 1 (BP1) of the Ohio State University Research Reactor (OSURR) in these same terms, with the intent of correlating observed degradation of the SiC detectors in the OSURR to the degradation that can be expected for various detector locations in the GT-MHR. Comparing $\phi_{eq,1\ MeV,\ SiC}^{Total}$ for the GT-MHR and for the OSURR, we conclude that SiC devices cannot be adequately tested in the characterization vessel in OSURR BP1 for the radiation damage that would be incurred over a refueling cycle for detectors placed in-core. Also, we note that the radiation environment in the OSURR BP1 is harder than the radiation environment in the GT-MHR.

KEYWORDS: GT-MHR, displacement damage kerma factor, 1 MeV equivalent neutron fulx, MCNP

Nomenclature

Indices

mat = material
eq = equivalent

Abbreviations

GT-MHR = gas turbine modular helium reactor
OSURR = Ohio State University Research Reactor
BP1 = beam port 1
RC = reactor cavity
RCCS = reactor cavity cooling system

Greek symbols

ϕ = flux
ν = number of neutrons produced per fission

Latin symbols

H = hardness factor
E = energy
F = damage function
R = radius
$\dot{S}_n$ = neutron production rate

Manuscript received June 20, 2005; accepted for publication May 17, 2006; published online June 2006. Presented at ASTM Symposium on Reactor Dosimetry, 12th International Symposium on 8–13 May 2005 in Gatlinburg, TN; D. W. Vehar, D M. Gilliam, and J. M. Admas, Guest Editors.
[1] Professor, The Ohio State University, Nuclear Engineering Program, Columbus, OH 43202.
[2] Engineer, Westinghouse Electric Company, Monroeville, PA, 15146.
[3] Graduate Student, The Ohio State University, Nuclear Engineering Program, Columbus, OH 43202.

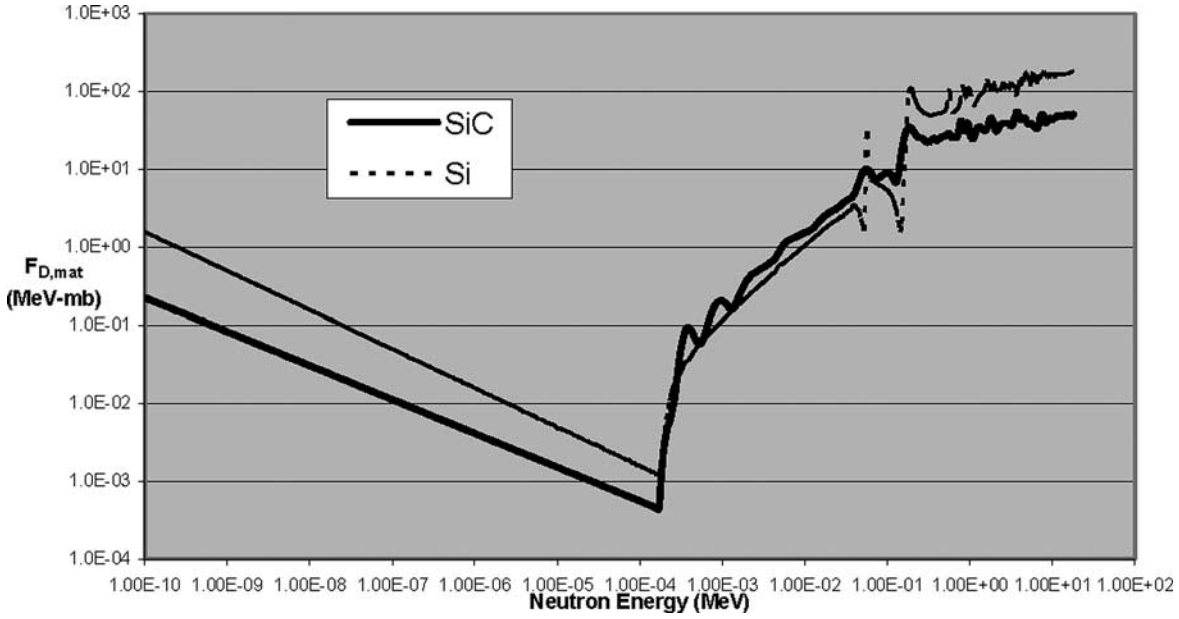

FIG. 1—*The damage functions (the displacement damage kerma factors) for* Si$[F_{D,\mathrm{Si}}(E)]$ *and* SiC$[F_{D,\mathrm{SiC}}(E)]$*: Logarithmic scales are used for the ordinate and for the abscissa.*

$\dot{d}$ = damage rate

Introduction

This paper describes the results of our efforts to characterize the radiation environment at various locations in the gas turbine modular helium Reactor (GT-MHR) where detectors may be placed, and in beam part 1 (BP1) of the Ohio State University Research Reactor (OSURR) in terms of $\phi^{\mathrm{Total}}_{\mathrm{eq,1\ MeV,mat}}$ (ASTM E 722-94) [2]. Displacement damage arising from gamma-ray interactions is insignificant and is not included in our analysis. Displacement damage arising from Si and C atoms recoiling in radiative capture events is included in the displacement damage kerma factor which is discussed below.

For the purpose of predicting detector lifetime, one is interested in knowing the displacement damage rate $\dot{d}$. It can be calculated with knowledge of the energy integrated neutron flux (ϕ^{Total}) (also called the total neutron flux) and the hardness factor (H_{mat}), where

$$H_{\mathrm{mat}} = \phi^{\mathrm{Total}}_{\mathrm{eq,1\ meV,mat}}/\phi^{\mathrm{Total}} \tag{1}$$

$$\phi^{\mathrm{Total}} = \int_0^{\infty} \phi(E)dE \tag{2}$$

and the total 1 MeV equivalent neutron flux $\phi^{\mathrm{Total}}_{\mathrm{eq,1\ MeV,mat}}$ is defined as:

$$\phi^{\mathrm{Total}}_{\mathrm{eq,1\ meV,mat}} = \int_0^{\infty} \frac{F_{D,\mathrm{mat}}(E)}{F_{D,1\ \mathrm{MeV,mat}}}\phi(E)dE \tag{3}$$

where $F_{D,\mathrm{mat}}(E)$ is the damage function (the displacement damage kerma factor), which is given below in Fig. 1 for Si and SiC. In this figure, $F_{D,\mathrm{Si}}(E)$ is from ASTM Standard 722-94. Data given by Heinisch et al. [3] was used to estimate $F_{D,\mathrm{SiC}}(E)$, assuming the average E_d for SiC is 22 eV [4].

With a knowledge of $F_{D,1\ \mathrm{MeV,mat}}$ and $\phi^{\mathrm{Total}}_{\mathrm{eq,1\ MeV,mat}}$, or with a knowledge of $F_{D,1\ \mathrm{MeV,mat}}$, H_{mat}, and ϕ^{Total}, one can calculate $\dot{d}$ as

$$\dot{d} = F_{D,1\ \mathrm{MeV,mat}}\phi^{\mathrm{Total}}_{\mathrm{eq,1\ meV,mat}} = F_{D,1\ \mathrm{MeV,mat}}H_{\mathrm{mat}}\phi^{\mathrm{Total}} \tag{4}$$

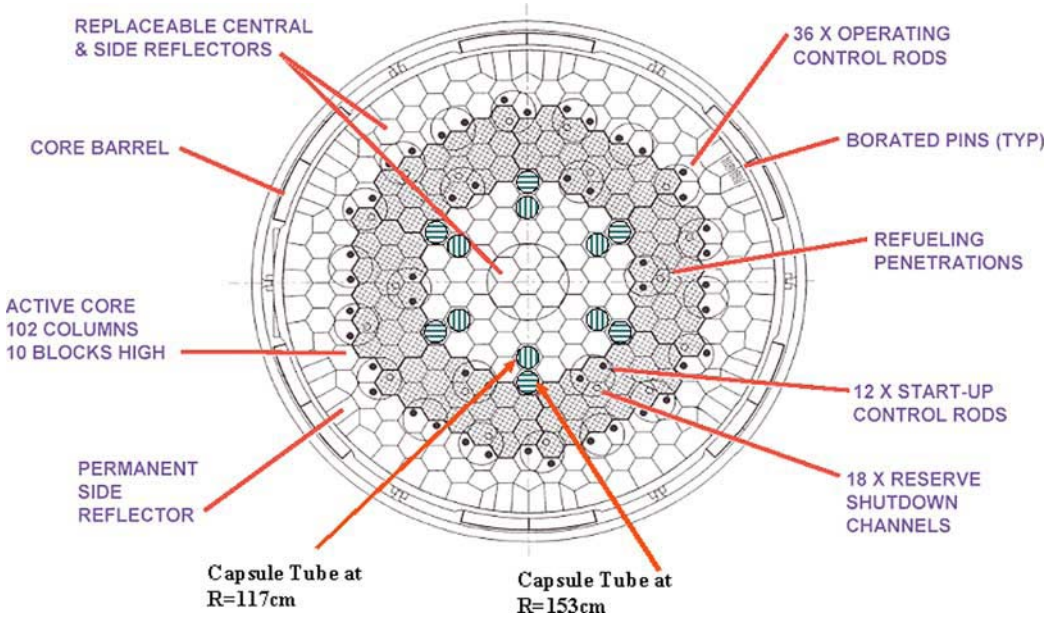

FIG. 2—*Core arrangement and the capsule tube positions. It should be noted that the capsule tubes are not in the original design of GT-MHR.*

In this paper, we present and compare values of $\phi^{\text{Total}}_{\text{eq,1 MeV,mat}}$ and H_{mat} calculated for SiC in the GT-MHR and in the OSURR BP1.

Background

GT-MHR

This section provides background information about the GT-MHR conceptual design based on the General Atomics report submitted to U.S. Nuclear Regulatory Commission [1]. The primary components for each module are reactor vessel and power conversion vessel, connected by a cross vessel. The vessel systems are located inside an underground silo 23.9 m in diameter × 42.7 m deep, which serves as the containment structure. The reactor vessel is made of high strength alloy steel and is approximately 7.58 m in diameter and about 31.2 m high. It contains the reactor core, core supports, internal structure, reactivity control assemblies, and hot duct.

The reactor core consists of hexagonal fuel and reflector elements, plenum elements, and reactivity control material, all located inside a reactor pressure vessel. The core is designed to provide 600 MW thermal (MWth) at a power density of 6.6 MW/m^3. The active core consists of an assembly of hexagonal graphite fuel elements (blocks) containing blind holes for fuel compacts and full-length channels for helium coolant flow. Figure 2 presents a cross section of the reactor vessel. The active fuel region of the core consists of 102 fuel columns that are ten blocks high, arranged in three annular rings. Above and below the active core there are upper and lower replaceable reflectors. The reflector above the active core is composed of one and one-half layers of H-451 graphite, for a total reflector height of 1.2 m. The reflector below the core has a total height of 1.6 m. It consists of two layers: one layer of two half-height reflector elements above a layer of two half-height flow distribution and supports elements.

The active core has columns of hexagonal graphite reflector elements in the inner and outer regions. The outer side reflector is split into two rows of replaceable reflector and one row of permanent side reflector. The permanent side reflector blocks are solid except for the inclusion of boronated steel pins, which act as neutron absorber poisons. A metallic core support, the core barrel, is provided around the outside of the core assembly for lateral support. The core is cooled by helium, which flows through the outer annulus within the cross vessel, up the core inlet riser channels located between the core barrel and

TABLE 1—*Geometrical data for MCNP GT-MHR model for in-core detector positions.*

Region number	Region	Hexagonal flat-to-flat (cm)	Inner diameter (cm)	Outer diameter (cm)	Height (cm)
1	Core	467.65	…	…	800
2	Central replaceable reflector	…	…	…	1080
	Ring 1	93.52	…	…	1080
	Ring 2	155.88	…	…	1080
	Ring 3	218.23	…	…	1080
	Ring 4	280.59	…	…	1080
3	Side reflector	…	…	617.6	1080
4	Upper replaceable reflector	…	…	484.0	120
5	Lower replaceable reflector	…	…	484.0	160
6	Permanent side reflector	…	617.6	671.0	1080
7	Permanent side reflector with boron carbide pins	…	671.0	682.0	1080
8	Core barrel	…	682.0	693.0	1080
9	He	…	693.0	720.0	1080
10	Gas duct shell	…	704.5	708.5	1080
11	Reactor vessel	…	720.0	758.0	1080
11	Reactor vessel flange	…	720.0	854.0	100
12	Reactor cavity	…	758.0	1180.0	1080
13	RCCS wall	…	1180.0	1212	1080
15	Cavity liner	…	1280.0	1281.2	1080
16	Concrete	…	1281.2	1341.2	1080
17	Capsule—inner tube	…	3.89	4.22	1080
18	Capsule—outer tube	…	6.66	8.89	1080
20	Porous carbon	…	9.70	14.90	1080

reactor vessel, and finally down through the core. The helium that is flowing into the reactor vessel is the working fluid in the power conversion system as well. GT-MHR operates at an elevated temperature with helium inlet temperatures of 491°C and outlet temperatures of 850°C.

The reactor vessel is surrounded by a reactor cavity cooling system (RCCS). The RCCS removes heat from the reactor vessel by radiation and natural convection from the uninsulated vessel. It also protects the concrete wall of the reactor cavity from exceeding design temperature limits for all modes of operation. The RCCS includes a cooling panel placed around the reactor vessel. Heat is removed from the reactor cavity by natural circulation of outside air through the RCCS cooling panels.

Methods

MCNP Computer Model

A model for the GT-MHR in-core detectors within capsule tubes (henceforth called simply "capsules") in the central reflector was designed using MCNP [4] version 4C. The computer model consists of a geometric representation of the GT-MHR core, reactor vessel, capsule, cavity, and RCCS. The model includes a particle specific source term, neutron and photon tallies, and variance reduction techniques to allow for accurate as well as timely results. The model was run on UNIX based computer systems.

The GT-MHR reactor geometry is defined in MCNP using a series of vertical surfaces and horizontal planes. Consequently, all the regions of the reactor have finite length. Table 1 presents the geometrical data for the all regions of the in-core detector model.

The central reflector (2) consists of graphite hexagonal elements, with a distance between flats of 46.76 cm (the distance between two opposite sides of the hexagon), that occupy the central region of the reactor. The central reflector's hexagonal shape allows six locations for the placement of the capsules. We have considered placing the capsules within the central reflector at 0, 60, 120, 180, 240, and 300 deg, as shown in Fig. 2. Moreover, we have considered placing the capsules at two different radii, first at $R = 153$ cm and second at $R = 117$ cm.

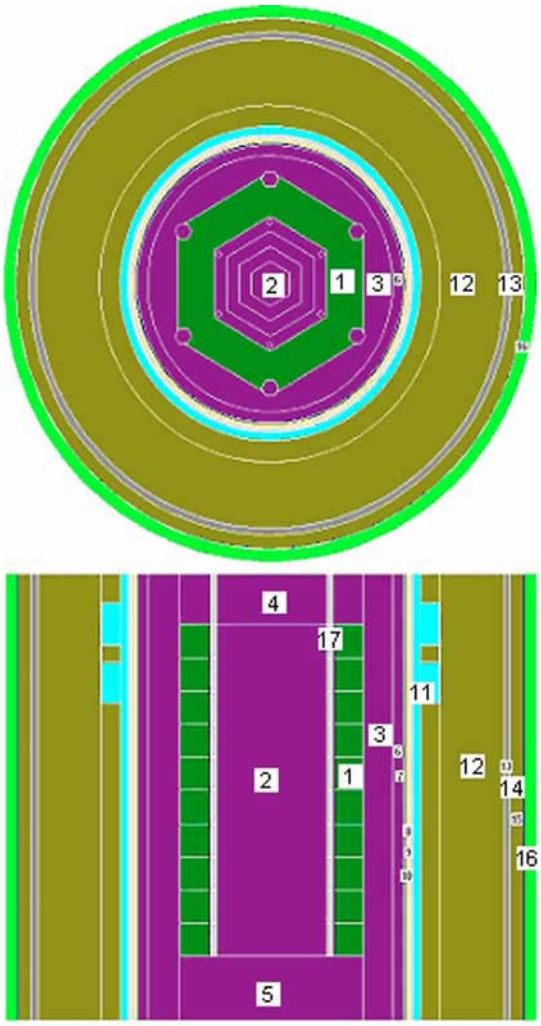

Legend

1. Core	5. Lower Ref.	10. Gas Duct Shell	14. Air RCCS
2. Central Ref.	6. Permanent Ref.	11. Reactor Vessel	15. Cavity Liner
3. Side Ref.	7. Boron Pins	12. Reactor Cavity	16. Concrete
4. Upper Ref.	8. Core Barrel	13. RCCS	17. Capsule Tube

FIG. 3—*Cross section of the MCNP GT-MHR model for in-core detector positions.*

Figure 3 presents transverse and lateral cross sections of the MCNP GT-MHR in-core model. The model is described below outwardly from the center of the core.

The fueled region of the GT-MHR core (1) was defined as existing between the boundaries of two hexagons. The inner hexagon has a distance between flats of 280.592 cm and the outer hexagon has a distance between flats of 467.724 cm. Moreover, six prismatic elements of the outer side reflector (3) are inserted into the active core in order to match as closely as possible the real geometry. The active core volume was divided into ten axial layers according to height of the hexagonal graphite fuel elements of which the core is composed. As can be seen in Fig. 3, above and below the core, there are, respectively, an upper replaceable reflector (4) and a lower replaceable reflector (5). The height of the upper reflector is one and one-half blocks (120 cm), and the height of the lower reflector is two blocks (160 cm). The active core volume is surrounded radially by the outer side replaceable reflector (3). The outer side replaceable reflector is surrounded by an annular region, which defines the permanent side reflector (6). The permanent side reflector is surrounded by a region which contains the boron carbide pins (7). The region of boron carbide pins is surrounded by the core barrel (8). Outboard of the core barrel, between the outer surface of the core barrel and the inner surface of the reactor vessel, there are two annular regions with helium (9), divided by a gas duct shell (10). An annular region defines the reactor vessel wall (11). Outboard of this

annular region, two ring regions define the reactor vessel flanges. Between the reactor vessel and the RCCS there are cells filled with air (12). The RCCS panel (13), cavity liner (15), and concrete wall (16) were modeled in detail as a part of an ex-core detector model. The detailed description of those elements of the model is not relevant for calculations for detector locations within the core, so, for this reason, we will not discuss them further. A sphere with a radius of 900 cm surrounds the MCNP GT-MHR in-core model. This sphere defines the "universe" for the Monte Carlo calculation. Particles transported outside of this sphere are ignored.

Material Cards and Cross-Section Libraries for GT-MHR

The material composition for each the structural elements that are listed in the legend was defined in the MCNP model as a homogenous mixture for a core completely loaded with fresh fuel. The homogenization of the fuel and binder in the core was judged to be adequate for our calculations, since, as described below, the source was defined with an axial power profile that was generated using a more detailed model geometry. The cross-section libraries used to perform the computations are based on the Evaluated Nuclear Data Files ENDF/B-VI. For carbon, the neutron scattering $S(\alpha,\beta)$ thermal treatment was taken into account. Furthermore, for each cell in the model, the temperature was indicated in order to take into account the Doppler effect. For the MCNP GT-MHR model, the neutron multiplication by fission was turned off by setting a "nonu" card to zero for all cells in the model.

Characteristics of the Neutron Source for GT-MHR

In the GT-MHR model, the source was defined in active core cells. The source was assigned an axial probability distribution function, based upon the power in ten core vertical cells. The relative probability of a source neutron being emitted from a cell was proportional to the cells contribution to the axial power profile. Each source within a cell was modeled as an isotropic neutron source uniformly distributed within the cell. The energy distribution of source neutrons was sampled using the watt neutron spectrum for U-235.

The neutron production rate ($\dot{S}_n$) was used to calculate the absolute neutron flux based on the flux per source particle that MCNP yields. The neutron production rate was calculated based on the thermal power of the core, which was assumed to be 600 MWth, the average fission neutron energy that is converted into thermal energy (E_f), which was assumed to be 190 MeV, and the number of neutrons produced per fission (ν), which was assumed to be 2.43.

Particle Tallies for GT-MHR Models

Tally number four yields the flux averaged over a volume and normalized on a per source particle basis. For the in-core detector model, tally number four was chosen to provide neutron flux values in ten cells in the capsule. The heights of the tally volumes correspond to the lengths of the corresponding fuel blocks. The neutron flux tally output was split into 101 energy bin groups plus one bin for the total flux. Thus, for an individual cell it is possible to determine the neutron flux energy spectrum.

Tally number two yields the flux, averaged over a surface and normalized to the number of source particles

The variance reduction techniques that were applied are geometrical splitting and energy splitting. For the detector tallies, the MCNP cases were run until the errors in the total fluence were smaller than 5 %.

Results

As an example of the results that were obtained, Fig. 4 shows the neutron energy spectra (neutron flux per MeV) for both in-core positions $R=153$ cm and $R=117$ cm, at $Z=320$ cm. For $R=153$ cm the neutron flux energy spectra is shown within the capsule and in the absence of the capsule. As can be seen, the presence of the capsule causes the thermal neutron flux to be smaller within the capsule than it is without the capsule, due to the absorption of thermal neutrons in the capsule wall.

Results similar to those shown in Fig. 4 were obtained at other in-core locations. The spectra that were obtained were processed using Eqs 1–3 to obtain $\phi^{\text{Total}}_{\text{eq,1 MeV,SiC}}$ and H_{SiC}.

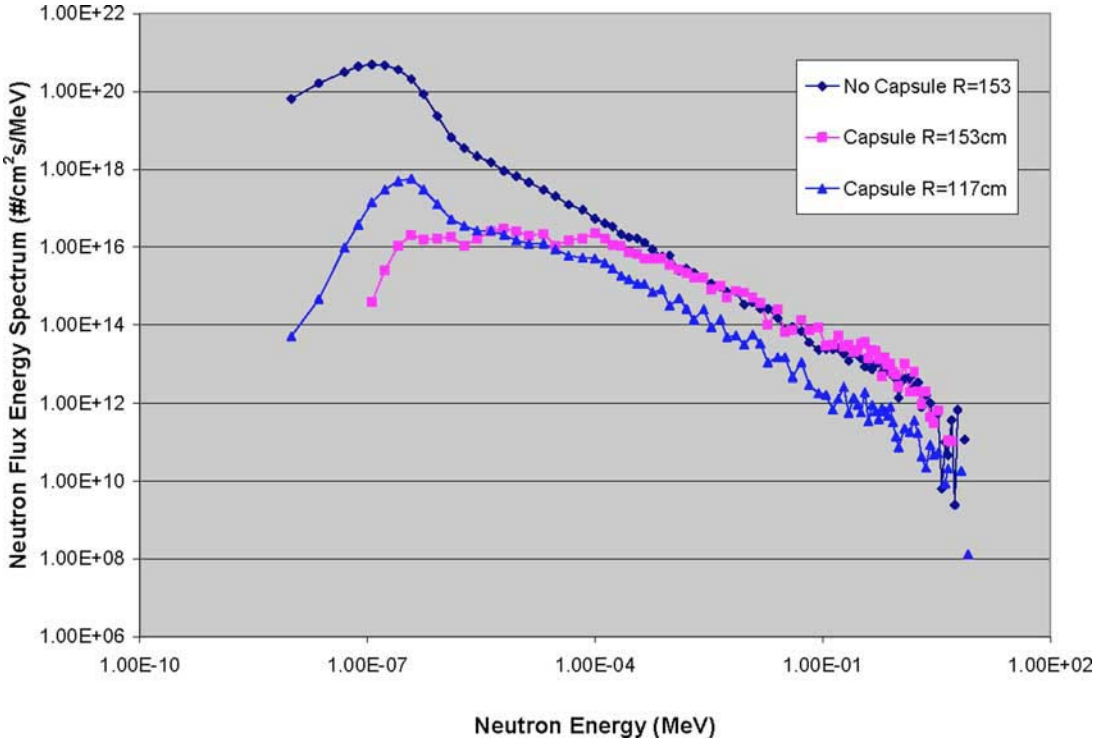

FIG. 4—*Neutron flux energy spectra for in-core positions at R*=153 *cm and Z*=320 *cm (with and without the capsule), R*=117 *cm and Z*=320 *cm, for full power operation* (*P*=600 *MWth*).

Figure 5 presents a graph of $\phi^{\text{Total}}_{\text{eq,1 MeV,SiC}}$ for two in-core radii (117 cm and 153 cm) and three axial positions for the GT-MHR reactor core. Figure 6 presents H_{SiC} versus axial layer, with radius as a parameter, for the same detector positions as for Fig. 5. For purposes of comparison, $\phi^{\text{Total}}_{\text{eq,1 MeV,SiC}}$ and H_{SiC} are presented in these figures for ex-core locations at the indicated radii in the RC (Region 12 in Fig. 3) and in the RCCS air (Region 14 in Fig. 3).

For purposes of comparison, $\phi^{\text{Total}}_{\text{eq,1 MeV,SiC}}$ were calculated in the manner described above for Position 4 in the semiconductor device characterization vessel in Beam Port 1 (BP1) of the OSURR. The values of $\phi(E)$ that were used in the calculations were determined using foil activation data and the SAND-II

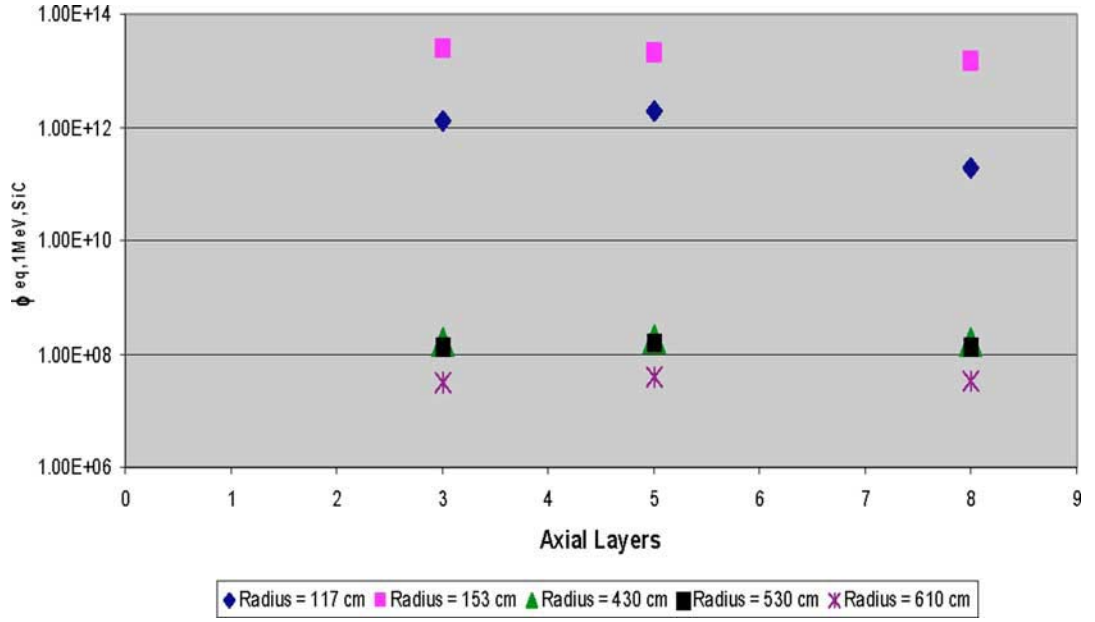

FIG. 5—$\phi^{\text{Total}}_{\text{eq,1 MeV,SiC}}$ *versus reactor layer, with radii as a parameter, for five in-core radii.*

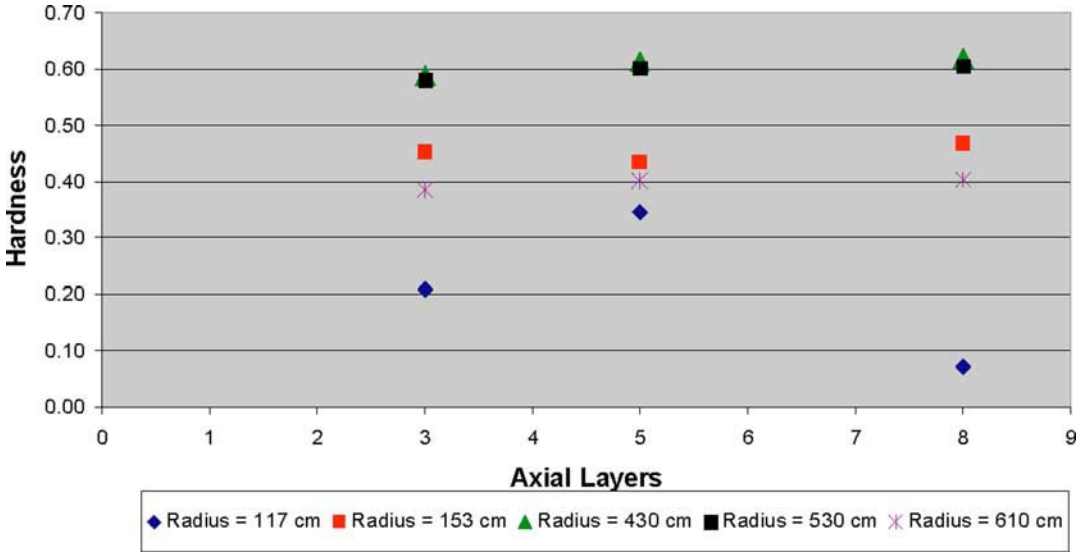

FIG. 6—*Hardness plot for five in-core radii as a function of reactor axial layer.*

neutron energy spectrum deconvolution code. The results of the calculations are $\phi^{\text{Total}}_{\text{eq,1 MeV,SiC}}=7.20 \times 10^{11}$ neutrons $\text{cm}^{-2}\,\text{s}^{-1}$ for operation at 500 kW (nominal full power). Also, $H_{\text{SiC}}=0.66$

In conclusion, it can be seen by comparing the values of $\phi^{\text{Total}}_{\text{eq,1 MeV,SiC}}$ and H_{SiC} for the GT-MHR with the value of $\phi^{\text{Total}}_{\text{eq,1MeV,SiC}}$ and H_{SiC} for the OSURR, that SiC devices cannot be adequately tested in the characterization vessel in BP1 of the OSURR, for the radiation damage that would be incurred over a refueling cycle, for detectors located in core in the GT-MHR. Although the differences in the radiation hardness, between the characterization vessel in BP1 of the OSURR and the GT-MHR for in-core locations, can be compensated for by simply irradiating the devices to equal 1 MeV equivalent neutron fluence ($\Phi^{\text{Total}}_{\text{eq.,1 MeV,SiC}}$); equal ($\Phi^{\text{Total}}_{\text{eq.,1 MeV,SiC}}$) cannot be practically attained in a reasonable time, since the OSURR is run only upon demand (which is on average a small fraction of a working day) and not often at full power. An analysis of ex-core locations is underway.

Acknowledgments

This material is based upon work supported by the U.S. Department of Energy under the NERI program Award No. DE-FG-07-02SF22620 and NERI Project Number 02-207. Any opinions, findings, and conclusions or recommendations expressed in this material are those of the authors and do not necessarily reflect the views of the Department of Energy.

References

[1] General Atomics, "Gas Turbine-Modular Helium Reactor (GT-MHR) Conceptual Design Description Report," Project No. 7658 1996.

[2] ASTM, Standard E 722-94, "Standard Practice for Characterization Neutron Energy Fluence Spectra in Terms of an Equivalent Monoenergetic Neutron Fluence for Radiation-Hardness Testing of Electronics," *Annual Book of ASTM Standards*, Vol. 12.02, ASTM International, West Conshohocken, PA, pp. 318–333.

[3] Heinisch, H. L., Greenwood, L. R., Weber, W. J., and Williford, R. E., "Displacement Damage in Silicon Carbide Irradiated in Fission Reactors," *J. Nucl. Mater.*, Vol. 327, 2004, pp. 175–181.

[4] Devanathan, R., Weber, W. J., and Gao, F., "Atomic Scale Simulation of Defect Production in Irradiated 3C-SiC," *J. Appl. Phys.*, Vol. 90, No. 5, 2001, pp. 2303–2309.

[5] Briesmeister, J. F. ed., "MCNP-A General Monte Carlo N-Particle Transport Code, Version 4C," Los Alamos National Laboratory Report No. LA-13709, 2000.

Journal of ASTM International, Vol. 3, No. 8
Paper ID JAI100358
Available online at www.astm.org

B. Khorsandi,[1] *T. E. Blue,*[2] *W. Windl,*[3] *and J. Kulisek*[1]

TRIM Modeling of Displacement Damage in SiC for Monoenergetic Neutrons

ABSTRACT: Although silicon carbide is a very good semiconductor material for the fabrication of diode detectors for use as neutron power monitors in nuclear reactors, the electrical properties of the diodes may be altered because of interactions between energetic neutrons and SiC atoms. If the energy that is transferred from a neutron to an atom in a collision exceeds some threshold value, the atom will be moved from its original position, creating displacement damage. Accurately modeling displacement damage is a first step to finding ways to eliminate or decrease the amount of damage the displacements induce. The methodology that we have used to estimate the number of displacements per atom per fluence, using two codes (MCNP and TRIM) is presented in this paper, along with examples of the results of our calculations.

KEYWORDS: displacement damage, MCNP, TRIM, PKA

Introduction

Silicon carbide (SiC) semiconductor diode detectors that are operated in the pulse mode may prove to be useful as neutron power monitors for Generation IV nuclear reactors. As a semiconductor material, SiC has very good thermal, chemical, neutronic, and electrical properties, particularly at high temperatures. Compared to Si, SiC is a radiation hard material; however, like Si, the properties of SiC are changed by irradiation by a large fluence of energetic neutrons, as a consequence of displacement damage. Since predictions of displacement damage and the concomitant radiation effects are important for deciding where the SiC detectors should be placed, we discuss below our efforts to quantify the displacement damage that may be expected to occur as a consequence of neutron irradiation of SiC diode detectors.

In studies of displacement damage, one attempts to estimate the number and configuration of displacements created by projectile particles [1]. The study of displacement damage does not deal specifically with the effects of radiation, the impact of time or temperature, or the recovery of defects. These are considerations in the study of radiation effects; however, the accurate prediction of displacement damage is a first step in the accurate prediction of radiation effects.

In a classic paper, Kinchin and Pease introduced a simple model to estimate the number of displacements per primary knock-on atom (PKA) [2]. Later, Norgett et al. proposed a method to approximate the number of Frenkel pairs that are created by energetic particles more accurately [3]. Because of the importance of these analytic formulations, later in this paper, predictions of displacement damage that we have obtained using detailed Monte Carlo modeling are compared with predictions of displacement damage made using these simple models. Coulter and Parkin formulated the displacement damage methodology for polyatomic materials [4,5].

Most modeling of neutron induced displacement damage, until recent times, has been focused on structural materials, especially iron. Notable among the papers that are not focused on iron is the paper by Lee and Farnum [6] that used SPECTER [7] and TRIM [8] to estimate the number of vacancies per neutron in alumina. The methods that we have used in this paper are similar to the methods that Lee and Farnum have used in that both we and they have predicted PKA source distributions with a computer code and used the resultant PKA source distributions as input to TRIM. However, our methods are different in that

Manuscript received June 20, 2005; accepted for publication May 5, 2006; published online June 2006. Presented at ASTM Symposium on Reactor Dosimetry, 12th International Symposium on 8–13 May 2005 in Gatlinburg, TN; D. W. Vehar, D. M. Gilliam, and J. M. Adams, Guest Editors.

[1] Graduate Student, Ohio State University, Nuclear Engineering Program, Columbus, OH 43202.
[2] Professor, Ohio State University, Nuclear Engineering Program, Columbus, OH 43202.
[3] Professor, Ohio State University, Department of Materials Science and Engineering, Columbus, OH 43210.

our calculations of the PKA source have been generated using the Monte Carlo code MCNP5 [9] with cross sections that are continuous in energy, whereas their PKA source has been generated by using SPECTER. As an additional point of reference, Weber et al. at PNNL have estimated the number of displacements per PKA [10] for SiC as a function of the PKA energy.

In this paper, we describe the methods that we have used to estimate the number of C- and Si-displacements, using two powerful computer codes—MCNP5 and SRIM/TRIM 2003—in combination. Our focus is to determine the displacements per atom (DPA) per fluence. This term (DPA/fluence) is useful for comparing the number of displacements created by various fluences of various projectiles irradiating various target materials.

Displacement Damage Equations

Transferred Energy to PKA

Based on binary collision theory, if a neutron, with energy E_n, collides with an atom in the target, the energy transfer in the elastic collision is given by the expression

$$T = \frac{1}{2}\Lambda E_n(1 - \cos\theta) \tag{1}$$

where T is the kinetic energy of the PKA and θ is the neutron scattering angle. Λ can be calculated as

$$\Lambda = \frac{4m_1m_2}{(m_1 + m_2)^2} \tag{2}$$

where m_1 is the mass of a neutron, and m_2 is the atomic mass of the PKA. ΛE_n is the maximum energy that can be transferred from a neutron to the PKA atom in a collision (and occurs for $\cos(\theta) = -1$).

For elastic isotropic scattering in the center of mass system, the average energy, $\bar{T}$, transferred from a neutron of energy E_n to a nucleus of the target atom can be determined using

$$\bar{T} = \frac{1}{2}\Lambda E_n \tag{3}$$

If we know the kinetic energy of a neutron before and after a collision (E_n and E_n', respectively),the kinetic energy of the PKA, i.e., T, can be simply calculated using Eq 4, for an elastic collision:

$$T = E_n - E_n' \tag{4}$$

For inelastic scattering, the corresponding equation to find the energy of the PKA is more complex. Since in this article we restrict our attention to neutron energies below those for which inelastic scattering occurs for SiC, equations that describe energy transfer in inelastic scattering events are not reviewed here, but can be found in, e.g., Ref. [1].

Number of Displacements

As stated previously, the purpose of this article is to introduce a method to estimate the number of displacements. Displacement damage theories are based on the assumption that the target atom must receive a minimum amount of energy (E_d) in the collision in order to be removed from its original position. For PKA energies that are much larger than E_d, the number of displaced atoms that are produced by the PKA is proportional to the PKA energy. Based on the Nogrett-Robinson-Torrens (NRT) model and the Linhard method, the following equations can be used to approximate the number of defects that are produced per PKA ($\nu(T)$) [1,2,11]:

$$\nu(T) = \xi(T)\left(\frac{\kappa T}{2E_d}\right) \tag{5}$$

where κ is the damage efficiency and is equal to 0.8, independent of the PKA energy, and $\xi(T)$ accounts for the effects of inelastic energy loss by the PKA. $\xi(T)$ can be determined using

$$\xi(T) = \frac{1}{1 + k\ g(\varepsilon)} \tag{6}$$

where

$$k = \frac{0.13372\ Z^{2/3}}{A^{\frac{1}{2}}} \tag{7}$$

and

$$g(\varepsilon) = 3.48008\varepsilon^{1/6} + 0.40244\varepsilon^{3/4} + \varepsilon \tag{8}$$

where

$$\varepsilon = \frac{T}{86.931Z^{7/3}} \tag{9}$$

where the unit of ε is eV. In the above equations, Z and A are the atomic number and atomic mass of the target atom, respectively.

The DPA can be calculated as

$$DPA = \frac{\nu(T)n_{\mathrm{PKA}}}{VN_{\mathrm{SiC}}} \tag{10}$$

where n_{PKA} is the total number of PKAs in the simulation, V is the volume of the detector (the irradiated volume) in cm^3, and N_{SiC} is the atom density of SiC in cm^{-3}.

DPA Estimating Process

In this paper, we suggest to estimate displacements that are created by neutrons in SiC diode detectors by using the outputs of the MCNP and TRIM codes in series. In order to use TRIM to determine the number of displacements resulting from neutrons, TRIM requires as input the types, energies, initial positions and direction cosines of the PKAs. We receive these input parameters by modeling the transport of neutrons through SiC with MCNP.

In our case, we are concerned with displacement damage in Schottky SiC semiconductor diode detectors. These diodes are very thin ($\sim$300 μm). Consequently, the majority of neutrons, which are incident upon the surface of the SiC diode, pass through the SiC without interacting. The PTRAC card in MCNP5 was used to determine the probability that a neutron that enters the SiC volume will interact with a Si or C atom therein. Furthermore, a C-program was written to extract neutron characteristics (energy, position, and direction cosines), before and after each collision, as well as the type of the PKA that is created in a collision, from the PTRAC files that were created by MCNP5. Based on conservation of energy and momentum, the PKA characteristics (atomic species, energy, position, and direction cosines), were determined for elastic collisions.

The output of the C-program was used as an input for the TRIM code, which was used to estimate the number of displacements that are created, including the number of C- and Si-vacancies, and replacements. Based on SRIM/TRIM definitions, if both the energies of the projectile after collision and the target atom are more than E_d (the minimum energy that is required to move an atom from its original site), a vacancy will be created in the original position of the target atom. For the case where the projectile and the target atom are of the same atomic species (such as a Si projectile atom striking a Si target atom), and the post-collision energy of the projectile is less than, then there will be a replacement. In the worst case, the statistical error of this process, because of uncertainties in the sampling of MCNP and TRIM, was below 2 %.

The thickness of the semiconductor was assumed to be 310 μm (the active volume was assumed to have a thickness of 10 μm and the substrate was assumed to have a thickness of 300 μm). TRIM treats a solid as being amorphous. In other words, the target properties are assumed to be isotropic, including E_d. The directionally averaged values of E_d were set equal to 20 and 35 eV for C and Si, respectively, to be consistent with Weber et al. [12]. However, there is some uncertainty in these numbers, since—in addition to the isotropic approximation—supposedly more reliable ab initio simulations found that E_d might be

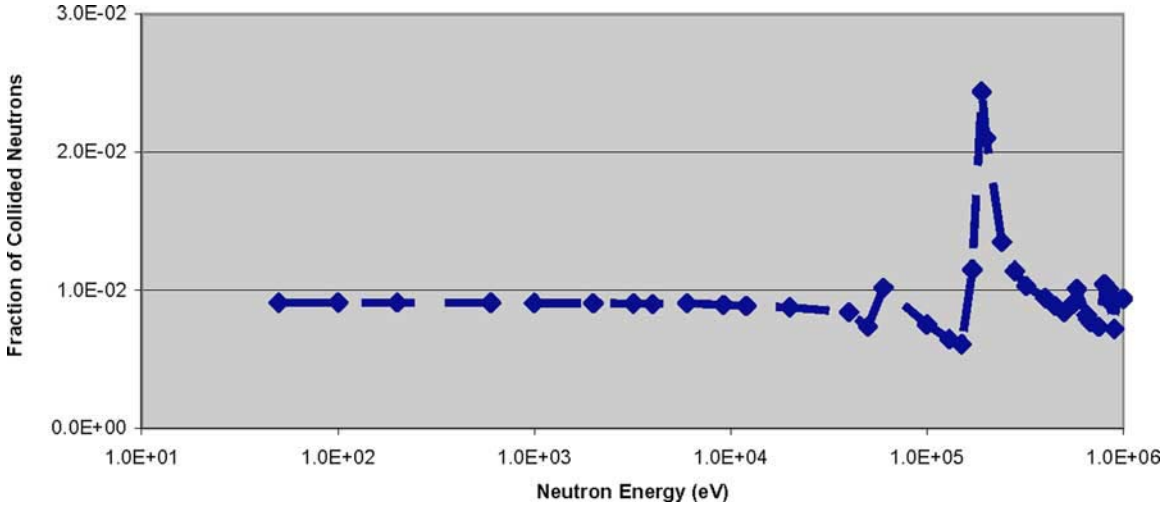

FIG. 1—*Fraction of neutrons that collide while passing through a* 310-μm-*thick* SiC *detector.*

higher for C, around 25 eV, and lower for Si, around 31 eV [13]. The experimental E_d values for Si in SiC vary between 35 and 85 eV, as a function of the Si orientation. For C, the experimental E_d values are 22 eVor smaller [14]. The SiC density was set to be 3.2 g/cm^3.

Results and Discussion

We used MCNP5 to determine the fraction of neutrons that collide while passing through the SiC detector. Figure 1 shows the fraction of neutrons that collide while passing through a 310-μm-thick SiC detector versus E_n, assuming the neutrons are isotropically directed.

Except at resonance energies, only a small fraction (about 0.6 %) of the neutrons that are incident upon the detector interact with Si or C atoms within the detector. Consequently, the probability that a particular neutron interacts two times within the SiC detector, before leaving the detector, is approximately 0.004 %. This probability (i.e., the probability that a particular neutron interacts twice within the SiC detector) is an important parameter in distinguishing between thin and thick SiC layers, since the thickness of the layer affects the dependence of the volume-averaged displacement damage on E_n. As an illustration of the effect, assume a neutron with energy E_n interacts within a SiC target that is thick enough that a neutron is likely to interact twice within the target. In this case, if a neutron scatters on a C atom, after the scattering event, the energy of the neutron decreases to $E'_{n,\mathrm{C}}$; if a different neutron with the same energy, E_n, interacts with a Si atom, the energy of the neutron decreases to $E'_{n,\mathrm{Si}}$. Since on average, $E'_{n,\mathrm{C}} < E'_{n,\mathrm{Si}}$, the dependence of the volume-averaged displacement damage on E_n would be less dramatic for a thick SiC target than for a thin SiC target; because, for the thick SiC target, the neutron that interacts first with a C atom, and in so doing deposits more energy in the SiC on average than a neutron which interacts first with a Si atom, would have less energy available on average to create additional displacements, if it were to interact a second time within the detector. Conversely, a neutron that interacts first with a Si atom, and in so doing deposits less energy in the SiC on average than a neutron which interacts first with a C atom, would have more energy available on average to create additional displacements, if it were to interact a second time within the detector. Therefore, as stated above, the dependence of the volume averaged displacement damage on E_n would be less dramatic for a thick SiC target than for a thin SiC target, because of the balancing of greater and lesser energy losses that occurs between the first and second collisions in a thick target. For our case, where the SiC target is very thin, the probability of interaction between neutrons and SiC atoms is very small, on a per neutron basis, and the dependence of the displacement damage on E_n is most pronounced.

The elastic scattering cross sections for Si and C are presented in Fig. 2 [15]. As can be seen, for E_n less than approximately 50 keV, the elastic scattering cross section of C is about 2 times greater than the elastic scattering cross section of Si. For E_n greater than 50 keV, the elastic scattering cross section for Si is comparable to, or slightly larger than, that of C.

Figure 3 presents the ratio of C-PKAs to the total number of PKAs (the ratio of the C scattering cross

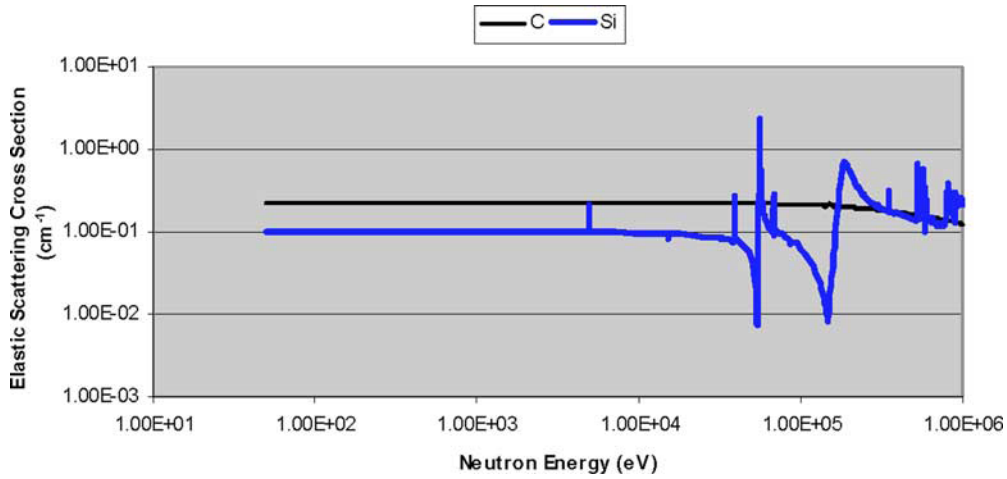

FIG. 2—*The elastic scattering cross sections for Si and C.*

section to the SiC scattering cross section) as a function of neutron energy. For low neutron energies, this fraction is 0.70. For larger neutron energies, this fraction varies due to variations in the scattering cross sections of C and Si.

Figure 4 shows the maximum and average C- and Si-PKA energies as a function of E_n. Theoretically, the ratio of the average PKA energy to the maximum PKA energy should be 0.5 for elastic and isotropic scattering. Our calculations show that this ratio is 0.50, for E_n less than 50 keV for C and for E_n less than

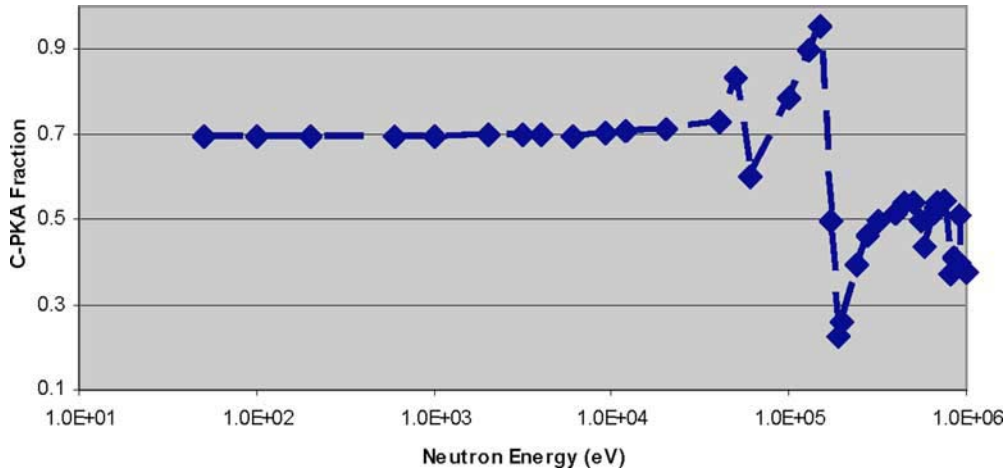

FIG. 3—*Fraction of C-PKAs as a function of neutron energy.*

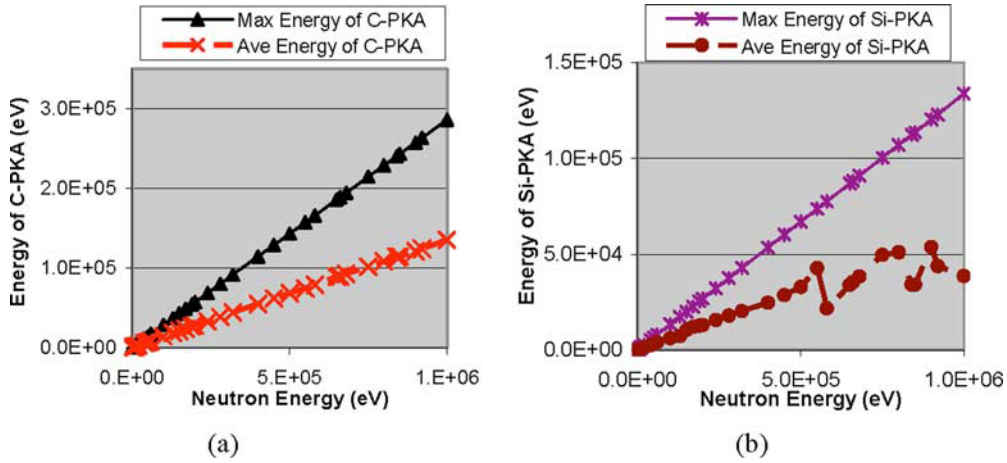

FIG. 4—*Maximum and average PKA energies versus neutron energy for (a) C-PKAs and (b) Si-PKAs.*

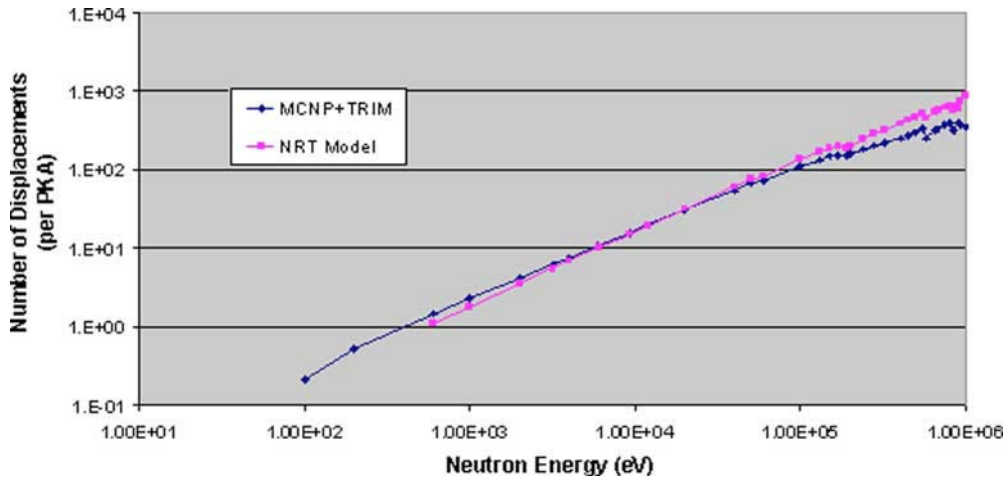

FIG. 5—*Number of displacements per PKA, determined by two methods: our method (MCNP+TRIM) and the NRT model.*

20 keV for Si. For greater than 50 keV for C, our calculations show that this ratio is slightly less than 0.5, because the scattering is not purely isotropic. For E_n ranging from 20 to 1 MeV for Si, our calculations show that this ratio varies between 0.29 and 0.58. Since the atomic mass of C is less than the atomic mass of Si, for equal E_n, the average C-PKA energy is greater than the average Si-PKA energy. Theoretically, the ratio of the average-C-PKA energy to the average-Si-PKA energy should be 2.13 for elastic and isotropic scattering. Our calculations reveal that the ratio of these two average energies is 2.14 for low E_n (where collisions are elastic and isotropic), but that due to anisotropic scattering, this ratio changes dramatically as E_n increases.

Figure 5 shows the number of displacements per PKA determined by our method as a function of E_n. For comparison, the number of displacements per PKA calculated by the simple NRT model is plotted as well. As it can be seen in the figure, these two results are in good agreement, particularly for small E_n. For larger E_n, the difference between the two methods is a little greater, since in the NRT model it is assumed that the neutron scattering angle is isotropic and that it is not a function of E_n. This assumption is not very accurate for large E_n, depending on the type of PKA. In addition, the NRT model was originally developed to estimate the number of displacements for elements, not compounds.

The results of our calculations of DPA/fluence from the previous results are presented as a function of E_n in Fig. 6, along with calculations of the DPA/fluence that we determined using SPECTER. One interesting point is that, according to both, the MCNP+TRIM calculations and the SPECTER calculations, the DPA/fluence is almost a constant, for E_n greater than 200 keV but less than 1 MeV.

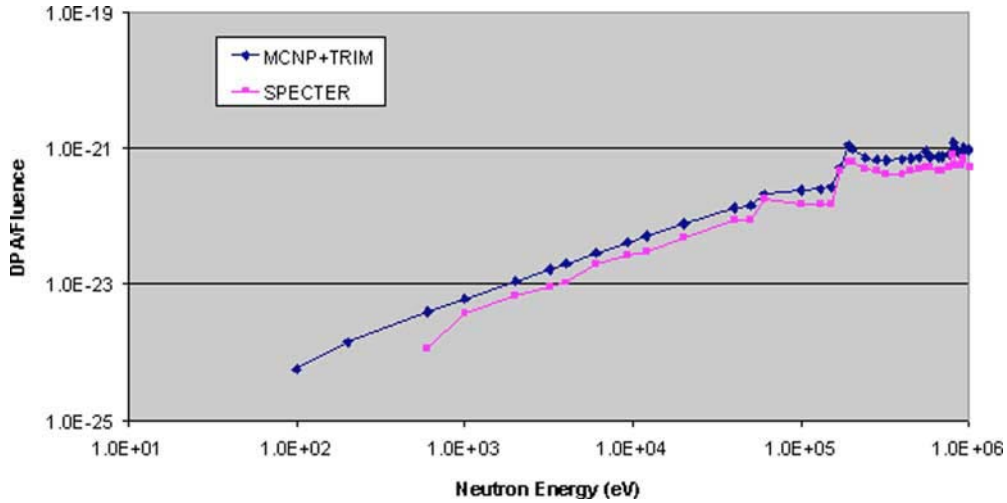

FIG. 6—*DPA/fluence as a function of neutron energy, determined by two methods: the MCNP+TRIM method as suggested in the present paper and SPECTER.*

As can be seen in Fig. 6, the results of the MCNP+TRIM and SPECTER calculations are comparable, except for low E_n. We believe that the main reason for the differences between the code calculations for low E_n is that the codes SPECTER and TRIM use different formalisms to predict the number of displaced atoms per PKA as a function of the kinetic energy of the PKA. The authors refer interested readers to the SPECTER and TRIM manuals [7,8] for details regarding the differences in the formalisms.

One advantage of using MCNP+TRIM is that MCNP+TRIM uses cross sections that are continuous functions of energy. Another advantage of using MCNP+TRIM, compared to SPECTER, is that MCNP+TRIM yields additional information; including, for example, the number of Si- and C-vacancies and replacements, the fraction of collided neutrons and the fraction of C-PKAs. Furthermore, when necessary, the spatial distribution of displacements can be studied. Finally, since TRIM is a code that was developed principally to study displacement damage resulting from ions, the MCNP+TRIM approach allows one to compare, in a consistent manner, the displacement damage caused by neutrons with the displacement damage caused by ions (for example protons to determine the effect of adding Coulomb interaction into the picture).

Conclusions

Our final goal is to be able to predict the operational lifetime of SiC detectors as neutron monitors, as a function of their flux and temperature histories. Towards this goal, we have developed a method to estimate the DPA/fluence using two well-known codes: MCNP and TRIM. From knowledge of the DPA/fluence, we are able to determine the DPA for any fluence. For the next step, we will calculate the resulting concentrations of C- and Si-antisites, vacancies, and interstitials. We will use these results combined with the results of ab initio modeling as input to kinetic diffusion equations that we will solve to study annealing of SiC defects as a function of time and temperature. Finally, we are modeling the influence of point defects on the electrical properties of SiC diodes to predict how these properties would change over time for various relevant time periods for reactor operation, such as a refueling cycle.

Acknowledgments

This material is based upon work supported by the US Department of Energy under the NERI program Award No. DE-FG-07-02SF22620 and NERI Project Number 02-207. Any opinions, findings, and conclusions or recommendations expressed in this material are those of the authors and do not necessarily reflect the views of the Department of Energy.

References

[1] Olander, D. E., "Radiation Damage," *Fundamental Aspect of Nuclear Reactor Fuel Elements*, Technical Information Center, Energy Research and Development Administration, USA, 1976.
[2] Gittus, J., *Irradiation Effects in Crystalline Solids*, Applied Science Publishers LTD, London, 1978.
[3] Norgett, M. J., Robinson, M. T., and Torrens, I. M., "A Proposed Method of Calculating Displacement Dose Rates," *Nucl. Eng. Des.*, Vol. 33, 1975, pp. 50–54.
[4] Coulter, C. A., and Parkin, D. M., "Damage Energy Functions in Polyatomic Materials," *J. Nucl. Mater.*, Vol. 88, 1980, pp. 249–260.
[5] Parkin, D. M., and Coulter, C. A., "Total and Net Displacement Functions for Polyatomic Materials," *J. Nucl. Mater.*, Vol. 101, 1981, pp. 261–276.
[6] Lee, M. B., and Farnum, E. H., "The Effect of Neutron Energy on Defect Production in Alumina," *Nucl. Instrum. Methods Phys. Res. B*, Vol. 102, 1995, pp. 113–118.
[7] Greenwood, L. R., and Smither, R. K., "SPECTER: Neutron Damage Calculations for Materials Irradiations," ANL/FPP/TM-197, Jan. 1985.
[8] Ziegler, F. J., "SRIM-2003," *Nucl. Instrum. Methods Phys. Res. B*, Vol. 219-220, 2004, pp. 1027–1036.
[9] Forster, R. A. et al., "MCNP Version 5," *Nucl. Instrum. Methods Phys. Res. B*, Vol. 213, 2004, pp. 82–86.

[10] Weber, W. J. et al., "The Efficiency of Damage Production in Silicon Carbide," *Nucl. Instrum. Methods Phys. Res. B*, Vol. 218, 2004, pp. 68–73.
[11] Fukahori, T. et al., *Reactor Dosimetry: Radiation Metrology and Assessment*, G. W. Williams et al., Ed., ASTM, International, West Conshohocken, PA, 2001.
[12] Gao, F., Weber, W. J., and Devanathan, R., "Defect Production, Multiple Ion-Solid Interactions and Amorphization in SiC," *Nucl. Instrum. Methods Phys. Res. B*, Vol. 191, 2002, pp. 487–496.
[13] Windl, W. et al., "First-Principle Investigation of Radiation Induced Defects in Si and SiC," *Nucl. Instrum. Methods Phys. Res. B*, Vol. 141, 1998, pp. 61–65.
[14] Zinkle, S. J., and Kinoshita, C., "Defect Production in Ceramics," *J. Nucl. Mater.*, Vol. 251, 1997, pp. 200–217.
[15] Korea Atomic Energy Evaluation Lab., 2000, http://atom.kaeri.re.kr/

MONTE CARLO MODELING OF COUNT RATES AND DEFECTS IN A SILICON CARBIDE DETECTOR NEUTRON MONITOR SYSTEM, HIGHLIGHTING GT-MHR

RADIATION MEASUREMENTS AND INSTRUMENTATION

KEYWORDS: *displacement damage modeling, silicon carbide, GT-MHR*

BEHROOZ KHORSANDI, MEHDI REISI FARD, THOMAS E. BLUE,*
and DON W. MILLER *The Ohio State University, Nuclear Engineering Program*
E429 Scott Laboratory, 201 W. 19th Avenue, Columbus, Ohio 43210

WOLFGANG WINDL *The Ohio State University*
Department of Materials Science and Engineering
477 Watts Hall, 2041 College Road, Columbus, Ohio 43210

Received July 12, 2006
Accepted for Publication November 5, 2006

Focusing on the gas turbine–modular helium reactor (GT-MHR), we have developed methods to predict the positions in a nuclear reactor where silicon carbide (SiC) semiconductor diode detectors may work functionally as neutron monitors for at least one refueling cycle. Using MCNP and TRIM, we determined the count rate due to fast neutron–induced primary knock-on atoms and tritons, and the number of displacement damage defects that are created per count and over a refueling cycle, for SiC diode detectors placed at four different radial locations in the central reflector of the GT-MHR. We found that although the total count rates for the SiC detectors placed in locations close to the fuel elements were highest (~1.2 × 10^6 counts/s), at those locations the detectors cannot tolerate the damage caused by fast neutrons for a reactor refueling cycle. On the contrary, for SiC detectors placed at the center of the central reflector, where the thermal neutron flux is the dominant flux component, the detectors can survive a GT-MHR refueling cycle. At this location, the total count rate for the SiC diode detectors that we have analyzed is ~1.6 × 10^5 counts/s.

I. INTRODUCTION

I.A. Motivation for SiC Detectors

There is considerable interest in developing neutron monitoring systems for Generation IV reactors that will increase reactor safety margins and possibly reactor efficiencies.[1] A new type of semiconductor neutron detector is under development based on the silicon carbide (SiC) technology for these reactors. As a semiconductor, 4H-SiC has some remarkable properties that make it a potentially appropriate material as a detector diode for high-temperature and high-neutron-fluence applications:

1. It has a high band gap.
2. In comparison to Si, it is radiation hard.
3. It is chemically and neutronically almost inactive.

Seshadri et al.[2] and Ruddy[3] showed that SiC detectors are still operational after irradiation with 3.4×10^{17} cm^{-2} fast neutron fluence or 1.1×10^{15} cm^{-2} triton fluence. In addition, a number of characteristics of SiC detectors make them well suited as neutron power monitors for terrestrial and space nuclear reactors. Among these characteristics are small size, small mass, small power consumption, and the potential for pulse-mode operation at high count rates.

In this paper, the focus is on the gas turbine–modular helium reactor (GT-MHR). The GT-MHR has been

*E-mail: blue.1@osu.edu

designed to work at high temperatures, with outlet He gas temperatures of ~850°C (Ref. 4), while in comparison commercial pressurized water reactors work at outlet coolant temperatures of ~300°C. Because of the high-temperature environment in the GT-MHR, SiC diode detectors may be well suited as neutron power monitors for the GT-MHR, if they can produce acceptably high count rates and withstand the GT-MHR radiation environment.

We used two Monte Carlo codes, Monte Carlo N-Particle[5] (MCNP) and Transport of Ions in Matter[6] (TRIM), to predict count rates and the number of defects created in SiC diode detectors, assuming that they are used as power monitors in specified locations in the GT-MHR. Although most of the defects that are created in the SiC detectors are annealed away for high-temperature operation, some fractions of the defects that are initially created are, or evolve to form, stable defects. This paper offers a systematic method for selecting the most appropriate locations to place SiC detectors in the GT-MHR, considering count rates and the defect formation rates. Effects of annealing are beyond the scope of this paper and are not considered in this analysis.

I.B. GT-MHR Design

The GT-MHR module arrangement is shown in Fig. 1. The primary components for each module are the reactor vessel and the power conversion vessel, which are connected by a cross vessel. The vessel systems are located inside an underground silo that is 23.9 m in diameter × 42.7 m deep, which serves as the containment structure. The reactor vessel is made of high-strength alloy steel and is ~7.58 m in diameter and ~31.2 m high (Ref. 7). It contains the reactor core, core supports, internal structure, reactivity control assemblies, and hot duct.

The reactor core consists of hexagonal fuel and reflector elements, plenum elements, and reactivity control material, all located inside a reactor pressure vessel. The core is designed to provide 600 MW(thermal) at a power

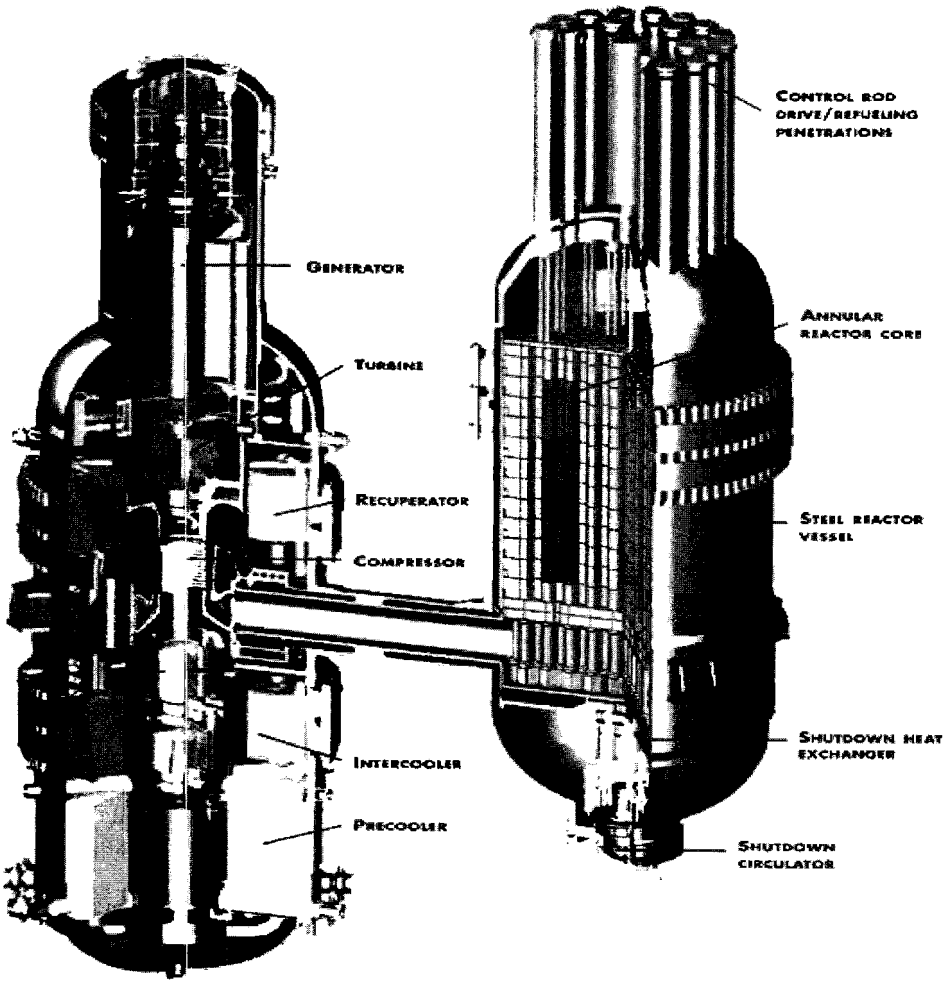

Fig. 1. GT-MHR module arrangements.

density of 6.6 MW/m^3. The active core consists of an assembly of hexagonal graphite fuel elements (blocks) containing blind holes for fuel compacts and full-length channels for helium coolant flow. The active fuel region of the core consists of 102 fuel columns, ten blocks high, arranged in three annular rings.

The core is cooled by helium, which flows through the outer annulus within the cross vessel, up the core inlet riser channels located between the core barrel and reactor vessel, and finally down through the core. The helium that is flowing into the reactor vessel is the working fluid in the power conversion system as well. The GT-MHR operates at elevated temperature with helium inlet temperatures of 491°C and outlet temperatures of 850°C (Ref. 4).

I.C. SiC Diode Design

Per the design of Westinghouse Electric Company,[8] the SiC neutron detector is based on a Schottky diode that detects tritons that are emitted from a LiF radiator layer comprising 90% enriched ^{6}Li. This LiF layer plays an essential role in the functioning of the SiC neutron detector since the tritons create a peak in the detector's pulse-height spectra, within the continuum of events that are the results of energy deposition by neutron-induced Si and C recoil nuclei.

Figure 2 presents the design of a Schottky diode neutron detector. As can be seen, the neutrons interact with ^{6}Li atoms producing ^{4}He (alpha) and 2.73-MeV ^{3}H (triton) particles. The tritons pass through an Al layer and deposit a fraction of their energy as ionization in the depleted region of the detector. Alpha particles, which also produce damage in the depleted SiC layer, are shielded by an aluminum layer. Computational analyses made using the TRIM code have shown that an 8-μm Al layer between the ^{6}LiF and SiC layers stops all alpha particles.

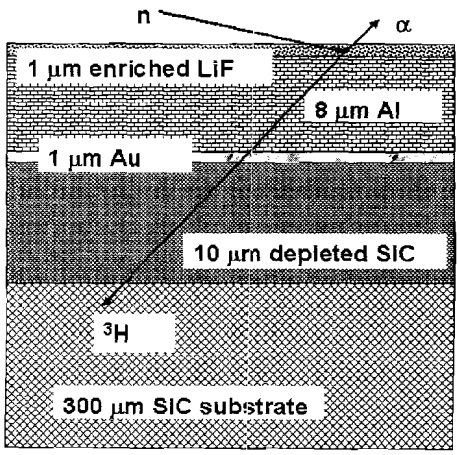

Fig. 2. Schottky diode concept. Picture is not drawn in scale.

Stopping alpha particles from producing radiation damage in the depleted region prolongs the detector lifetime.

In our analysis it is assumed that the detector is configured as shown from a lateral perspective in Fig. 2 and that the detector, when viewed from the top, is circular with a diameter of 500 μm.

II. SiC POSITIONING IN GT-MHR

II.A. In-Core Positions

This paper is directed toward the evaluation of semiconductor detectors for use as in-core neutron power monitors for the GT-MHR. For this purpose, a SiC diode detector has advantages because of its wide band-gap energy compared with conventional semiconductors, which make it resistant to the effects of temperature and radiation damage. Furthermore, its relatively small size permits measurement at discrete physical locations.

Although operation in the GT-MHR at 850°C might have some advantages for SiC detectors, by more completely annealing radiation damage, operation at such high temperatures would destroy the ohmic and Schottky contacts, for ohmic and Schottky contacts that are presently available for SiC devices. For this reason, we designed a cylindrical tube, which we shall hereafter call a "capsule," in which to place SiC detectors within the GT-MHR central reflector. The purpose of the capsule is to maintain the temperature of the SiC detectors at values that are below the limits for degradation of the ohmic and Schottky contacts but as high as possible within these limits so as to maximize the annealing of the detector. It should be noted that these capsules are not a part of the GT-MHR original design.

We chose four radial locations and, given the hexagonal shape of the GT-MHR, six azimuthally symmetrical azimuthal locations in the central reflector of the GT-MHR in which to place the capsules. Figure 3 (Ref. 9) presents a cross section of the reactor vessel in which the locations of the capsules are identified. The capsules are located at radii of 153 cm (R153) and 117 cm (R117), 81 cm (R81) and at the core center (R0).[a] There would, of course, be only one capsule located at the center of the central reflector since azimuthal angle cannot be defined for that position.

II.B. Capsule Design

The capsule design is only conceptual at this point. To keep the SiC within a temperature range of 400 to

[a] For the sake of simplicity, the notations R153, R117, R81, and R0 are used in the rest of this paper to refer to detector locations. The number after the R refers to the radial location of the capsule. For example, R153 refers to a capsule located at R = 153 cm from the center of the GT-MHR.

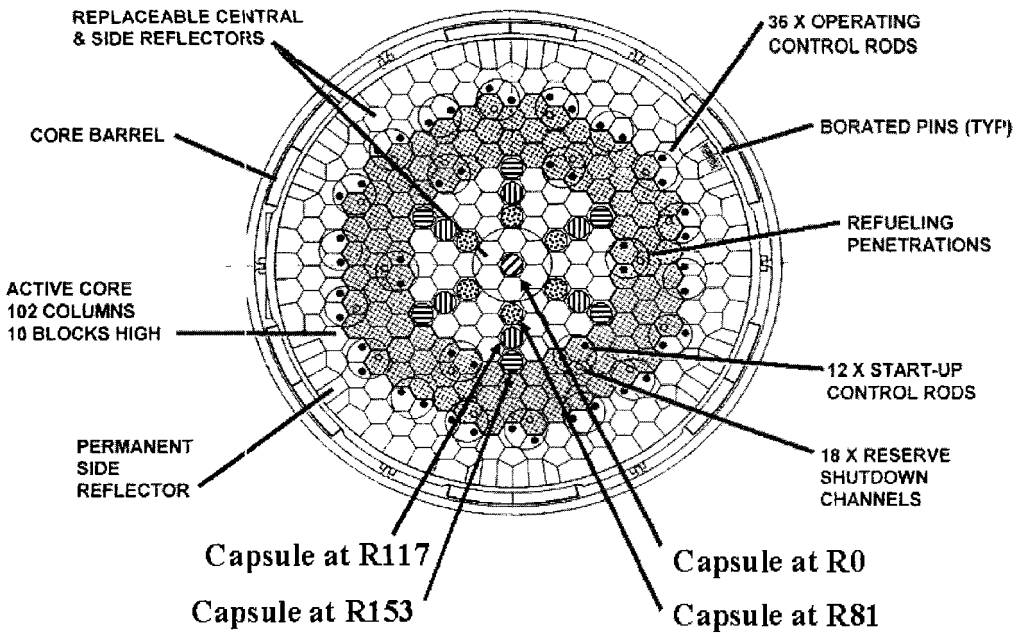

Fig. 3. GT-MHR core arrangement. R153, R117, R81, and R0 are shown in the schematic. The capsules are not in the original design and have been added by us.

600°C, it consists of two nested cooling systems (one that is passive and another that is active) circulating He coolant around and through, respectively, two nested steel cylinders that are insulated over their length by a third cylinder with larger radii (labeled "Insulator" in Fig. 4). The capsules enter the central reflector through the top of the core. The outer cooling system is a parasitic flow path (a diverted stream of reactor coolant) for the main coolant flow through the core. In Fig. 4, this flow path is through the tube with tube walls that are labeled "Insulator" and the inwardly adjacent tube. This parasitic flow path cools the detectors whenever coolant flows through the core. Although the term is not perfectly accurate, we will hereafter refer to it as a passive system. This system protects the detectors in the case of an accident event when the helium current for the other cooling system is disconnected. The other cooling system is a forced-convection (pumped) loop moving heat energy from the capsule's interior to the outside of the pressure vessel. Figure 4 shows the geometric arrangement of the two cooling systems.

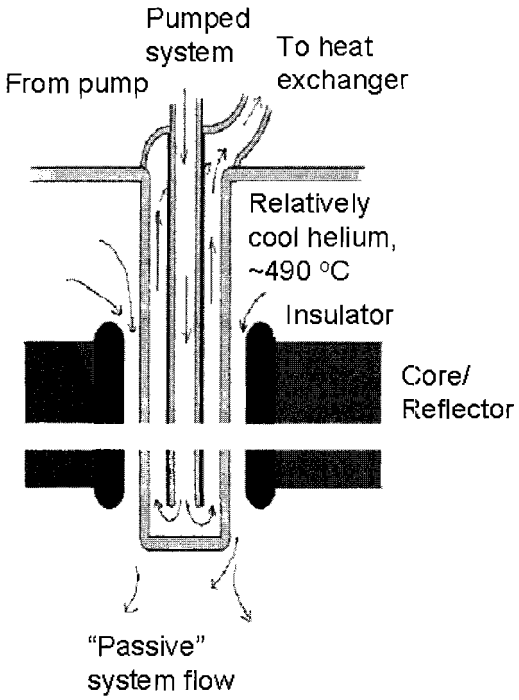

Fig. 4. Two nested cooling systems for the detector capsule. The detectors would lie in the central, downward-flowing coolant stream since this stream contains the lowest temperature flow. The picture is not shown to scale. The break in the drawing is intended to represent the axial extent of the core.

III. MCNP MODEL

The GT-MHR geometry was defined using MCNP input cards. Figure 5 presents axial and vertical cross sections for the MCNP-GT-MHR model. The three-dimensional geometry was made up of a series of vertical

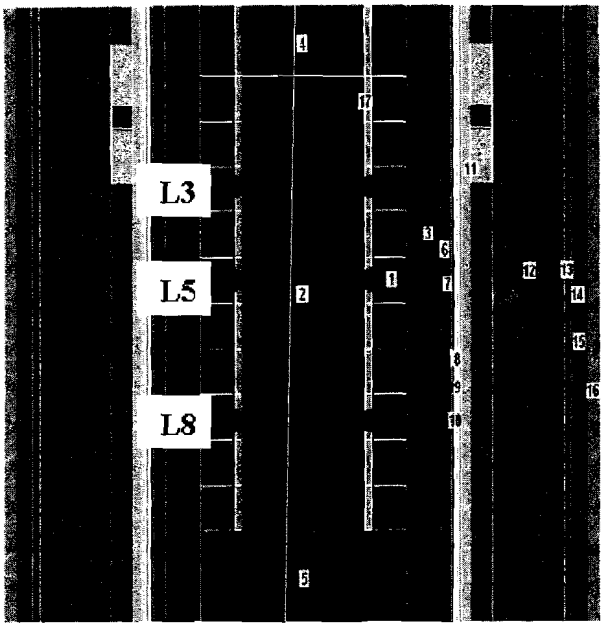

Legend:

1 - Core	5 - Lower Ref.	10 - Gas Duct Shell	14 - Air RCCS
2 - Inner Ref.	6 - Permanent Ref.	11 - Reactor Vessel	15 - Cavity Liner
3 - Outer Ref.	7 - Boron Pins	12 - Reactor Cavity	16 - Concrete
4 - Upper Ref.	8 - Core Barrel	13 - RCCS	17 - Capsule's Tube

Fig. 5. Cross section of the MCNP GT-MHR model.

surfaces and horizontal planes. Thus, all the regions of the reactor had finite lengths. Our model of the GT-MHR geometry is described in the following two paragraphs. In the first paragraph, we describe those parts of the MCNP model that are consistent with the General Atomics (GA) design of the GT-MHR, as that was the design provided to us by GA. The second paragraph describes those parts of the MCNP model that are particular to our envisioned modification of the GT-MHR design to include capsules in the central reflector in which to place SiC neutron monitors.

The parts of the MCNP model that are consistent with the GA design of the GT-MHR are described below, from smaller radii to larger radii. The central reflector consists of graphite hexagonal elements. These hexagonal elements are assembled in a manner so as to create a larger hexagon with a distance between flats (the distance between two opposite sides of the hexagon) of 280.592 cm. This larger hexagon defines the outer boundary of the central reflector and the inner boundary of the active (fueled region) of the GT-MHR core. The temperature of the outer hexagon in the central reflector was set to 753°C. The temperature of the other hexagons was 659°C. The active core consists of an assembly of hexagonal graphite fuel elements (blocks) containing blind holes for fuel compacts and full-length channels for helium coolant flow. The fueled region of the GT-MHR core ("1" in Fig. 5) was defined as existing between the hexagon that defines the outer boundary of the central reflector and a larger hexagon, with a distance between flats of 467.724 cm, which define the outer boundary of the active core. Neither the individual fuel compacts nor the coolant channels were modeled in detail. Also, six prismatic elements of the outer replaceable reflector were inserted into the hexagon defining the active core (compare the outside corners of the active core hexagon in Figs. 3 and 5), in order to model the real geometry as closely as possible. The volume of the active core was divided into ten axial layers according to the height of the hexagonal graphite fuel elements of which the core is composed. The height of the active core is 800 cm, and the height of one fuel element block is 80 cm. As can be seen in Fig. 5, above and below the core, there are upper and lower replaceable reflector cells. The height of the upper reflector is one and one-half blocks (120 cm), and the height of the lower reflector is two blocks (160 cm). Although they are formed as blocks, three regions of the core that are outside of the active core region were, for simplicity, modeled as annuli with increasingly larger radii. The three regions are, in order of increasing radii, the outer replaceable reflector, the permanent side reflector, and the portion of the permanent side reflector that contains boron carbide pins. The fueled region of the core was represented in the MCNP model as a homogeneous mixture of uranium, oxygen, silicon, boron, and carbon. The same modeling simplification of homogenization was used for the permanent side reflector that contains boron carbide pins. The thermal treatment option $[S(\alpha,\beta)]$ was invoked in MCNP for the graphite reflectors. The core barrel, the helium working fluid of the power conversion system that flows through two annuli that are within the core barrel, the air that fills the region between the outer surface of the reactor vessel and the reactor cavity cooling system (RCCS), the RCCS, and the concrete wall of the silo that contains the reactor were all modeled in more detail than is necessary for this calculation. This detail was a remnant of a previous modeling effort where the intent was to predict the response of detectors that were placed external to the reactor vessel. A more detailed description regarding our MCNP modeling of the GT-MHR can be found in Ref. 10.

The parts of the MCNP model that are particular to our envisioned modification of the GT-MHR design to include capsules in the central reflector in which to place SiC neutron monitors are described below. The capsules with the detectors and cables are envisioned to be placed at 0-, 60-, 120-, 180-, 240-, and 300-deg locations, within the central reflector, as shown in Fig. 5. Two annuli, with walls of steel, define each capsule. Each capsule is surrounded by a porous carbon annulus, which is identified as insulator in Fig. 4, that provides thermal insulation for the capsule. The volumes within the inner steel annulus, and between the steel annuli, and between the outer steel annuli and the surrounding porous carbon insulator are

filled with helium. Four models were created with capsules at R153, R117, R81, and R0.

IV. COUNT RATE CALCULATION

The neutron flux and detector count rates were calculated within the capsules for the ten axial layers corresponding to the ten fuel layers. Results of these calculations are labeled with an index, which corresponds to the fuel layer, with the numbering beginning with one at the top of the core and ending with ten at the core bottom.

Three general categories of events can contribute to the SiC detector count rate $[(CR)_{all}]$[b] in SiC detectors. The three categories of events are

1. events that are initiated by the interaction of gamma rays
2. events that are initiated by the interaction of thermal neutrons and epithermal neutrons with the radiator
3. events that are initiated by epithermal and fast neutron interactions with the SiC.

Events that are initiated by gamma rays produce counts in the detector in an indirect fashion, as the gamma rays generate secondary electrons. The thickness of the active volume of the detector, shown in Fig. 2, is so small (10 μm) that secondary electrons, which are created by gamma-ray interactions, pass through the diode active volume without creating many electron-hole pairs. Although gamma-ray events appear in recorded pulse-height spectra, the gamma-ray events can be eliminated from the pulse-height spectra by pulse-height discrimination, by setting a sufficiently large lower level of discrimination (LLD). The events that are initiated by thermal and epithermal neutrons are, in the great majority of cases, due to the interaction of the thermal neutron with ^{6}Li in the LiF radiator. The resulting tritons have a range that is large enough that for a 1-μm-thick LiF radiator, most of the tritons, which are emitted in the direction of the diode, enter the diode active volume and create a pulse that is above the LLD setting for gamma-ray discrimination. In contrast with the events that are due to tritons, events that are initiated by epithermal and fast neutron interactions with SiC create a pulse-height distribution that has components that are both above and below the LLD, if the LLD is set to barely eliminate gamma-ray events from the pulse-height spectra.

We have used MCNP to predict the count rates resulting from neutrons interacting with the LiF radiator and with the SiC. We have not concerned ourselves with modeling gamma-ray interactions, since events that are due to gamma-ray interactions can be eliminated from the detector count by pulse-height discrimination.

The detector count rate was calculated in a two-step process. As the first step of the process, we calculated the neutron flux within the capsules for the ten axial layers corresponding to the ten fuel layers. As the next step in the process, a model of the detector was created in MCNP, and the MCNP-SiC detector model was run to estimate $(CR)_{all}$. In the MCNP-SiC detector model, the SiC detector was modeled as being at the center of a sphere. A source of neutrons was defined at the surface of the sphere, with a neutron energy spectrum corresponding to the neutron flux that was calculated within the capsules, for R153, R117, R81, and R0 for three axial layers (3, 5, and 8). The neutron source was emitted from the spherical surface with a directional bias, which created a higher track density toward the center of the sphere, where our detector was placed. The radius of the sphere was 0.1 cm.

In order to calculate the fast neutron count rate $[(CR)_{neutron}]$, MCNP F4:N tally and PTRAC cards were used to determine the energy spectra for SiC PKAs.[c] Based upon experimental observations, we concluded that PKAs, which deposit >200 keV ($N_{E_{PKA>200\,keV}}$) within the detector active volume, create pulses that exceed the LLD and cause a count. Therefore, in our analysis, we counted the number of PKAs per source particles in the MCNP-SiC detector model that have energies >200 keV ($N_{E_{PKA>200\,keV}}$). Because the active volume of the SiC detectors is very thin, the probability of a single neutron creating more than one PKA is exceedingly small. Therefore, the pulse-height tally option in MCNP was not used.

Because a source particle for the calculation of the neutron flux using the MCNP-GT-MHR model is different from a source particle for the calculation of the detector count rate using the MCNP-SiC detector model, Eq. (1) was used to determine $(CR)_{neutron}$:

$$(CR)_{neutron} = \phi_{GT\text{-}MHR} \cdot N_{E_{PKA>200\,keV}} / \phi_{MCNP} \ , \qquad (1)$$

where $\phi_{GT\text{-}MHR}$ is the neutron flux at the desired location calculated using the MCNP-GT-MHR model and ϕ_{MCNP} is the neutron flux per source particle in the MCNP-SiC neutron detector model.

In addition, the MCNP FM card was used to determine the number of ^{6}Li$(n,\alpha)^3$He reactions in the LiF layer of a SiC diode detector. Then, the triton count rate $[(CR)_{triton}]$ was calculated using Eq. (2):

$$(CR)_{triton} = \phi_{GT\text{-}MHR} \cdot N_{triton} \cdot 0.39 / \phi_{MCNP} \ , \qquad (2)$$

[b]The subscript "*all*" stands for all projectiles related to the main variable. For instance, the count rate for the SiC diode detectors is due to either tritons or fast neutron–induced primary knock-on atoms (PKAs). Therefore, "*all*" in $(CR)_{all}$ refers to the tritons and fast neutron–induced PKAs.

[c]The methodology used to determine PKA specifications will be discussed in Sec. V.B.

where N_{triton} is the number of (n,triton) reactions per source particle in the MCNP-SiC detector model. The coefficient 0.39 accounts for 39% of the tritons that are born in the LiF reaching the SiC depleted layer (the geometric efficiency), for the SiC detector geometry shown in Fig. 2.

The value $(CR)_{all}$ is the sum of $(CR)_{neutron}$ and $(CR)_{triton}$. It should be noted that our calculation of $(CR)_{all}$ assumes that the SiC detector records perfectly all of the calculated interactions.

V. DISPLACEMENT DAMAGE IN SiC

V.A. SiC Displacement Damage Reactions

The properties of SiC diodes are changed by irradiation with energetic projectiles as a consequence of displacement damage. Energetic projectiles may hit and transfer energy to Si and/or C PKAs in a SiC semiconductor. Some PKAs may hit and transfer energy to other SiC atoms, and so on. If the transferred energy exceeds some specific value (E_d), then the struck atom is moved from its original site. As a result, displacement damage creates defects such as vacancies, interstitials, and antisites. A significant fraction of the defects that are initially formed anneal away as a consequence of interactions among the defects. However, a fraction of the defects may remain, so that with prolonged irradiation, the electronic characteristics of SiC diode detectors may change. These changes may alter the count rates of the detectors and hence may limit the lifetime of the detectors in a nuclear reactor. Accurately predicting the formation of the various types of defects in SiC diode detectors, as a consequence of neutron irradiation, is the first step in accurately predicting the effects of neutron irradiation on the detectors and in estimating the detector's lifetime in various reactor environments.

There are four origins for the projectile particles that initiate displacement damage cascades in the SiC diode detectors of the design that is shown in Fig. 2. They are

1. Si and C PKAs that are created by neutron scattering reactions
2. tritons that are emitted in the LiF layer with an initial energy of 2.73 MeV
3. 1.33-keV ^{29}Si recoils from ^{28}Si$(n,\gamma)^{29}$Si reactions
4. 1.01-keV ^{13}C recoils from ^{12}C$(n,\gamma)^{13}$C reactions.

The damage created in the SiC layers by these projectiles, except tritons, is uniformly distributed over the SiC volume since the detectors are thin and neutrons do not have a specific range in materials. On the contrary, the damage created by tritons is not uniform since tritons have a finite range in the SiC layers and are emitted in a geometry that consists of finite planes.

V.B. Displacement Damage Defects Modeling

Using the MCNP-SiC detector model and TRIM, we modeled the displacement damage defects that are induced in the SiC layers by the projectile particles that are identified in Sec. V.A. These diodes are very thin (310 μm SiC). Consequently, the majority of neutrons, which are incident upon the surface of the SiC diode, pass through the SiC layers without interacting. In order to use TRIM to determine the densities of defects resulting from neutron scattering, TRIM requires as input the types, initial positions, energies, and direction cosines of the PKAs that are created by neutron interactions. These input parameters for TRIM were determined by modeling the transport of neutrons through SiC in MCNP.

TRIM treats a solid as being amorphous. In other words, the target properties are assumed to be isotropic, including E_d (the minimum energy that is required to move an atom from its original site). The values of E_d were set equal to 20 and 35 eV for C and Si, respectively, to be consistent with Gao et al.[11] The SiC density was set to be 3.2 g/cm^3.

We used the PTRAC card in MCNP to determine the probability that a neutron, which enters the SiC volume, will interact with a Si or C atom therein in a scattering event. Furthermore, we wrote a C program to extract neutron characteristics (energy, position, and direction cosines) before and after each collision, as well as the type of PKA, from the PTRAC files that were created by MCNP. Then, using conservation of energy and momentum, the PKA energy and direction cosines were determined. A brief description of how we determined the stated PKA characteristics follows.

Suppose E_n and E_n' are the energies of a neutron before and after collision with a PKA (either Si or C), respectively. The PKA kinetic energy $E_{\rm PKA}$ was calculated using Eq. (3); this equation is valid for both elastic and inelastic scattering[d]:

$$E_{\rm PKA} = \frac{m_n}{M}\{E_n + E_n' - 2(E_n)^{1/2}(E_n')^{1/2}\hat{\Omega}_n\cdot\hat{\Omega}_n'\} \ , \quad (3)$$

where m_n and M are the masses of a neutron and the PKA nucleus, respectively, and $\hat{\Omega}_n\cdot\hat{\Omega}_n'$ is

$$\hat{\Omega}_n\cdot\hat{\Omega}_n' = \alpha_n\alpha_n' + \beta_n\beta_n' + \gamma_n\gamma_n' \ , \quad (4)$$

where

α_n, α_n' = direction cosines of the neutron before and after collision with respect to the x axis

β_n, β_n' = direction cosines of the neutron before and after collision with respect to the y axis

γ_n, γ_n' = direction cosines of the neutron before and after collision with respect to the z axis.

[d] Another equation to calculate the energy of a PKA is $E_{\rm PKA} = E_n - E_n' - Q$, where Q is the inelastic excitation energy if an inelastic collision happens. Otherwise, Q is zero.

The direction cosine of a PKA with respect to the x axis, α_{PKA}, can be calculated using Eq. (5):

$$\alpha_{PKA} = \frac{(E_n)^{1/2}\alpha_n - (E'_n)^{1/2}\alpha'_n}{\{E_n + E'_n - 2(E_n)^{1/2}(E'_n)^{1/2}\underline{\hat{\Omega}}_n\underline{\hat{\Omega}}'_n\}^{1/2}} \quad . \quad (5)$$

Similar equations can be used to calculate the direction cosines of PKAs with respect to the y and z axes.

The neutron characteristics, which were extracted from the MCNP-SiC detector model output using the C-extraction program, were used as an input for the TRIM code. The TRIM code was used to estimate the number of C and Si defects that were created as a consequence of irradiation with neutrons, based on the binary-collision approximation. Specifically, we calculated $(PDPA/\Phi_{MCNP})_{neutron}$, the number of point defects (hereafter, we call it defects) created per SiC atom per unit fluence by summing $(PDPA/\Phi_{MCNP})^i_{neutron}$ over species i (i = Si or i = C). The quantity $(PDPA/\Phi_{MCNP})^i_{neutron}$ was calculated for each species by dividing the number of defects that were created in the SiC diode by the number of atoms of either type in the diode and then dividing the resulting quotient by the MCNP fluence (Φ_{MCNP}) that created the defects; i.e.,

$$(PDPA/\Phi_{MCNP})_{neutron} = \sum_i (PDPA/\Phi_{MCNP})^i_{neutron} \quad , \quad (6)$$

where

$$(PDPA)^i_{neutron} = \frac{v^i_{neutron}(N_{PKA})^i_{neutron}}{Vn} \quad , \quad (7)$$

where

$v^i_{neutron}$ = average number of defects that are created in the SiC layers per PKA for a neutron scattering event with atoms of species i

$(N_{PKA})^i_{neutron}$ = total number of PKAs that are created by neutron scattering with atoms of species i

V = volume of the detector (the irradiated volume)

n = SiC atom density.

A similar methodology, with three differences, was used to calculate the number of defects created per atom of species i, in the SiC layers per unit fluence for the three other projectiles that initiate displacement damage (^{29}Si particles, ^{13}C particles, and tritons). The similarities in the methodologies are in the mathematical approach that was used, which is expressed in Eqs. (6) and (7), and that TRIM was used to determine the number of defects that were created per projectile particle. A difference was that in the implementation of the method, the 1.33-keV Si recoils and the 1.01-keV C recoils were explicitly assumed to be uniformly distributed in the SiC layers. Also, the 2.73-MeV tritons were explicitly assumed to be uniformly distributed in the LiF layer. A second difference was that instead of extracting neutron precollision and postcollision properties from the PTRAC cards and using these properties to deduce the properties of the PKAs, F4:N tally and FM cards in MCNP were used to determine the number of $^{28}Si(n,\gamma)^{29}Si$, $^{12}C(n,\gamma)^{13}C$, and $^{6}Li(n,\alpha)^{3}He$ reactions occurring per cubic centimeter per source particle in the MCNP-SiC detector model. The third difference was that instead of calculating $(N_{PKA})^i_{neutron}$, $N_{^{29}Si}$ (i.e., the number of ^{29}Si recoils that are produced by neutron absorption), $N_{^{13}C}$ (i.e., the number of ^{13}C recoils that are produced by neutron absorption), and N_{triton} (i.e., the number of tritons that are produced by neutron absorption) were used in Eq. (7). Therefore, v^i for these three recoil projectiles is defined as the average number of defects of species i that are created per projectile j (not PKA) in the SiC layers in the simulation, where j refers to a ^{29}Si recoil nucleus, a ^{13}C recoil nucleus, or a triton.

Finally, $(PDPA/\Phi_{MCNP})_{all}$ was calculated using Eq. (8):

$$(PDPA/\Phi_{MCNP})_{all} = (PDPA/\Phi_{MCNP})_{neutron} + \sum_j (PDPA/\Phi_{MCNP})_j \quad , \quad (8)$$

thus combining, in one term, the effects of epithermal and fast neutron–induced damage with the effects of damage that are initiated through the absorption of thermal and epithermal neutrons to produce ^{29}Si recoil nuclei, ^{13}C recoil nuclei, and tritons.

V.C. 1-MeV Equivalent Neutron Flux

As described previously, our goal was to find locations for the power monitors, considering detector count rates and lifetimes, such that the detectors could operate effectively for a period of time greater than at least one reactor refueling cycle. Regarding detector lifetime, our intent was to characterize the radiation environment in various locations in the GT-MHR, where detectors may be placed, in terms of the 1-MeV equivalent neutron flux in SiC ($\phi^{Total}_{eq,1MeV,SiC}$). The value $\phi^{Total}_{eq,1MeV,SiC}$ is defined as

$$\phi^{Total}_{eq,1MeV,mat} = \int_0^\infty \frac{F_{D,mat}(E)}{F_{D,1MeV,mat}} \phi(E)\, dE \quad , \quad (9)$$

where

$F_{D,mat}(E)$ = damage function for the material of interest (SiC) evaluated at energy E

$F_{D,1MeV,mat}$ = damage function for the material of interest (SiC) evaluated at energy E = 1 MeV

$\phi(E)$ = energy-dependent neutron flux density function.

Data for $F_{D,\mathrm{SiC}}(E)$ were extracted from, e.g., Ref. 12, assuming the average E_d for SiC is 22 eV (Ref. 13).

The other displacement damage parameter that we calculated was the neutron energy spectrum hardness (H_{mat}). As stated in the ASTM E 722 (Ref. 14), H_{mat} is defined as

$$H_{mat} = \phi^{Total}_{eq,1\mathrm{MeV},mat}/\phi^{Total} \quad . \qquad (10)$$

H_{mat} is a useful parameter with which to compare two or more neutron energy spectra on the basis of their propensity for creating displacement damage defects in a specific material (in our case SiC), assuming their total flux is equal.

VI. RESULTS

Figure 6 shows the differential neutron flux versus energy for locations R153L5, R117L5, R81L5, and R0L5[e] in the capsule. Although there is some lack of good statistics, particularly at R81L5, it is seen that the fast neutron flux declines dramatically by decreasing the radial location of the capsule in the GT-MHR central reflector. The thermal neutron flux at R117L5, R81L5, and R0L5 are comparable.

However, within the capsules, above ~10 eV, the neutron flux at R153L5 is greater than the neutron flux at other specified positions. On this basis, one can conclude that at R153L5, fast neutrons contribute more to the count rate and to the displacement damage rate than at R117L5, R81L5, and R0L5. However, the flux spectrum exhibits a thermal peak at these three locations, and consequently, the triton count rate $[(CR)_{triton}]$ at R117L5, R81L5, and R0L5 can be expected to be significant in comparison to the triton count rate at R153L5.

Figure 7 displays

$$E\phi_{eq,1\mathrm{MeV},\mathrm{SiC}}(E)Ln(10) \times \left(\phi_{eq,1\mathrm{MeV},mat}(E) = \frac{F_{D,mat}(E)}{F_{D,1\mathrm{MeV},mat}}\phi(E)\right)$$

as a function of neutron energy, on a log-linear graph. With this presentation format, the areas under the curves are meaningful. It can be seen from Fig. 7 that at R153L5, the displacement damage caused by fast neutrons greatly exceeds the displacement damage caused by thermal neutrons. By decreasing the radial location of the capsule, the importance of fast neutrons in creating damage decreases.

[e]This notation refers to the position in the GT-MHR where the calculation was made. As was stated previously, the number after the R refers to the radial location of the capsule in the GT-MHR. The number after the L refers to the axial position. For instance, R153L5 refers to a capsule located at R = 153 cm and to layer 5 (for 10 fuel layers where layer 1 is the top layer).

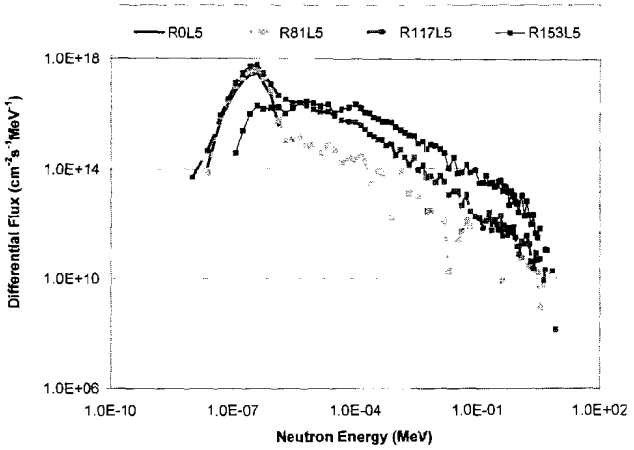

Fig. 6. Differential neutron flux versus energy for R153L5, R117L5, R81L5, and R0L5 [P = 600 MW(thermal)].

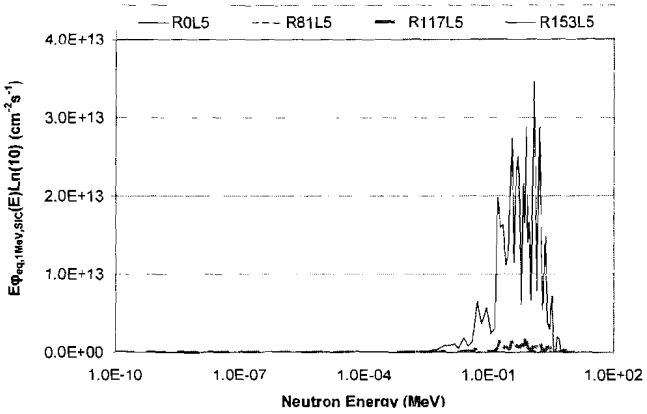

Fig. 7. The value $E\phi_{eq,1\mathrm{MeV},\mathrm{SiC}}(E)Ln(10)$ versus energy at R153, R117, R81, and R0. With this presentation format, the areas under the curves are meaningful.

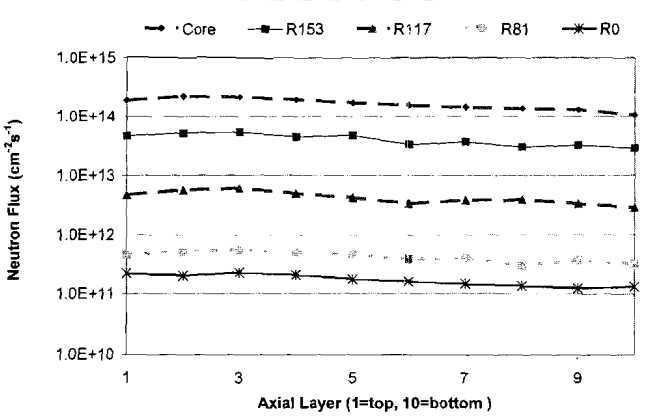

Fig. 8. Total neutron flux for various axial layers for the active core and for four radii: R153, R117, R81, and R0.

TABLE I

Average $\phi^{Total}_{eq,1MeV,SiC}$, H_{SiC}, $(CR)_{neutron}$, $(CR)_{triton}$, $(CR)_{neutron}/(CR)_{all}$, and $(CR)_{triton}/(CR)_{all}$ for R153, R117, R81, and R0 Within the GT-MHR

Detector Radial Location (cm)	$\phi^{Total}_{eq,1MeV,SiC}$ ($cm^{-2}\cdot s^{-1}$)	H_{SiC}	$(CR)_{neutron}$	$(CR)_{triton}$	$\frac{(CR)_{neutron}}{(CR)_{all}}$	$\frac{(CR)_{triton}}{(CR)_{all}}$
0	1.9E+08[a]	8.9E−04	0.0	1.6E+05	0.0	1.0
81	4.3E+10	1.0E−01	2.7E+03	2.2E+05	0.1E−01	9.9E−01
117	1.1E+12	2.1E−01	1.3E+04	5.8E+05	0.2E−01	9.8E−01
153	2.0E+13	4.5E−01	5.7E+05	6.4E+05	4.7E−01	5.3E−01

[a]Read as 1.9×10^{08}.

Figure 8 presents the total (integrated over all energies) neutron flux versus position for the ten layers of the GT-MHR core for the active core and at the specified axial locations within the capsule for capsules at R153, R117, R81, and R0. The total neutron flux within the active core is one and two orders of magnitude greater than the total neutron flux at R153 and R117, respectively. It can be seen from Fig. 7 that for the beginning-of-life source spectra used in the MCNP-GT-MHR model, the total neutron flux decreases nearly linearly with increasing layer number, for the active core and at locations R153, R117, R81, and R0. Therefore, for purposes of brevity, hereafter, results averaged over layers 3, 5, and 8 are presented as being representative of results for the GT-MHR as a whole.

Table I presents results regarding neutron fluxes and count rates averaged over axial layers 3, 5, and 8 with detector radial location as a parameter. Columns 2 and 3 present $\phi^{Total}_{eq,1MeV,SiC}$ and H_{SiC}. The value $\phi^{Total}_{eq,1MeV,SiC}$ for R153 is 2.0×10^{13} $cm^{-2}\cdot s^{-1}$. The values of $\phi^{Total}_{eq,1MeV,SiC}$ for R117, R81, and R0 are, respectively, one, three, and five orders of magnitude less than the value of $\phi^{Total}_{eq,1MeV,SiC}$ for R153. The decrease in $\phi^{Total}_{eq,1MeV,SiC}$ with decreasing detector radial location is due to the decrease of the total neutron flux with decreasing detector radial location that is shown in Fig. 8, plus the softening of the neutron flux energy spectra with decreasing detector radial location that is shown in column 3 of Table I. Columns 4, 5, 6, and 7 present $(CR)_{neutron}$, $(CR)_{triton}$, $(CR)_{neutron}/(CR)_{all}$, and $(CR)_{triton}/(CR)_{all}$. Regarding column 4, since thermal neutron absorption events in Si and C do not deposit within the Si and C enough energy for the energy depo-sition events to be recorded as counts, $(CR)_{neutron}$ decreases with decreasing detector radial location in approximately the same manner as $\phi^{Total}_{eq,1MeV,SiC}$. Regarding column 5, despite the softening of the neutron flux with decreasing detector radial location, $(CR)_{triton}$ decreases with decreasing detector radial location, due to the decrease in the total neutron flux (shown in Fig. 8). In column 6, $(CR)_{neutron}/(CR)_{all}$, like H_{SiC}, is a ratio. The variation of $(CR)_{neutron}/(CR)_{all}$ with detector radial location is similar but not identical to that for H_{SiC}. In column 7, on the other hand, $(CR)_{triton}/(CR)_{all}$ increases with decreasing detector radial location, as a consequence of softening of the neutron flux energy spectra since the sum of $(CR)_{neutron}/(CR)_{all}$ and $(CR)_{triton}/(CR)_{all}$ equals unity.

At R153, $(CR)_{neutron}$ and $(CR)_{triton}$ contribute almost equally to $(CR)_{all}$. On the contrary, $(CR)_{triton}$ contributes 98% to $(CR)_{all}$ at R117 and 100% to $(CR)_{all}$ at R0.

Table II presents values of υ [the average number of defects that are created in the SiC layers per projectile particle for ^{29}Si and ^{13}C recoil particles and tritons or per PKA for neutron scattering (neutron-PKA)]. Values of υ are presented for 1.33-keV ^{29}Si and 1.01-keV ^{13}C recoil particles and 2.73-MeV tritons, and for neutron-induced PKAs (for neutrons with energy spectra that are consistent with the stated location of the detector in the core). As is the case for Table I, Table II presents results averaged over axial layers 3, 5, and 8 with detector radial location

TABLE II

Values of υ for Various Projectile Species

Projectile	1.33-keV ^{29}Si	1.01-keV ^{13}C	2.73-MeV Triton	Neutron-PKA at R0	Neutron-PKA at R81	Neutron-PKA at R117	Neutron-PKA at R153
υ	134	28	52	0	60	116	252

TABLE III

$\left\langle \left(\frac{PDPA}{\Phi_{MCNP}} \right)_{all}^{whole} \right\rangle$, $\left\langle \left(\frac{PDPA}{\Phi_{MCNP}} \right)_{all}^{depleted} \right\rangle$, $\langle (PDPA)_{all}^{whole} \rangle$, and $\left\langle \frac{(CR)_{all}}{(PDPA)_{all}^{whole}} \right\rangle$
Values in Different Detector Radial Locations

Detector Radial Location (cm)	$\left\langle \left(\frac{PDPA}{\Phi_{MCNP}} \right)_{all}^{whole} \right\rangle$	$\left\langle \left(\frac{PDPA}{\Phi_{MCNP}} \right)_{all}^{depleted} \right\rangle$	$\langle (PDPA)_{all}^{whole} \rangle$	$\left\langle \frac{(CR)_{all}}{(PDPA)_{all}^{whole}} \right\rangle$
0	2.4E−23[a]	4.0E−22	1.7E−04	9.5E+08
81	2.2E−22	4.4E−22	3.8E−03	6.0E+07
117	4.0E−22	4.6E−22	8.0E−02	9.0E+06
153	8.8E−22	8.8E−22	1.5E+00	8.0E+05

[a]Read as 2.4×10^{-23}.

as a parameter, as indicated. Also, the value of v is calculated irrespective of where in the SiC diode the defects are created (either in the diode's active volume or in the substrate). For 1.33-keV ^{29}Si and 1.01-keV ^{13}C recoil particles and neutron PKAs, the value of v is independent of location in the diode, since the 1.33-keV ^{29}Si and 1.01-keV ^{13}C recoil particles and PKAs are born within the SiC. For the tritons, the number of defects that are created per triton is a function of location in the diode, since the tritons are born external to the diode. Regarding neutron-induced PKAs, on average, each neutron-induced PKA at R153 produces more damage in the SiC layers than the other projectiles because of the neutrons' high energies at this radial location. Regarding tritons, although the energy of tritons is 2.73 MeV at their birth in the LiF radiator, tritons create less damage than the other projectiles except ^{13}C, since in contrast to the other projectile particles, they are born external to the SiC, and therefore part of their energy is absorbed by the LiF, Al, and Au layers. Also, a large fraction of the triton's energy is spent in creating ionizations, not displacement damage.

Table III presents additional results that are averaged over axial layers 3, 5, and 8 with detector radial location as a parameter. However, the location of the defects within the SiC diode is noted (either averaged over the diode's active volume and substrate or in the diode's active volume only). This distinction is made because the doping levels of the diode's active volume and the substrate are different, and, therefore, the effect of a given concentration of defects on the performance of the diode may be different for these locations within the diode. Table III presents, respectively in columns 2 and 3, the values of $(PDPA/\Phi_{MCNP})_{all}$, averaged over the whole SiC volume ($\langle (PDPA/\Phi_{MCNP})_{all}^{whole} \rangle$) and averaged over the SiC depleted region (active volume) only ($\langle (PDPA/\Phi_{MCNP})_{all}^{depleted} \rangle$). From column 2 it can be seen that $\langle (PDPA/\Phi_{MCNP})_{all}^{whole} \rangle$ for R153 is twice as large as its corresponding value for R117 and is approximately 36 times larger than its corresponding value for R0. At R153, the capsule is very close to the fuel, and consequently, fast neutron interactions with Si and C atoms contribute significantly to the concentration of displacement damage defects in the SiC. On the contrary, at R117, R81, and R0, the concentration of displacement damage defects due to fast neutrons decreases dramatically with decreasing radial location, and the effect of tritons increases.

Because at R0 the thermal flux is large in comparison to the fast neutron flux, $\langle (PDPA/\Phi_{MCNP})_{all}^{depleted} \rangle$ is significantly more than $\langle (PDPA/\Phi_{MCNP})_{all}^{whole} \rangle$. This is because the damage caused by tritons is greater in the depleted region than in the substrate due to the limited range of the tritons in the SiC.

Table III presents in column 4 the axially averaged value of $(PDPA)_{all}$ averaged over the whole SiC volume for the detector radial location as a parameter, for the neutron fluence that would be experienced by the SiC detectors for the GT-MHR refueling cycle, i.e., 15.7 months ($\langle (PDPA)_{all}^{whole} \rangle$). For detectors located at R153, $\langle (PDPA)_{all}^{whole} \rangle$ is 1.5. This means that 75% of SiC atoms would be displaced[f] from their original sites in one refueling cycle. The corresponding percentage for detectors located at R117, R81, and R0 are 4.0, 0.19, and 8.5×10^{-3}%, respectively.[g]

Table III presents in column 5, the axially averaged $(CR)_{all}/(PDPA)_{all}$ averaged over the whole SiC volume for SiC detectors at R153, R117, R81, and R0, for the GT-MHR refueling cycle ($\langle (CR)_{all}/(PDPA)_{all}^{whole} \rangle$). This means that for a specified count rate, there would be many fewer defects for detectors located at R0 compared to detectors located at R153.

The cited results show that SiC detectors placed at R0 and R81 have more chance to survive at least one GT-MHR refueling cycle than SiC detectors at R153.

[f]Each displacement consists of approximately two defects.
[g]It should be mentioned that the impact of temperature on damage recovery has not yet been studied.

VII. SELECTION OF THE OPTIMUM DETECTOR LOCATION

Appropriate locations for the SiC detectors are locations where (a) the detector sensitivity is adequately large to monitor the reactor power with acceptable accuracy in acceptable times and (b) the detector survives for at least a refueling cycle period.

The power monitoring system sensitivity is an essentially important parameter in the design of the nuclear power plant power monitoring instrumentation. For a system that operates in pulse mode, such as the SiC detector system that is the subject of this discussion, the channel sensitivity is limited by the maximum allowable count rate of the channel. The electronic channel dead time is defined as the minimum amount of time that must separate two events in order that they are recorded as two separate pulses. The fraction of the counts that are lost due to dead-time effects can become unacceptably large when high counting rates are encountered, and the detector count rate should not exceed this value.[15] Our calculations show that a fast power monitoring system electronic channel, which we have designed and tested for SiC detectors based on the use of a voltage sensitive preamplifier, is able to process count rates as high as 5×10^7 counts/s with <10% count loss.[16] Assuming that a count loss that is as large as 10% can be corrected with acceptable accuracy, we somewhat arbitrarily specify here that the allowable count rate upper limit is 5×10^7 counts/s. As presented in Table IV, the detector count rates for R0, R81, R117, and R153 are far less than this allowable upper limit. Radiation damage to the detector channel does not affect the electronic processing speed of the channel and, therefore, the count rate upper limit. Rather, radiation damage diminishes the count rate of the channel by causing pulses that would otherwise be counted to fall below the discriminator threshold.[17]

As shown, four radial locations were identified in which to place the detectors. First, assuming arbitrarily a 1-s counting time, these detectors are only able to monitor reactor power for reactor powers in the power range at most, because of their limited sensitivity. Although modifications to the detector configuration can be made that will increase the channel sensitivity (the details of those modifications will not be discussed here), the sensitivity is nevertheless bounded on its high side. Consequently, depending on the detector counting time and count rate, there is a power level, for each potential detector location, for which the count rate is too low to obtain good statistics for the counting period. Even for their use in the power range, we cannot calculate with good confidence the acceptable operation of the power monitoring system since the system's required dynamic range at full power, response time, and accuracy are not known to us. These system specifications are interrelated in a way such that improving one specification may adversely affect another specification. As an example, if the power range is expanded to more than three orders of magnitude, the uncertainty of the channel count rate, at the lower limit of the range, can become unacceptably large, assuming a 1-s counting time and that the detector dead time does not exceed 10% at full power.

TABLE IV

The SiC Detector Sensitivity and $(CR)_{all}$* at Four GT-MHR In-Core Locations

	R0	R81	R117	R153
Sensitivity (count·s^{-1}/cm^{-2}·s^{-1})	9.2E−07[a]	5.3E−07	1.3E−07	2.8E−08
$(CR)_{all}$ (count/s)	1.6E+05	2.3E+05	6.2E+05	1.2E+06

*Averaged over axial layers 3, 5, and 8.
[a]Read as 9.2×10^{-7}.

VIII. CONCLUSION

Our final goal is to be able to predict the operational lifetime of SiC detectors, in different nuclear reactors, as neutron monitors, as a function of their flux and temperature histories. Toward this goal, highlighting the GT-MHR, we have developed a method to estimate the count rate and number of defects created per atom using two well-known codes: MCNP and TRIM. It was shown that for the stated SiC detector geometry, in comparison with detectors placed at R153, for detectors placed at R117, the count rate for the detectors is one-half, but the average $(PDPA)_{all}$ over a GT-MHR refueling cycle is 20 times smaller. For SiC detectors placed at R81 and R0, the reduction in the average $(PDPA)_{all}$ over a GT-MHR refueling cycle is much more significant. Based on available data in literature, SiC detectors placed in a capsule that is located at R0 and R81 can tolerate at least one GT-MHR refueling cycle.

In this paper, we did not study the impact of temperature on the SiC detector properties. The experimental results[18] and damage simulations by molecular dynamics[19] show a significant damage recovery at high temperatures. Currently, we are developing a kinetic Monte Carlo code to estimate the number of defects in SiC detectors while the detectors are operating at high temperatures in a nuclear reactor.

ACKNOWLEDGMENTS

This material is based upon work supported by the U.S. Department of Energy under the Nuclear Energy Research Initiative (NERI) program Award DE-FG-07-02SF22620 and NERI Project 02-207. Any opinions, findings, and conclusions or recommendations expressed in this material are those of the

authors and do not necessarily reflect the views of the U.S. Department of Energy.

We would like to thank F. Ruddy, J. Kulisek, B. Lohan, and A. Orosz for their assistance and informative support.

REFERENCES

1. T. E. BLUE et al., "Prediction of Radiation Damage in Silicon Carbide Semiconductor Radiation Detectors for Nuclear Reactor Power Monitoring in the GT-MHR," *J. ASTM Int.*, **3**, 8 (2006).

2. S. SESHADRI et al., "Demonstration of an SiC Neutron Detector for High-Radiation Environments," *IEEE Trans. Electron Devices*, **46**, 3 (1999).

3. F. H. RUDDY, "Silicon Carbide Semiconductor Radiation Detectors," presented at The Ohio State University; available on the Internet at www.min.uc.edu/nuclear/htmfile/osu_oct6.ppt (Oct. 2000).

4. M. P. LABAR, "The Gas Turbine–Modular Helium Reactor: A Promising Option for Near Term Deployment," GA-A23952, General Atomics (Apr. 2002).

5. R. A. FORSTER et al., "MCNP Version 5," *Nucl. Instrum. Methods Phys. Res. B*, **213**, 82 (2004).

6. F. J. ZIEGLER, "SRIM-2003," *Nucl. Instrum. Methods Phys. Res. B*, **1027**, 219 (2004).

7. "Gas Turbine-Modular Helium Reactor (GT-MHR) Conceptual Design Description Report," General Atomics (July 1996).

8. A. R. DULLOO et al., "The Neutron Response of Miniature Silicon Carbide Semiconductor Detectors," *Nucl. Instrum. Methods Phys. Res. A*, **422**, 47 (1999).

9. M. P. LABAR et al., "Status of the GT-MHR for Electricity Production," *Proc. 3rd Symp. World Nuclear Association*, London, United Kingdom, September 3–5, 2003, World Nuclear Association (2003).

10. B. LOHAN, "Nuclear Reactor Power Monitoring Using Silicon Carbide Semiconductor Radiation Detector in Gas Turbine Modular Helium Reactor," MS Thesis, The Ohio State University (2004).

11. F. GAO et al., "Defect Production, Multiple Ion-Solid Interactions and Amorphization in SiC," *Nucl. Instrum. Methods Phys. Res. B*, **191**, 487 (2002).

12. H. L. HEINISCH et al., "Displacement Damage in Silicon Carbide Irradiated in Fission Reactors," *J. Nucl. Mater.*, **327**, 175 (2004).

13. R. DEVANATHAN et al., "Atomic Scale Simulation of Defect Production in Irradiated 3C-SiC," *J. Appl. Phys.*, **90**, 5, 2303 (2001).

14. "Standard Practice for Characterizing Neutron Energy Fluence Spectra in Terms of an Equivalent Monoenergetic Neutron Fluence for Radiation-Hardness Testing of Electronics," ASTM E 722, Vol. 12.02, p. 318, ASTM International (1994).

15. G. F. KNOLL, *Radiation Detection and Measurement*, p. 119, John Wiley & Sons, New York (1999).

16. M. REISI FARD et al., "A Mathematical Model of SiC Detectors as Power Monitors," *Proc. 4th Int. Topl. Mtg. Nuclear Plant Instrumentation Control and Human-Machine Interface Technology*, Columbus, Ohio, September 19–22, 2004, American Nuclear Society (2004) (CD-ROM).

17. M. REISI FARD et al., "Evaluation of the SiC Semiconductor Diode Detector Degradation in a Fast Neutron Flux," *Proc. 5th Int. Topl. Mtg. Nuclear Plant Instrumentation, Controls, and Human-Machine Interface Technology*, Albuquerque, New Mexico, November 12–16, 2006, American Nuclear Society (2006) (CD-ROM).

18. W. J. WEBER et al., "Defect Annealing Kinetics in Irradiated 6H-SiC," *Nucl. Instrum. Methods Phys. Res. B*, **166–167**, 410 (2002).

19. F. GAO and W. J. WEBER, "Atomic-Scale Simulation of 50 keV Si Displacement Cascades in β-SiC," *Phys. Rev. B*, **63**, 054101 (2000).

NUCLEAR SCIENCE AND ENGINEERING: **157**, 316–330 (2007)

Development of a Novel Dynamic Simulink Model of the GT-MHR Core

Mehdi Reisi Fard, Thomas E. Blue,* and Don W. Miller

The Ohio State University, Nuclear Engineering Program, 201 West 19th Avenue Columbus, Ohio 43210-1142

Received October 6, 2006
Accepted February 3, 2007

Abstract—*A dynamic model of the Gas Turbine–Modular Helium Reactor core has been developed using the Simulink simulation program. The Simulink model utilizes a space-independent neutronics (point-kinetics) model along with a space-dependent heat transfer model of the core to simulate the short time reactor transients. The core model employs unique capabilities of the Simulink program to implement a user-friendly fully interactive environment to perform a variety of reactor transient scenarios.*

I. INTRODUCTION

An ongoing Nuclear Energy Research Initiative (NERI) project at The Ohio State University is directed toward the design, development, and assessment of a power monitoring system for two types of Generation IV reactors, namely, the Gas Turbine–Modular Helium Reactor (GT-MHR) and the International Reactor Innovative and Secure (IRIS). The power monitoring system is based on the use of silicon carbide (SiC) semiconductor diode detectors.[1–3] The SiC diode detector and the electronic processing channel have been studied, developed, and modeled.[4–6] Experiments are being conducted to evaluate the performance of the monitoring system and to assess the validity of the modeling. As an essential step in the development of the power monitoring system, we are investigating the power monitoring requirements for the GT-MHR. To evaluate the power monitoring requirements for the GT-MHR that are most demanding for a SiC diode power monitor, we have developed a Simulink model to study the transient behavior of the GT-MHR. In this paper, the Simulink dynamic model of the GT-MHR core is presented.

*E-mail: Blue.1@osu.edu

II. BACKGROUND

II.A. Rationale for Model Development

For the GT-MHR, rapid increases in the reactor power can potentially lead to fuel failure in two ways: (a) by exceeding the maximum allowable fuel temperature within individual microspheres and (b) by exceeding the maximum allowable rate of change of fuel temperature within individual microspheres. A number of reactor parameters are monitored during reactor operation to detect increases of reactor power in case of accidents and consequently to trip the reactor before fuel failure occurs. Safety trips of the GT-MHR are based on the neutron flux–to–He mass flow ratio, the primary coolant pressure, the core inlet and outlet temperatures, and the turbomachine speed.[7] Among the safety trip signals, the neutron flux–to–He mass flow ratio trip signal is relied upon to protect the reactor against fast up-power transients. Therefore, the neutron flux measurement and the response time associated with the neutron flux measurement are especially important.

Because of the significance of the neutron monitoring instrumentation response time, the adequacy of a SiC neutron power monitoring channel to respond to fast up-power transients should be examined. Furthermore, as a consequence of the proportional relationship

between count rate and power, identifying the largest acceptable response time of the power monitoring channel, which can provide protection of the reactor for the most rapidly increasing credible reactor power transient, is a major step in specifying the dynamic range of the power monitoring system. Therefore, accident scenarios that can cause reactor power to increase rapidly have to be studied. Accident scenarios such as accidental withdrawal of control rods, loss of poison material from the core, insertion of reactive material into the core, changes in geometrical core configuration, loss of coolant and blower failure, and start-up accidents have been qualitatively studied[8,9] for high-temperature reactors (HTRs). Among those accidents, the start-up reactivity insertion transient (SURIT), which is an accident within the category "accidental withdrawal of control rods," where the transient is initiated with the reactor initially operating below the power range, is considered the most limiting protectable accident (an accident where the concern is damage to the reactor plant) in terms of establishing the dynamic range of the SiC power monitoring system.[10]

Analysis of the reactivity insertion accident (RIA) is a main category of the design-basis accident analyses.[11,12] In the analysis of the accidents occurring during power operation, such as the RIA, it is important to find the worst conditions under which the accident can occur.[11] The maximum temperatures reached during an accident, and the rate of power increase, vary considerably according to initial power. Therefore, we developed a computational tool with which to study control rod withdrawal accidents that are initiated from various power levels, such as the two power level extremes (full power and start-up power).

II.B. Work of Others and Scope of Our Model

In order to study and model GT-MHR RIA transients such as the SURIT and the full-power reactivity insertion transient (FPRIT), two dynamic reactor models have been developed. One is based on the RELAP5 program,[a] and the other is based on the Simulink program.[b] The RELAP5 model of the GT-MHR was developed previously by General Atomics.[13] We have recently developed the Simulink model, which is the subject of this paper.

The Simulink program is widely used in a variety of fields because of its superior capabilities in modeling and analyzing dynamic systems. Recently, the Simulink program has been used by others to model the dynamics of nuclear reactors.[14–16] In general, reactor dynamics simulations are concerned with the analysis of the time-dependent behavior of the reactor in normal operation and during accidents.[8] Numerous reactor dynamics simulation codes have been developed to study various aspects of reactor dynamics for different types of nuclear power plants. Depending on the application of the simulation, computer codes are focused on different parts of the reactor, such as the reactor core and the power conversion system. Since our Simulink model of the GT-MHR was written to evaluate the response of detectors to fast reactor transients, we have included in our model a detailed model of the GT-MHR reactor core that includes the main short time constant phenomena. On the other hand, we did not include the power conversion system, which introduces long-term transients, in our model.

Similarly, the GT-MHR reactor core model does not account for fuel burnup and fission product decay. Xenon and samarium transients have time constants that vary between 9 and 48 h. The time constants for burnup transients are even longer. For the transients that are of concern to us in our analysis of response time requirements for SiC diode power monitors, i.e., transients with fast time dynamics (transients with time constants that vary from fractions of seconds to a few minutes), the change in the number of Xe and Sm and fuel atoms within the core is negligible.

III. MODEL AND PAPER OVERVIEW

The Simulink GT-MHR model consists of the core model and a subsystem that has been created to model the control instrumentation. The core model consists of two major subsystems: a neutronics subsystem and a thermohydraulics subsystem. The GT-MHR model offers a number of new features in terms of modeling methods and interfacing schemes in the simulation of the reactor core and control systems. The control instrumentation modeling scheme provides a fully interactive environment, which can be upgraded to a control room simulator. The flexibility of the control instrumentation modeling scheme lets the user simulate numerous accident scenarios, as well as normal operational transients. Modifications and improvements to the model can be easily performed because of the block-oriented nature of the model. Although the existing model is specifically focused on modeling the GT-MHR, the model can be easily applied to any gas-cooled reactor or reactors with a single-phase coolant on the primary side.

The core neutronics subsystem accounts for the main phenomena that occur during fast reactor transients. Each of these phenomena is characterized by a different time constant. The results of control rod withdrawal accidents are usually rapid transients whose time constants are determined by the lifetime of the prompt and the delayed neutrons and the reactivity insertion. Fuel and moderator temperature feedbacks have time constants determined by the heat capacity and conductivity of fuel and moderator. The function of the neutronics subsystem is discussed in more detail in Appendix A.

[a]See http://www.inl.gov/relap5.

[b]From The MathWorks, Inc., 3 Apple Hill Drive, Natick, MA 01760.

In addition to the core neutronics model, the Simulink model includes a detailed model of the reactor core thermohydraulics, along with an efficient and user-friendly controlling system. The thermohydraulics model calculates the temperature distribution throughout the core, instead of attributing a single temperature to the whole-core structure. Such a detailed core thermohydraulics model is important for accurate modeling for two reasons. First, knowing the temperature distribution within the core is crucially important when core temperatures are compared with core component temperature limits. Second, the temperature reactivity feedback due to the fuel and moderator are calculated separately and more accurately.

Our intent in developing the Simulink model was to initially reproduce the RELAP5 model of the GT-MHR and the RELAP5 results (developed by General Atomics) as a means of validating the Simulink code. Our thoughts were that once the RELAP5 results were reproduced, then the Simulink model could be modified from this validated base state in order to identify the effect of various changes to this base model.

Although the existing Simulink model does not include the balance of plant, the core and control room models accurately simulate transients in which the characteristics of the secondary side do not change significantly during the simulation. The core and control room models are described in this paper, and results of a representative simulation are presented and compared with the results of RELAP5 for purposes of validation.

In Sec. IV, FPRIT simulation results obtained by RELAP5 and Simulink are presented and compared. A parametric evaluation of the effects of the initial power level on the severity of a SURIT is left as a topic for a following paper. In Appendixes A, B, and C, the core neutronics model, the core thermohydraulics model, and the model of the control instrumentation, respectively, are discussed. Each section includes a description of the methods that are used to model each subsystem.

IV. FULL-POWER REACTIVITY INSERTION TRANSIENT ANALYSIS

In this section, the reactor characteristics at full power as calculated by the Simulink model are presented and compared to RELAP5 simulation results obtained by General Atomics. In Sec. IV.A, the reactor characteristics at full power in steady state are studied. The FPRIT is investigated in Sec. IV.B. Finally, differences between the Simulink and RELAP5 results are discussed.

IV.A. Steady-State Full Power

At middle of equilibrium cycle (MOEC) full power, reactor criticality is achieved by having four rod banks fully inserted and the fifth rod bank inserted by 60.8%.

TABLE I

Coolant Specifications at Full Power

Helium mass flow rate (kg/s)	322.703
Helium pressure (MPa)	7.03
Helium inlet temperature (K)	909.6

The coolant specifications at full power are also presented in Table I. These specifications are used as the Simulink model inputs to calculate the temperature distribution in the coolant-hole model.

Using the parameters shown in Table I, the temperature of the reactor core is calculated at steady state. Table II shows the temperature distribution at the coolant-hole mesh points (defined in Appendix B), which is obtained at full power using Simulink. The temperature differences between the RELAP5 and Simulink model results are shown in Table III. They are very small. The maximum difference is <0.7% and occurs at the outermost mesh point of the second row.

Figure 1 shows temperature distribution at full power throughout the coolant-hole structure. The mesh points defined in Appendix B are shown in Fig. 1 so that the reader can visualize the temperatures in the fuel, moderator, reflectors, and He channel regions.

The average temperature of the fuel, moderator, and reflector calculated by RELAP5 and Simulink and the differences between the calculated temperatures for the two codes are presented in Table IV. The greatest difference is in the average fuel temperature, which is ~0.11%.

The accuracy of the calculations of the average fuel and moderator temperatures is crucial since the average fuel and moderator temperatures are used as the basis for

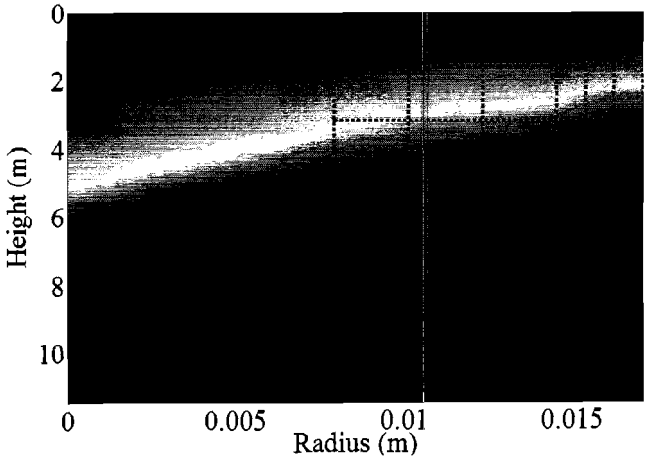

Fig. 1. Temperature distribution in the coolant-hole model at full power (two-dimensional).

TABLE II

Steady-State Temperature Distribution in the Coolant Hole at Full Power Using Simulink Model*

760.70	760.70	760.70	760.70	760.70	760.70	760.70	760.70
875.27	962.71	977.64	989.57	999.48	1013.48	1022.52	1026.90
1027.80	1102.03	1114.35	1124.21	1132.41	1144.11	1151.66	1155.33
1118.82	1144.77	1149.10	1152.57	1155.47	1159.62	1162.31	1163.61
1118.89	1118.93	1118.93	1118.94	1118.94	1118.94	1118.94	1118.94

*In units of Kelvin.

TABLE III

Temperature Difference between RELAP5 and Simulink Models*

−0.01	−0.02	−0.02	−0.02	−0.02	−0.02	−0.02	−0.02
−0.02	−0.12	−0.11	−0.08	−0.05	−2.28	−4.48	−6.63
0.08	1.01	1.02	1.00	1.02	−0.85	−2.68	−4.45
0.37	0.88	0.88	0.86	0.85	0.20	−0.43	−1.07
−0.17	−0.22	−0.23	−0.23	−0.24	−0.24	−0.24	−0.24

*In units of Kelvin.

TABLE IV

Average Temperature of Fuel, Moderator, and Reflector Calculated by RELAP5 and Simulink

	RELAP5 (K)	Simulink (K)	Difference (%)
Average fuel temperature	1126.41	1127.68	0.113
Average moderator temperature	1109.09	1108.37	0.065
Average reflector temperature	952.97	953.10	0.014

TABLE V

Reactivity of Fuel, Moderator, and Reflector at Full Power

	RELAP5 ($)	Simulink ($)
Fuel reactivity	6.194	6.186
Moderator reactivity	−0.1727	−0.1716
Reflector reactivity	0.0463	0.0467

calculating the reactivity. Table V presents the reactivity of the fuel, moderator, and reflector at full power as calculated by RELAP5 and Simulink. As expected, based on the differences between the calculated temperatures for the two codes, the reactivities calculated by RELAP5 and Simulink are in good agreement. They exhibit roughly the same fractional errors as the fractional errors in the corresponding material temperatures.

IV.B. Full-Power Transient Analysis

The FPRIT is simulated by withdrawing a fully inserted rod group when the reactor is critical at full power. A rod bank with the highest reactivity worth is chosen to be withdrawn. The rod bank is withdrawn with the speed of 3 cm/s, which is the maximum allowable withdrawal speed. Withdrawing the rod bank makes the reactor supercritical, and consequently, the reactor power will increase. The reactor scrams when the power-to-coolant flow ratio is 1.5, i.e., when reactor power increases to 150% of full power. When the reactor scrams, all rod banks are inserted. For a fully withdrawn rod bank, it takes 23.13 s to be inserted completely.

IV.B.1. Variation of Reactor Power

To study the FPRIT, at t = 600 s the chosen rod bank is withdrawn. The reactor power increases to 150% (900 MW) of full power at t = 642.6 s using the Simulink model and at t = 642.9 s using the RELAP5

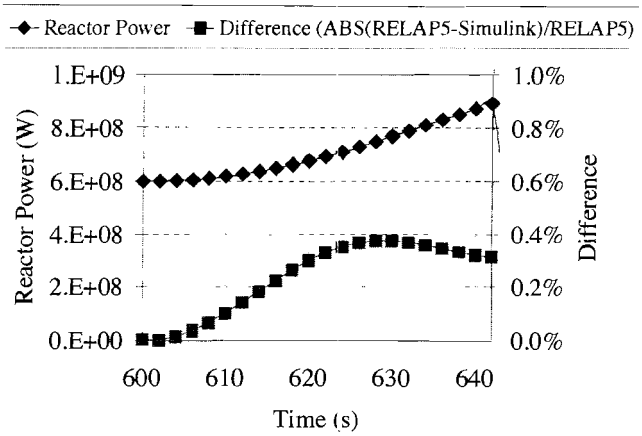

Fig. 2. Variation of the reactor power during FPRIT using the Simulink and RELAP5 models.

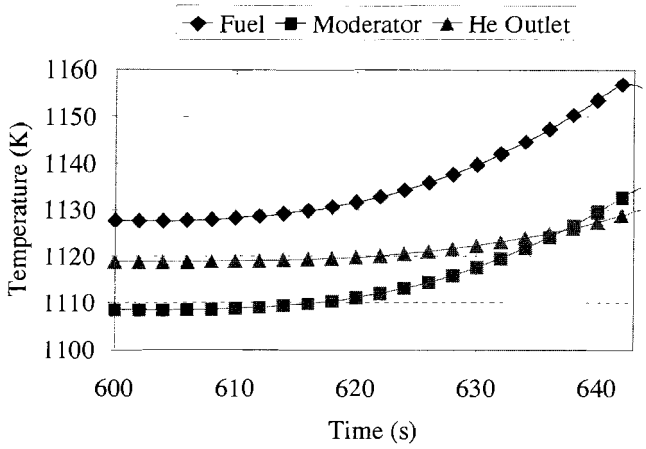

Fig. 3. Variation of the average fuel, average moderator, and He outlet temperatures during an FPRIT using the Simulink model.

model. Figure 2 shows the power trace during the FPRIT using the Simulink model. In addition, Fig. 2 presents the relative difference between the Simulink and RELAP5 results. The Simulink and RELAP5 codes calculate power during the FPRIT with <0.4% relative difference.

IV.B.2. Variation of Reactor Temperature

Evaluation of the reactor temperatures during the FPRIT is crucial from two standpoints. First, the reactivity feedback associated with the average fuel and moderator temperatures greatly affects the total reactivity of the core and consequently the reactor power. Second, the local temperature of the fuel during the transient is crucially important since the fuel temperature should not exceed certain limits. In this section, we discuss the variation of average fuel and moderator temperatures, as well as the coolant outlet temperature. Furthermore, the variation of local fuel temperature is discussed.

Figure 3 presents the average fuel, moderator, and He outlet temperatures. As shown, the average fuel temperature increases by ~30 deg during the transient. Figure 4 presents the difference between the average fuel, moderator, and He outlet temperatures calculated by the RELAP5 and the Simulink models. As shown, during the transient, the differences in the average fuel, average moderator, and He outlet temperatures are <0.15, 0.08, and 0.08%, respectively.

With the Simulink model we are able to calculate the fuel temperature locally. Figure 5 shows the variation of the core temperature at the third axial divisions of the coolant hole. The seven curves in Fig. 5 represent the temperatures at the seven radial meshes of the corresponding axial division. The maximum fuel temperature during the transient is 1200.57 K and occurs at $t = 642.89$ s (42.89 s after the beginning of transient). Since the

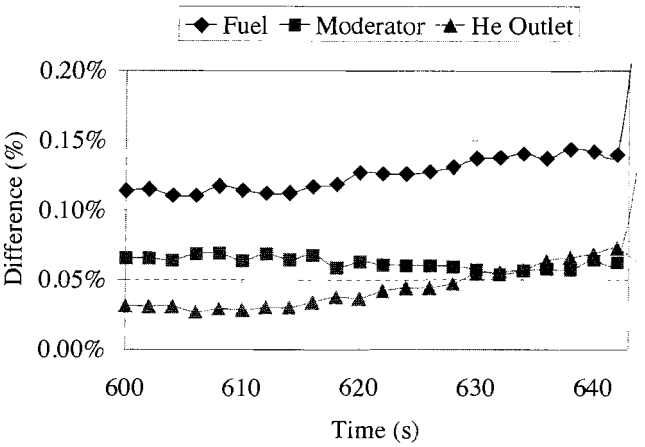

Fig. 4. Differences between average fuel, average moderator, and He outlet temperatures calculated by the Simulink model and calculated by the RELAP5 model during an FPRIT.

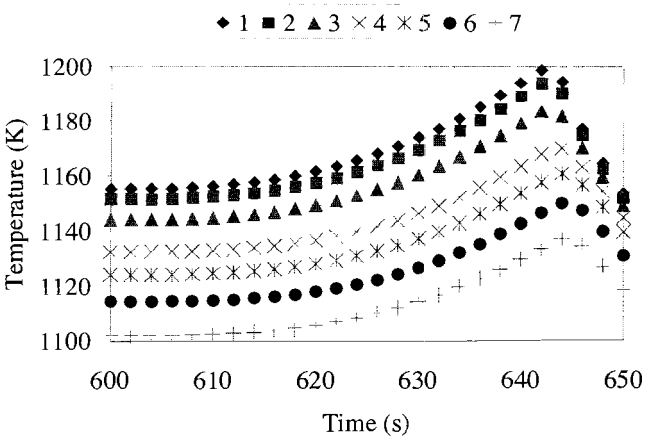

Fig. 5. Temperature variation on each mesh of the coolant-hole third row using Simulink model.

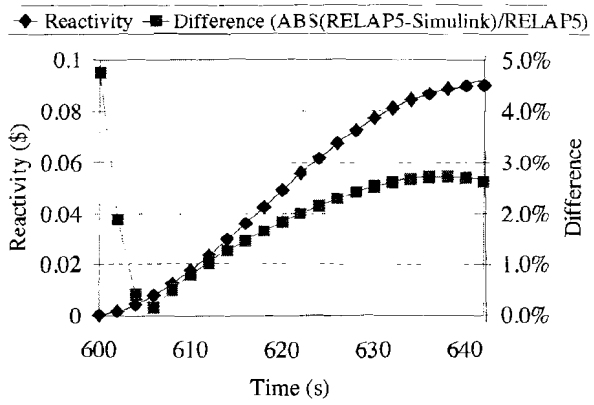

Fig. 6. Variation of the reactor reactivity during transient using Simulink and RELAP5 models.

limitation on the fuel temperature is ~1600 K, even the temperature at the hottest spot is considerably lower than the maximum allowable temperature.

IV.B.3. Variation of Reactor Reactivity

Figure 6 shows the variation of the core reactivity during the transient. During the first few seconds, when the core temperature does not change considerably, the reactivity change is mainly due to withdrawing the rod bank, which increases the reactivity. According to Fig. 3, the average fuel temperature begins to change after a few seconds, which decreases the reactivity associated with the fuel. Although increases in the moderator and reflector temperatures also change the core reactivity, the change in the fuel temperature has the greatest impact (Fig. 7). Therefore, after the first few seconds of the transient, the core reactivity depends on not only the positive reactivity insertion due to rod bank withdrawal but also the negative reactivity insertion due to fuel temperature increase. As a result, the rate at which the core reactivity grows begins to decrease.

An interesting observation is obtained when we decrease the fuel heat capacity. By decreasing the fuel heat capacity, the fuel temperature rises faster, and the fuel reactivity decreases faster. Thus, the total core reactivity begins to decrease even before reactor power reaches 150% of the full power.

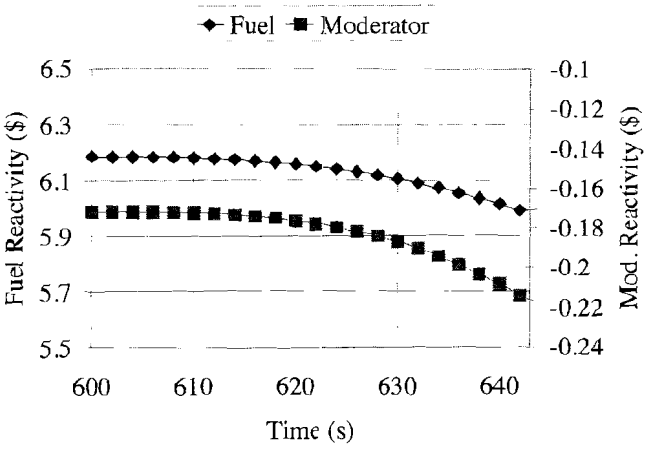

Fig. 7. Variation of the fuel and moderator reactivities during transient using the Simulink model.

V. CONCLUSION

The Simulink model of the GT-MHR core presented in this paper (Fig. 8) can be used to perform different types of transient scenarios. The modular structure of the program and the fully interactive environment make the program easy to run, debug, modify, and expand to develop detailed models.

As an example of the Simulink model applications, results of the full-power reactivity insertion transient simulation were presented. Furthermore, we showed that the results of the Simulink model simulation were in a very close agreement with the results of a RELAP5 model simulation.

By including a model of the balance of the plant, applications of the program may be extended to simulate long-term transients as well. Applicability of the program for long-term simulations requires further investigations.

APPENDIX A

CORE NEUTRONICS MODEL

The neutronics model of the GT-MHR core calculates the neutron population as a function of the reactor reactivity and the core neutronics parameters. The power is computed using the space-independent (or point-kinetics) approximation, which assumes that the core power distribution can be written as a product of functions of space and time. Comparisons performed between space-dependent and point model calculations show that for the maximum reactivity transients possible for HTRs, there is very little discrepancy in the behavior of the total reactor power with time[8] between space-dependent and space-independent calculations. This means that if the flux shape is not changed during the transient, the results of the point model are sufficiently accurate, as far as neutron kinetics is concerned. However, assumptions of space-time independence are not valid for the heat transfer calculations because the shape of the axial temperature profile may change strongly during a power excursion.

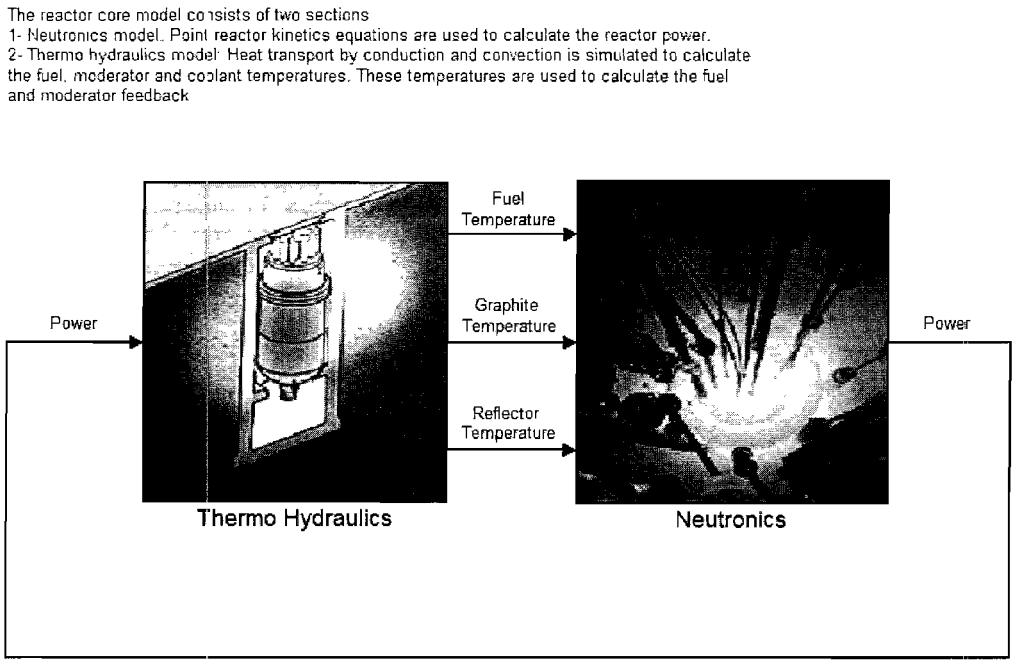

Fig. 8. Simulink diagram of the core block.

The total power of the reactor is the sum of the immediate fission power, the fission product, and the actinide decay powers. The immediate fission power is the power that is released at the time of fission and includes the power from the kinetic energy of the fission products and the power that is deposited in the core as a consequence of neutron moderation. Decay power is generated as the fission products and actinides undergo reactivity decay. In this Simulink model, we assume that in fast transients, changes in the reactor power are dominated by changes in the fission power. Therefore, the fission product and actinide decay powers are assumed to remain constant during FPRIT and SURIT simulations.

The following equations are used to calculate the reactor fission power (see footnote a on p. 317):

$$\frac{d}{dt}\varphi(t) = \frac{(\rho(t)-\beta)\varphi(t)}{\Lambda} + \sum_{i=1}^{N_d}\lambda_i C_i(t) + S \ , \quad \text{(A.1)}$$

$$\frac{d}{dt}C_i(t) = \frac{\beta f_i}{\Lambda}\varphi(t) - \lambda_i C_i(t) \ , \quad \text{(A.2)}$$

$$\psi(t) = \Sigma_f \varphi(t) \ , \quad \text{(A.3)}$$

and

$$P_f(t) = Q_f \psi(t) \ , \quad \text{(A.4)}$$

where

$\varphi(t)$ = neutron flux

$C_i(t)$ = neutron precursor flux of group i

β = effective delayed neutron fraction

Λ = prompt neutron generation time

ρ = reactivity

f_i = fraction of delayed neutrons of group i

λ_i = decay constant of group i

S = source

$\psi(t)$ = fission rate (s^{-1})

Σ_f = macroscopic fission cross section

$P_f(t)$ = immediate fission power (MeV/s)

Q_f = immediate fission energy per fission (MeV);

$$P_{total}(t) = Q_f X \psi(t) + P_{decay} \ , \quad \text{(A.5)}$$

where X is the conversion factor from MeV/s to watts.

All the abovementioned parameters are specified as the inputs of the model and can be changed during the simulation through the neutronics block.

To implement the point-kinetics equations into the Simulink program, the neutronics block has been developed. The neutronics block includes two major subsystems: (a) the delayed neutron subsystem and (b) the

reactivity feedback subsystem. The delayed neutron subsystem calculates the immediate fission power, based on Eqs. (A.1) through (A.5). The reactivity feedback subsystem computes the reactivity feedback associated with the fuel, moderator, and reflector temperatures. The rod banks' worth is computed in a separate subsystem and is used along with the reactivity that is computed in the reactivity feedback subsystem to calculate the total reactivity of the core.

Temperature reactivity feedback effects on the reactor are modeled through the inclusion of fuel temperature feedback, moderator temperature feedback, and reflector temperature feedback. The temperature through the core is calculated with the thermohydraulics block, which is presented in Appendix B. The reactivity feedback for the fuel, moderator, and reflector, as a function of temperature, is specified by the user in the reactivity feedback subsystem. The relation between the reactivity and temperature of the materials can be specified as an algebraic function or as a curve. Thus, the program uses accurate models of reactivity feedback over a wide temperature range for each of the aforementioned core materials. Using accurate temperature feedback models is necessary when the variations of temperature and, consequently, the feedback reactivity are significant. A user may disable any of the feedback mechanisms during simulation using disabling options that are provided in the reactivity feedback subsystem.

A.I. SIMULINK NEUTRONICS MODEL STRUCTURE

The neutronics block (Fig. A.1) receives fuel, moderator, and reflector temperatures as input and calculates the reactor power. By double-clicking on this block, the Simulink diagram of the neutronics block will appear. The user specifies the initial power, delayed neutron fraction, prompt neutron generation time, and delayed neutrons' specifications in this model. Two subsystems are placed in this model: the delayed neutron subsystem and the temperature feedback subsystem.

The delayed neutron block calculates the concentration of delayed neutron precursors. By double-clicking on this block, Fig. A.2 pops up, in which the user specifies the fraction of delayed neutrons and decay constant for each of six delayed neutron groups. To see more details of the delayed neutron block, the user can choose the "Look under mask" option after right-clicking on the block. If the user does this, then a schematic will appear in which each delayed neutron precursor group is modeled by a group block.

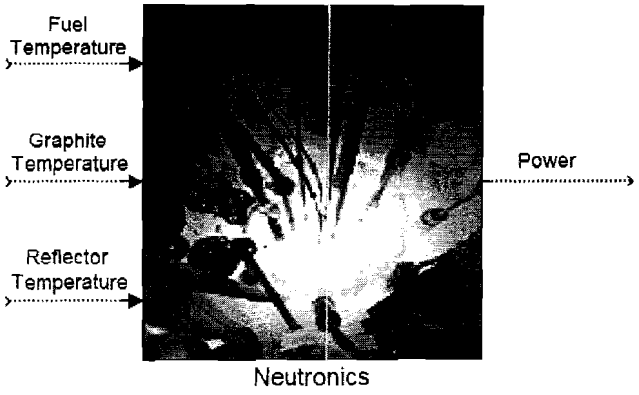

Fig. A.1. Neutronics block schematic diagram.

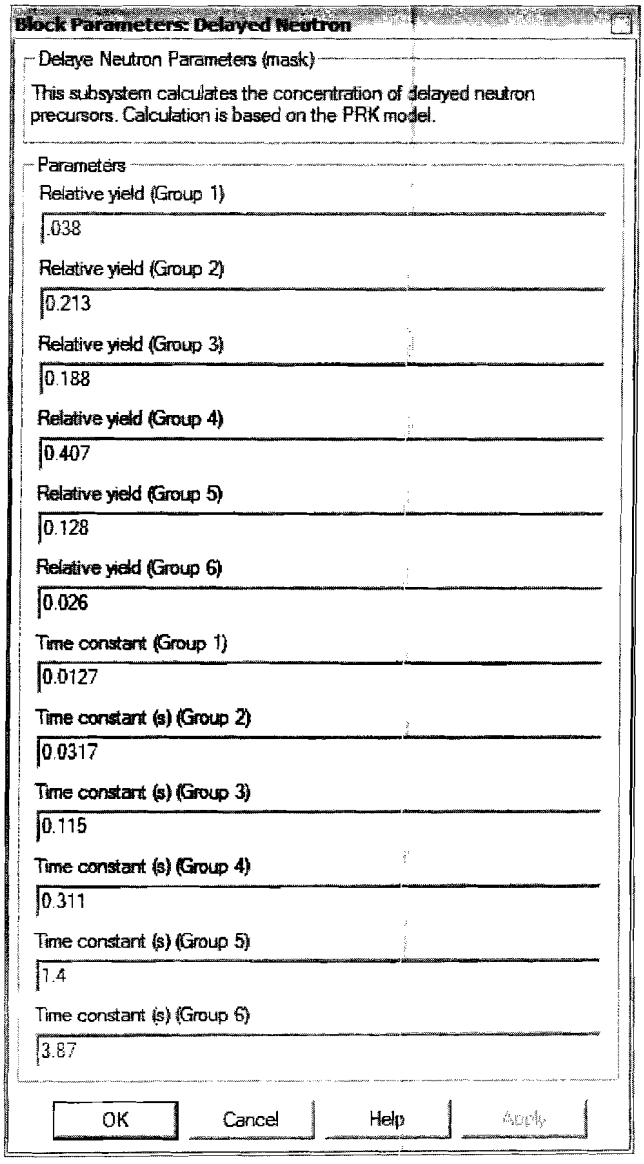

Fig. A.2. Delayed neutron block dialog window.

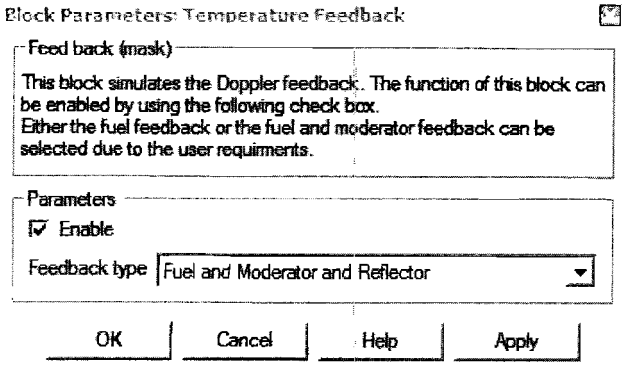

Fig. A.3. Feedback block dialog window.

By double-clicking on each of the group blocks, the user can see a detailed model of the block. Each of the group blocks models a delayed neutron precursor concentration equation.

The temperature reactivity block simulates the temperature reactivity feedback. This block accepts the fuel, moderator, and reflector temperatures and calculates the reactivity associated with the temperature of each of these elements.

By double-clicking on the temperature feedback block, the dialog box shown in Fig. A.3 will pop up, which allows the user to disable or enable the function of this block. In this way, a user can easily compare the simulation response with and without feedback. Also, the effects of temperature feedback due to the various elements (fuel, moderator, and reflector) can be identified by specifying in this dialog block dialog window either fuel feedback, fuel and moderator feedback, or fuel and moderator and reflector feedback.

APPENDIX B

CORE THERMOHYDRAULICS MODEL

To study the reactor core dynamics, space-dependent heat transfer calculations are essential, although zero-dimensional neutron kinetics equations are, in many cases, sufficient. The core thermohydraulics model simulates the heat transfer from the fuel to the moderator and from the moderator to the coolant. The temperatures of the fuel, moderator, and reflector are calculated as a function of time at a flexible number of radial and axial locations. The number of locations that one employs in the calculations, of course, depends on the required accuracy.

In this Appendix, the thermohydraulics model of the GT-MHR core is presented. In Sec. B.I, the mathematical model of the reactor core heat transfer is explained. Thereafter, in Sec. B.II, implementation of the heat transfer mathematical model with the Simulink program is discussed.

B.I. GENERAL ATOMICS RELAP5 COOLANT-HOLE CENTERED MODEL

The thermohydraulics model of our Simulink program is based on the coolant-hole centered concept, which has been developed by General Atomics. According to the RELAP5 model of the GT-MHR developed by General Atomics, heat transfer by conduction and convection are simulated using a coolant-hole centered model. There are in total 10 361 coolant holes within the core. All the coolant holes are modeled using a single equivalent representative coolant hole, which is shown in Fig. B.1. The coolant-hole structure is divided into axial and radial nodes in such a way that the axial conduction within the flowing fluid and the solid elements of the core can be neglected. As specified in Fig. B.1, to calculate the temperature distribution using the coolant-hole model, the geometry of the model is divided into five axial regions, and each axial region is divided into six radial nodes. Thus, in total, to match the General Atomics GT-MHR model, the coolant-hole structure in our Simulink thermohydraulics model is, by default, divided into 30 nodes, and the temperature is calculated at mesh points of each temperature node. However, the number of axial and radial nodes is flexible and can be specified by the user, depending on the required accuracy and the computation time.

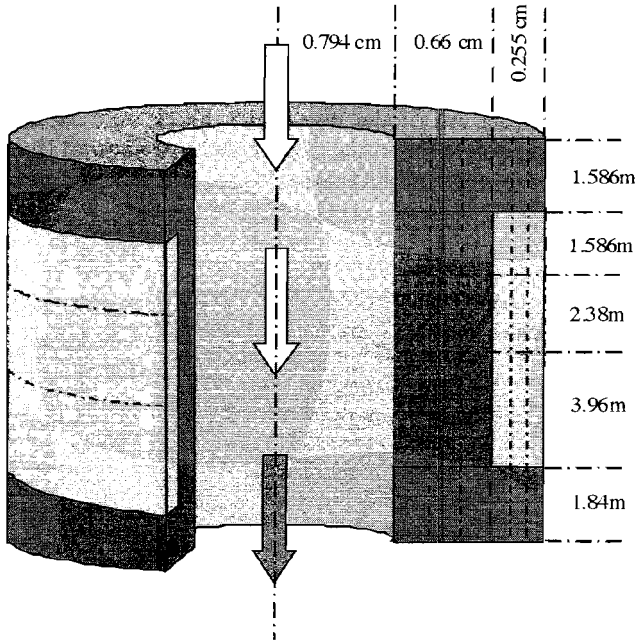

Fig. B.1. Three-dimensional representation of a coolant-hole centered model.

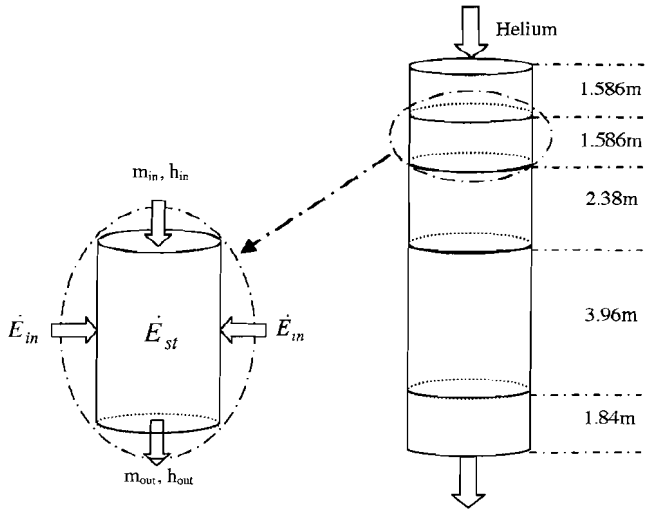

Fig. B.2. Coolant channel divisions.

The heat is generated in the fuel compacts, which are radially located at the outer surface of the coolant-center model cylinder and axially placed between the top and bottom reflectors as shown in Fig. B.1. The total fuel height is 7.93 m, and it is placed in a ring with an inner radius of 1.454 cm and outer radius of 1.709 cm. The fuel is divided into three axial layers (with the ratio from top to bottom of 2:3:5), and each layer has three radial nodes with equal width. Therefore, the fuel is in total divided into nine nodes.

In the coolant-hole centered model, the coolant, which is He, flows in the channel in the middle of the coolant hole, which is surrounded by the moderator. As shown in Fig. B.2, the coolant channel is divided into five axial nodes.

B.I.A. Heat Transfer in Fuel and Graphite

The heat transfer in the fuel and moderator is studied by considering each node as a control mass system. Heat is transferred by conduction from the fuel to the moderator and then by convection to the coolant. To study the heat transfer in each conduction node, the energy balance equation is applied to the control mass system that represents the conduction node:

$$\dot{E}_{in} + \dot{E}_g - \dot{E}_{out} = \dot{E}_{st} \ , \tag{B.1}$$

where

$\dot{E}_{in}, \dot{E}_{out}$ = rates of internal energy transfer in and out across the surface of the system due to heat transfer, respectively

$\dot{E}_g$ = rate of internal energy generation within the system

$\dot{E}_{st}$ = rate of internal energy storage within the system.

The energy stored in a control mass system $\dot{E}_{st}$ is calculated by

$$\dot{E}_{st} = \rho V c \frac{dT}{dt} \ , \tag{B.2}$$

where

ρ = material density

V = node volume, which is constant in this case

c = material heat capacity

T = average temperature of the node.

The rate of energy transfer to each node $\dot{E}_{in}$ is specified by the energy transported into it from the adjacent nodes. On the other hand, the rate of energy transfer out of the node $\dot{E}_{out}$ is calculated based on the difference between the radial coordinates of the inner and outer surfaces of the node. In general, the rate of energy transfer from any surface is calculated by

$$\dot{Q} = -kA \frac{dT}{dr} \ , \tag{B.3}$$

where

k = material thermal conductivity

A = area of conduction

r = radial coordinate.

As explained previously, in the coolant-hole model, with regard to radius, energy is transported radially inward. For this reason, Eq. (B.3) is written in such a way that $\dot{E}_{out}$ is positive when the temperature at the outer surface is higher than that of the inner surface.

The rate of internal energy generation within the system $\dot{E}_g$ is calculated based on the total power of the core (which in the Simulink implementation of the model is calculated in the neutronics block) and the volume of the node.

By substituting Eqs. (B.2) and (B.3) into Eq. (B.1), we derived a differential equation. For each node, $\dot{E}_{in}$ and $\dot{E}_g$ are defined as inputs, and temperatures at the node boundaries are computed. This differential equation has been discretized in Simulink using forward difference, backward difference, and central difference discretization schemes.

B.I.B. Heat Transfer in the Coolant

To model the heat transfer from graphite to the coolant, the coolant channel is divided into a number of control volume systems. The energy rate balance equation is employed for each control volume to calculate the

helium temperature in the control volume. The energy rate balance equation for a control volume system is represented as[9]

$$\frac{dE_{cv}}{dt} = \dot{Q}_{cv} - \dot{W}_{cv} + \sum \dot{m}_i \left(h_i + \frac{V_i^2}{2} + g z_i \right) - \sum \dot{m}_e \left(h_e + \frac{V_e^2}{2} + g z_e \right) , \quad \text{(B.4)}$$

where

E_{cv} = energy of the control volume system

$\dot{Q}_{cv}$ = net rate of energy transfer in the system by heat transfer

$\dot{W}_{cv}$ = net work done by the control volume system

$\dot{m}_i, \dot{m}_e$ = mass flow rates at the inlet and exit, respectively

h_i, h_e = fluid enthalpy at the inlet and exit, respectively

z_i, z_e = elevation at the inlet and exit, respectively

V_i, V_e = fluid velocity at the inlet and exit, respectively

g = acceleration due to gravity.

The mass flow rate into the control volume is assumed to be equal to the mass flow rate out of the control volume, which means $\dot{m}_i = \dot{m}_e$. Furthermore, the number of calculations and consequently the computation time can be reduced by assuming that the difference in the velocity (V_i, V_e) and elevation (z_i, z_e) at the input and exit of the control volume system is negligible. These approximations have been made in the Simulink model.

B.I.C. Core Material

The coolant-hole model consists of three materials: fuel, graphite, and helium. Grade H-451 graphite is used as the moderator and reflector materials. The top and bottom portions of the coolant hole are top and bottom reflectors, respectively. To calculate the temperature of the coolant-hole structure, the thermal conductivity k, the heat capacity c_p, and the product of the mass density ρ and heat capacity c_p for all the aforementioned materials have to be specified, as a function of the material temperature.

B.II. SIMULINK IMPLEMENTATION OF RELAP5 THERMOHYDRAULICS MODEL

The thermohydraulics model of the core is modeled by the thermohydraulics block presented in Fig. B.3. This

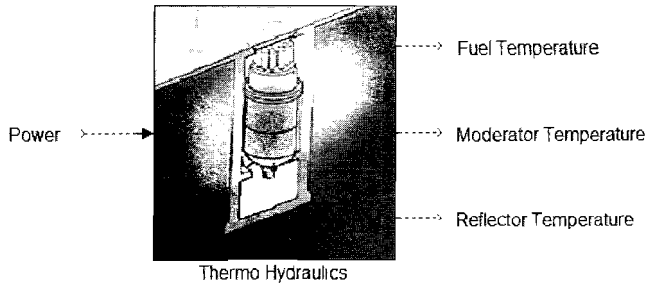

Fig. B.3. Thermohydraulics block diagram.

block takes as input the reactor power calculated in the neutronics block and, based on the reactor power, computes the temperature distribution throughout the coolant-hole structure, as well as the average temperatures of the fuel, moderator, and reflector.

The thermohydraulics block contains the coolant-hole geometrical specifications, and blocks to specify the fuel, moderator, and coolant physical properties. As discussed earlier, the reactor core is divided into five axial locations. In the thermohydraulics block, the fraction of power that is generated in each axial location is specified. The total reactor power is divided by the total number of coolant holes, which is 10 361. As presently specified (with a configuration that matches that of the RELAP5 model of the GT-MHR), the coolant-hole structure is divided into five axial layers, each modeled by a row block. Each row block has two inputs: (a) the total power generated in that axial layer and (b) the coolant inlet temperature. The inlet temperature of the first row block is simply the inlet temperature of the coolant channel. The inlet temperature of the other row blocks is the outlet temperature of the previous row block. The number of row blocks can be easily customized to obtain the required accuracy.

The average temperatures of the fuel, moderator, reflector, and coolant are calculated in the coolant-hole subsystem based on the temperatures calculated in each row block. Row blocks calculate the temperature along each axial layer at a selectable number of thermal nodes. Therefore, each row block contains a number of node blocks. There are two types of nodes in each row: (a) conduction nodes represented by "Node" and (b) the convection node indicated by "HeNode." These two types of thermal nodes are described in Secs. B.II.A and B.II.B.

B.II.A. Conduction Node

A conduction node models one-dimensional heat transfer by conduction in a Cartesian, cylindrical, or spherical coordinate system. Based on the selected coordinate system, the parameters that are required to specify the geometry of the node appear. For instance, if a cylindrical coordinate system is chosen, the node is a

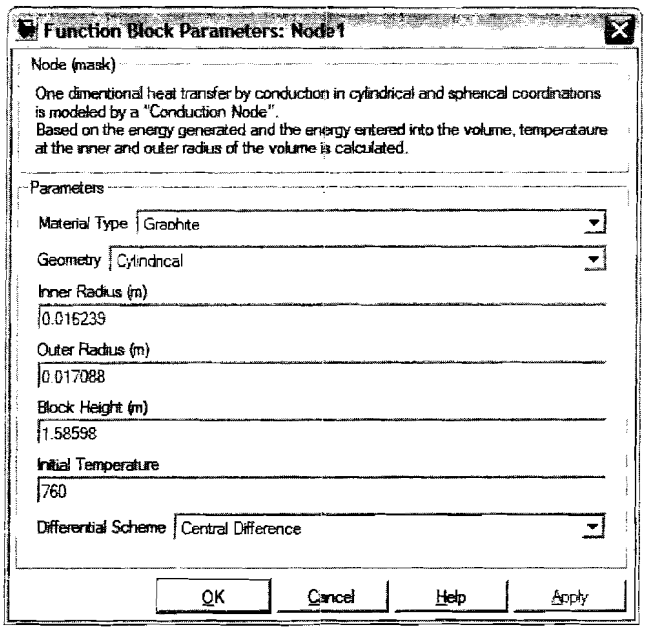

Fig. B.4. Conduction node block dialog window.

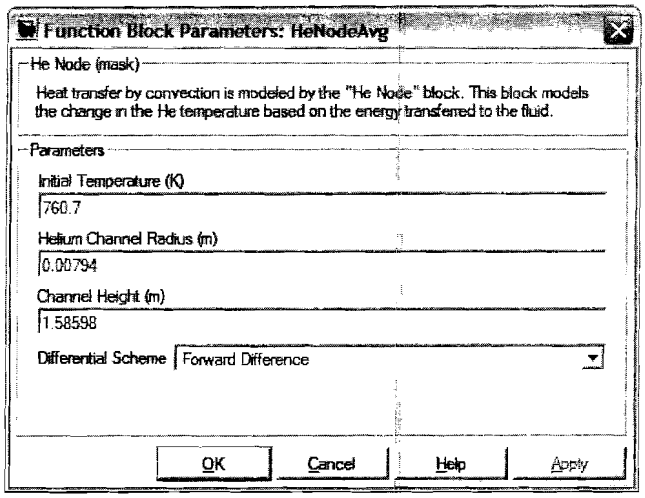

Fig. B.5. Convection node block dialog window.

ring, which is specified by its outer radius, inner radius, and height. Each conduction node consists of a single material that is specified in the dialog window. A sample dialog window, which appears by double-clicking on the conduction node, is shown in Fig. B.4.

The conduction node block has three inputs: (a) rate of energy generated in the node $\dot{E}_g$, (b) rate of energy transfer into the node $\dot{E}_{in}$, and (c) temperature of the adjacent node. The node temperature and the rate of energy transfer out of the node are calculated using the energy balance equation as explained in Sec. B.I.A.

As presented earlier, the heat transfer equation used in our analysis is a parabolic differential equation. A number of discretization schemes exist to solve this type of equation numerically.[17] Among those, this Simulink model lets the user select between the central, backward, and forward difference schemes. Although generally the central difference scheme has the best accuracy, in some situations the initial condition forces one to use another type of discretization scheme. Therefore, the flexibility of applying different numerical schemes is important in some situations.

B.II.B. Convection Node

In each row block, the heat transfer by convection is modeled by convection nodes. The convection node block has two inputs: (a) rate of energy transfer into the coolant (which in this case comes from the moderator) and (b) the coolant inlet temperature. The coolant outlet temperature T_h and the surface temperature T_s are evaluated in this block using Eq. (B.4).

By double-clicking on the convection block, a dialog window appears that allows the user to specify the control volume geometry, namely, the coolant channel radius, the channel height, and also the initial temperature of the coolant (Fig. B.5).

As a part of the convection node block, a subsystem was developed to evaluate the coolant thermal properties, which is "He calculator" block. This subsystem calculates the coolant density, specific heat, thermal conductivity, and convection heat transfer coefficient as a function of the coolant temperature. Other single-phased coolants may be considered by modifying the physical properties of the coolant in this block.

APPENDIX C

MODEL OF THE CONTROL INSTRUMENTATION

In this Appendix, the Simulink models of the controlling instruments are described. Models of control instruments help the user simulate and analyze various types of scenarios in order to study and evaluate the reactor dynamic response. The Simulink program's control instruments models are separated into two major categories: (a) model of the control room and (b) model of the reactivity control assemblies.

C.I. CONTROL ROOM MODEL

The reactor control is based on the physical quantities, which are measured with various accuracy, delay, and reliability. The quantities of interest usually are neutron flux; temperature of fuel, coolant, and structures;

coolant mass flow; coolant pressure; and coolant activity.[8] The control room model simulates a number of instruments that are available in most reactors' control rooms, such as dials and gauges to monitor the control rods' positions; the average coolant temperature, $T_{av} = (T_h + T_c)/2$; the coolant inlet and outlet temperatures; and the coolant mass flow rate. In addition, other instruments and readings that are not available in a real control room, but that are important for understanding the dynamics of the plant, as modeled by Simulink, such as the temperature distribution throughout the core, average fuel temperature, average moderator temperature, average reflector temperature, reactor multiplication factor, reactor reactivity, fuel reactivity, moderator reactivity, and reflector reactivity, are included for completeness.

Figure C.1 presents the Simulink diagram of the control room model. On the right side of Fig. C.1, gray-color blocks, are used to display the reactor's parameters. In addition, the reactor power is displayed by an LCD display and sketched in the strip chart.

To monitor the temperature distribution in the core, the user can double-click on the temperature distribution block on the control room form. The temperature distribution for the coolant-hole model that was discussed earlier is displayed at the 35 mesh points discussed earlier with a 5×7 matrix. In addition, the He temperature at five axial locations along the He channel is displayed.

In Secs. C.I.A, C.I.B, and C.I.C, subsystems that were developed to control the reactor model characteristics are explained.

C.I.A. Neutron Source

A neutron source block was designed to model the external neutron source. The relation between the photofission source strength and the initial fission power is determined by the reactor subcritical multiplication. We have used the following point reactor kinetic (PRK) equations to calculate the equilibrium fission power. The PRK equations were presented in Eqs. (A.1) and (A.2).

When the reactor reaches equilibrium, the fission power and the delayed neutron precursor concentrations are constant in time. Therefore, $d\tilde{C}_i(t)/dt = 0$ and

$$\frac{\beta_i}{\Lambda} P(t) = \lambda_i \tilde{C}_i(t) \ . \qquad \text{(C.1)}$$

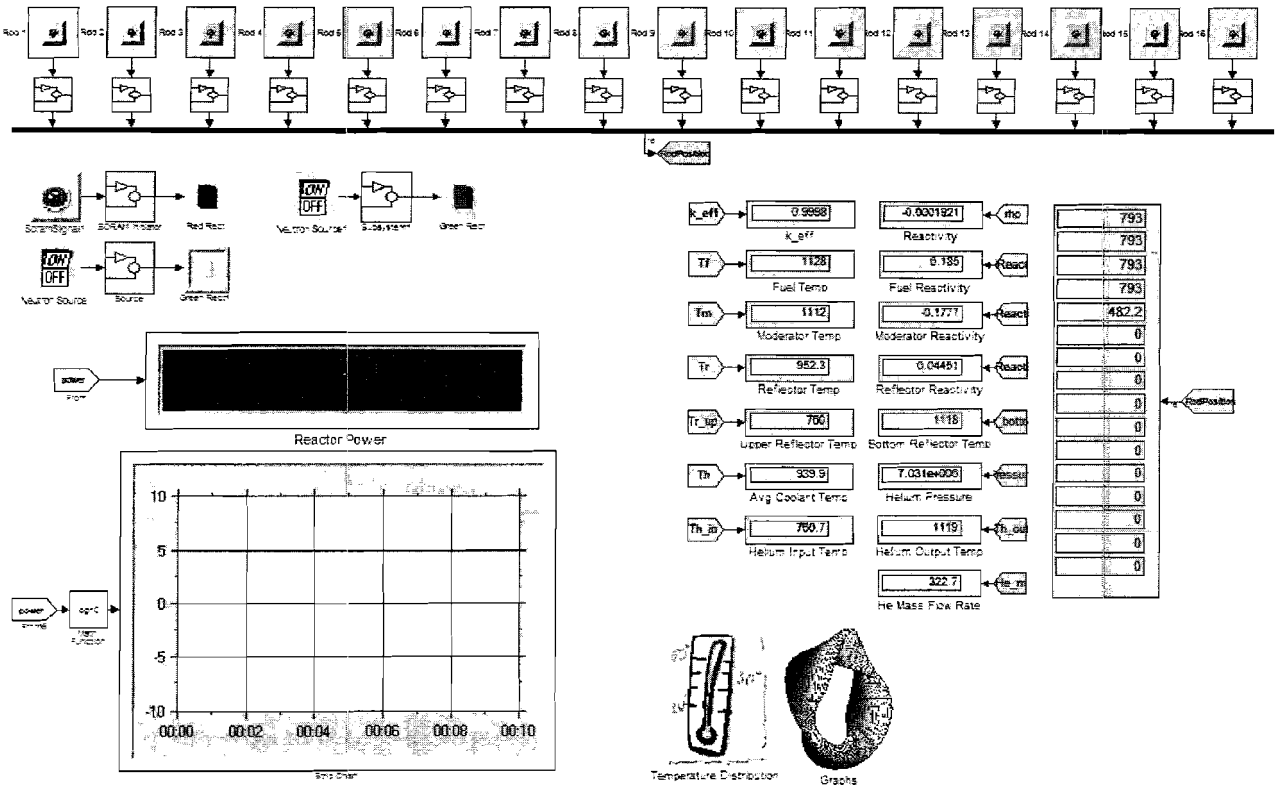

Fig. C.1. Simulink diagram of the control room model.

Substituting Eq. (C.1) into Eq. (A.2), we derive

$$\frac{\rho(t)-\beta}{\Lambda}P+\sum_{i=1}^{N_d}\frac{\beta_i}{\Lambda}P+S=0$$

$$\Rightarrow \frac{\rho(t)-\beta}{\Lambda}P+\frac{\beta}{\Lambda}P+S=0$$

$$\Rightarrow \frac{\rho(t)}{\Lambda}P+S=0\ ,$$

and finally

$$\Rightarrow S=-\frac{\rho(t)}{\Lambda}P\ . \qquad \text{(C.2)}$$

Using Eq. (C.2), we can numerically calculate the neutron source strength that is required to produce a specific fission power P in equilibrium.

C.I.B. Automatic Control Rod Adjustment

This block automatically adjusts the control rods' positions to make the reactor critical. When this switch is off, the user has to adjust the reactivity by changing the control rod position.

C.I.C. SCRAM Initiator

This block initiates a SCRAM when the power increases beyond the safety margins. The other scram functions such as scram on the rate of power increase are not included, since our goal is to reproduce the RELAP5 model of the GT-MHR and other scram functions are not utilized in the RELAP5 model. Upon initiating a SCRAM, all rod banks are inserted into the core with the speed that is specified on the controller block.

The SCRAM can be initiated manually by pressing the "ScramSignal" button or automatically by specifying a maximum power on the SCRAM initiator block. By double-clicking on the SCRAM initiator block, a dialog window appears in which the reactor full thermal power and the maximum power ratio for the initiation of a scram are specified.

C.II. REACTIVITY CONTROL ASSEMBLIES

The reactivity control assemblies' model simulates the rod banks and their movement. Two subsystems are designed to model the rod banks: (a) controller blocks that model the rod banks' movement and (b) reactivity control assemblies that models the rod banks' reactivity worth.

The controller block is located on the control room model. Each rod bank is controlled by a controller block. This block is connected to a button that activates the controller block when the button is set to "on." The rod bank's position does not change when the button is off.

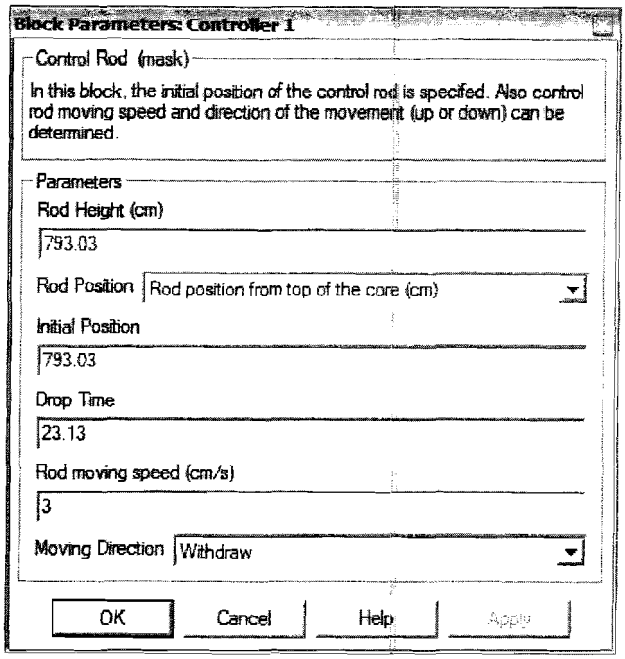

Fig. C.2. Controller block dialog window.

By double-clicking on the controller block, a dialog window shown in Fig. C.2 pops up, which allows the user to specify the following parameters:

1. *rod height*: the total rod height in centimeters
2. *initial position*: indicates the initial rod position measured from top of the core
3. *drop time*: time required for a fully withdrawn rod to insert completely on initiation of the SCRAM scenario
4. *rod speed*: specifies the speed of the rod when it is inserted or withdrawn
5. *rod direction*: indicates if the rod is withdrawn or inserted.

While the controller block simulates the movement of the rod banks, the reactivity control assemblies block has been developed to model the reactivity of the control rods. This block is located on the model main page, although the rod banks' positions are specified by the models located on the control room model. Using the position of the rod bank, the rod bank's reactivity is calculated on the reactivity calculator block. Besides a rod bank's position, a rod bank's reactivity worth depends on the history of reactor operation. Rod bank reactivities are reported by General Atomics for the beginning of equilibrium cycle (BOEC), MOEC, and end of equilibrium cycle. In our analysis, the BOEC and

MOEC data are used for the start-up and full-power analyses, correspondingly.

By double-clicking on the reactivity calculator block, a dialog window pops up, and the total reactivity of each rod bank can be specified in this dialog. Although the total reactivity of rod banks varies among rod banks, we assumed that the fraction of bank worth as a function of insertion fraction is the same for all rod banks. However, the function describing the fraction of a bank's worth as a function of insertion can be defined for each of the rod banks differently. This function is specified by either an algebraic expression or a curve. Finally, knowing the insertion fraction for each rod, the reactivity associated with each rod bank is calculated by multiplying the bank fraction and the total bank worth.

ACKNOWLEDGMENT

This material is based upon work supported by the U.S. Department of Energy (DOE) under the NERI program Award No. DE-FG-07-02SF22620 and NERI Project No. 02-207. Any opinions, findings, and conclusions or recommendations expressed in this material are those of the authors and do not necessarily reflect the views of the DOE.

REFERENCES

1. F. H. RUDDY, A. R. DULLOO, J. G. SEIDEL, F. W. HANTZ, and L. R. GROBMYER, "Nuclear Reactor Power Monitoring Using Silicon Carbide Semiconductor Radiation Detectors," *Nucl. Technol.*, **140**, 198 (2002).

2. A. R. DULLOO, F. H. RUDDY, J. G. SEIDEL, J. M. ADAMS, J. S. NICO, and D. M. GILLIAM, "The Neutron Response of Miniature Silicon Carbide Semiconductor Detector," *Nucl. Instrum. Methods Phys. Res. A*, **422** 47 (1999).

3. A. R. DULLOO, F. H. RUDDY, J. G. SEIDEL, S. SESHADRI, and L. B. ROWLAND, "Development of a Silicon Carbide Radiation Detector," *IEEE Trans. Nucl. Sci.*, **45**, *3* (June 1998).

4. M. REISI FARD, T. E. BLUE, and D. W. MILLER, "SiC Semiconductor Detector Power Monitors for Space Nuclear Reactors," *Proc. Space Technology and Applications International Forum (STAIF-2004)*, M. S. EL-DENK, ED., Albuquerque, New Mexico, February 8–12, 2004, American Institute of Physics (2004).

5. M. REISI FARD, T. E. BLUE, D.W. MILLER, F. H. RUDDY, A. R. DULLOO, and J. G. SEIDEL, "A Mathematical Model of SiC Detector as Power Monitors," *Proc. 4th Int. Topl. Mtg. Nuclear Plant Instrumentation, Control and Human Machine Interface Technology*, Columbus, Ohio, September 19–22, 2004, American Nuclear Society (2004) (CD-ROM).

6. M. REISI FARD, T. E. BLUE, and D. W. MILLER, "Effect of Detector Capacitance and Cable on SiC Detector-Cable System Performance," *Proc. 4th Int. Topl. Mtg. Nuclear Plant Instrumentation, Control and Human Machine Interface Technology*, Columbus, Ohio, September 19–22, 2004, American Nuclear Society (2004) (CD-ROM).

7. T. QUINN, "Instrument and Control for Advanced Reactors Safety Margin," presented at American Nuclear Society Advanced Gas Reactor Technology Course, San Diego, California, June 9–10, 2005.

8. L. MASSIMO, *Physics of High Temperature Reactors*, Pergamon Press, New York (1976).

9. C. RODRIGUEZ, J. ZGLICZYNSKI, and D. PFREMMER, "GT-MHR Operations and Control," *Proc. Development Status of Modular High Temperature Reactors and Their Future Role*, Petten, Netherlands, November 28–December 1, 1994, ECN (1994).

10. M. REISI FARD, T. E. BLUE, and D. W. MILLER, "GT-MHR Start-Up Reactivity Insertion Transient Using Simulink," *Proc. Int. Congress Advances in Nuclear Power Plants (ICAPP '06)*, Reno, Nevada, June 4–8, 2006, American Nuclear Society (2006) (CD-ROM).

11. "Code on the Safety of Nuclear Research Reactors Design, Safety Standards," SS-35-S1, International Atomic Energy Agency (1992).

12. "Research Reactor Core Conversions—Guidebook," TEC-DOC 233, International Atomic Energy Agency (1992).

13. V. TANGIRALA, "RELAP5/MOD3 Model Enhancements Calculation Report," Document No. 910756, Rev. 0, General Atomics (Dec. 1994).

14. S. A. WRIGHT and T. SANCHEZ, "Dynamic Modeling and Control of Nuclear Reactors Coupled to Closed-Loop Brayton Cycle Systems Using SIMULINK," *AIP Conf. Proc.*, **746**, *1*, 991 (2005).

15. S. A. WRIGHT, "Preliminary Results of Dynamic System Model for a Closed-Loop Brayton Cycle Coupled to a Nuclear Reactor," *Proc. 1st Int. Energy Conversion Engineering Conf.*, Portsmouth, Virginia, August 17–21, 2003.

16. M. EL-GENK and J. TOURNIER, "DynMo: Dynamic Simulation Model for Space Reactor Power Systems," *AIP Conf. Proc.*, **746**, 1005 (2005).

17. G. D. SMITH, *Numerical Solution of Partial Differential Equations: Finite Difference Methods*, 3rd ed., Oxford University Press, New York (1986).